

PROBING QUANTUM CRITICALITY IN AN IRON-BASED  
SUPERCONDUCTOR WITH SYMMETRY-BREAKING STRAIN

A DISSERTATION  
SUBMITTED TO THE DEPARTMENT OF APPLIED PHYSICS  
AND THE COMMITTEE ON GRADUATE STUDIES  
OF STANFORD UNIVERSITY  
IN PARTIAL FULFILLMENT OF THE REQUIREMENTS  
FOR THE DEGREE OF  
DOCTOR OF PHILOSOPHY

Thanapat Worasaran

August 2021

© 2021 by Thanapat Worasaran. All Rights Reserved.  
Re-distributed by Stanford University under license with the author.



This work is licensed under a Creative Commons Attribution-Noncommercial 3.0 United States License.

<http://creativecommons.org/licenses/by-nc/3.0/us/>

This dissertation is online at: <https://purl.stanford.edu/kk851jj6905>

I certify that I have read this dissertation and that, in my opinion, it is fully adequate in scope and quality as a dissertation for the degree of Doctor of Philosophy.

**Ian Fisher, Primary Adviser**

I certify that I have read this dissertation and that, in my opinion, it is fully adequate in scope and quality as a dissertation for the degree of Doctor of Philosophy.

**Harold Hwang**

I certify that I have read this dissertation and that, in my opinion, it is fully adequate in scope and quality as a dissertation for the degree of Doctor of Philosophy.

**Steven Kivelson**

Approved for the Stanford University Committee on Graduate Studies.

**Stacey F. Bent, Vice Provost for Graduate Education**

*This signature page was generated electronically upon submission of this dissertation in electronic format. An original signed hard copy of the signature page is on file in University Archives.*

I dedicate this thesis to my father.

# Abstract

Electronic nematicity is often invoked as being an important ingredient for unconventional superconductivity in iron-based superconductors. Theoretically, quantum critical nematic fluctuations, if present, can enhance the superconductivity or even be responsible for the superconducting pairing mechanism itself. The phenomenology of the nematic quantum criticality, however, is not well established as the evidence for the quantum criticality with nematic character is limited. In this work, I develop experimental techniques using strain as a primary tool to probe this quantum critical phenomena.

My dissertation presents a linear storyline with three experiments. In the first experiment, I study the effect of the symmetry-preserving  $A_{1g}$  strain and the orthogonal antisymmetric strain  $B_{1g}$  to the critical temperature  $T_S$  of the nematic phase transition in a prototypical iron-based superconductor,  $\text{Ba}(\text{Fe}_{0.975}\text{Co}_{0.025})_2\text{As}_2$ . The decomposition is achieved by comparing the material's response under two different environments: hydrostatic pressure and uniaxial stress applied along [100] crystallographic direction. The result establishes the orthogonal antisymmetric strain  $B_{1g}$  as an effective tuning parameter for the nematic order, due a large quadratic dependence of  $T_S$  on  $B_{1g}$  strain. In the second experiment, I utilize this perspective by using the uniaxial stress to systematically study the effect of  $A_{1g}$  and  $B_{1g}$  strains on  $T_S$  in various compositions of  $\text{Ba}(\text{Fe}_{1-x}\text{Co}_x)_2\text{As}_2$ , especially those close to the optimally doped composition. A power-law behavior of the critical temperature  $T_S$  was observed as a function of the combined tuning parameters, which is a linear combination of  $A_{1g}$  strain,  $B_{1g}$  strain, and cobalt concentration  $x$ . This provides the first clear evidence for power-law behavior of the critical temperature as a function of non-thermal tuning parameters. A consequence of this observation is that the uniaxial stress (along [100] crystallographic direction) is increasingly effective as a tuning parameter when approaching the quantum critical point. This inspired the third experiment, where I present a new technique to measure nematic susceptibility using a novel conjugate field constructed from a combination of a time-varying strain and a magnetic field. The technique allows for the measurement of the nematic susceptibility while continuously tuning with ( $A_{1g}$  and  $B_{1g}$ ) strain. While the signal associated with this coupling is observed, it does not follow the anticipated temperature dependence, implying that the signal may have come from other microscopic origins, and that the coefficient coupling this conjugate field to the

nematic order parameter is too small to be measured in this material. I do, however, hope that this third experiment establishes a roadmap that will be useful for future investigations of alternative materials.

# Acknowledgments

Work presented in this thesis was supported by the Department of Energy, Office of Basic Energy Sciences, under contract DE-AC02-76SF00515.

Graduate school has been very challenging in many ways, but there are also many happy moments along this journey. Looking back, it is hard to believe how much I have grown intellectually and as a person. This journey would not have been completed without so many people who supported me along the way, and I could not be grateful enough for them.

I first and foremost like to express my deep gratitude to my advisor, Prof. Ian Fisher. When I said I could not have asked for a better advisor, I meant it. Ian is a tremendous scientist, teacher, mentor and a wonderful person all around. It is no secret that I struggled and have issues with up and down in motivation, and Ian is always there, listening and patiently guiding me all the way. I hope that we stay in touch after my graduation as friends, and I would love to be invited to cook some Beef Wellington for your family again (yes, there is a story behind it).

I would like to thank my thesis committee and my reading committee - Prof. Steven Kivelson, Prof. Harold Hwang, Prof. Aharon Kapitulnik, and Prof. Ben Feldman, especially for scheduling the defense and reading the thesis on such a tight schedule.

I would like to thank Prof. Steven Kivelson, Prof. Sri Raghu, Prof. Joerg Schmalian, and Prof. Rafael Fernandes for educating me with their vast theoretical knowledge.

I would like to thank all the GLAM and applied physics administrators and staff for operating the department and keeping everything running smoothly: Paula Perron, Claire Nicholas, Fiona Chiu, Patrice O'Dwyer, Margo Holly, Corrina Peng, Clara Yeung, Chris McIntosh, Lina Alsibai, Cynthia Sanchez Sybille Katz, and Mark Gibson.

People in the FisherLab are one of the nicest people and one of the smartest people I have ever met. The first member of the FisherLab I have met is my master degrees advisor in Cambridge and Ian's first graduate student, Prof. Suchitra Sebastian. Suchitra is an amazing scientist who sparked my interests in condensed matter physics and helped guiding me onto this path. I am very thankful for the time working with her.

I am fortunate to have learned from the expertise and wisdom of the postdocs. These people are: Jiun-Haw Chu, Phillip K. Walmsley, Matthias Ikeda, Harlyn Silverstein, Pierre Massat, Maja

Bachmann, and Linda Ye. When I first came in and felt my way around as a researcher, Jiun-Haw is always there to help me with crystal growth and cryostats. Watching him work inspired me, as he is one of the best experimentalists I know. Harlyn came into the lab and brought in his crystal growth expertise and really broadened our horizon on the subject. The documentations he made is still referred to until this day. I really enjoy hanging out with Pierre as he always shares his many enthusiasm, and he has great humor. He brought so much expertise and much more into the lab. He introduced me to ballroom dancing and surfing, which I really enjoy it even though I suck at both of them. (I sprain my ankle during surfing, how is that even possible?) Phil comes in just about a few months after me, and his sexy British accent brought me back to England. I have enjoyed so many conversations with him about condensed matter physics, and he never failed to elucidate me with his knowledge. I also enjoyed talking politics with him, as he is probably closest to me ideologically. Linda joined the group during my last year. She and I hit it off from the start as we talked a lot about Asian cooking (thanks for recommending me that garlic chili oil). I am impressed by how prolific and innovative she is - with less than a year, she has already proposed and worked on several projects. She also gave me a lot of good advice on the last chapter of my thesis, especially with the measurement in magnetic field. I first met Maja in Japan during the SCES conference, and I am so glad that I had the pleasure to work with her and collaborate with her on the work that later became the last chapter of this thesis. Her presence in the lab is really valuable both scientifically and culturally. I really appreciate her especially for helping with the FIB and giving me many good suggestions on running experiments, and also suggestions for good restaurants.

I would like to express my utmost gratitude to Matthias Ikeda. He joined the lab at the time when I struggled the most after I failed my two previous projects. He and I picked up a major project, which later became the first experimental chapter of this thesis. I have learned so much, and I can safely say that because of the experience working with him on that project, I was able to walk on my own as a scientist. Although what I learned from him is so valuable, I value my friendship with Matthias even more. We share many interests and had so many good memories as he brought me to archery, fishing, camping, and more. We are both competitive when it comes to ping pong and cooking.<sup>1</sup> I hope our friendship continues as we both move on to the next phases of our life.

I also have the pleasure to work alongside my fellow graduate students in the lab: Paula Giraldo-Gallo, Max Shapiro, Alex Hristov, Elliott Rosenberg, Johanna Palmstrom, Josh Straquadine, Matt Sorensen, Kaan Alp Yay, Anisha Singh, and Mark Zic. My overlap time with Paula was far too short, as she was leaving when I arrived. I was hoping to know her more, as she is such a wonderful person and an amazing scientist. I have an honor to inherit her desk, which is the primary base I used to work during my time here. Max is one of the nicest people I know, and I learned a lot about American culture from him. He is wicked smart and has a great sense of humor. He gave

---

<sup>1</sup>I shall admit in a small print here that you made better sushi than me in the last competition, but mark my word, I will eventually get that sweet revenge.

suggestions on my thesis defense and kindly helped me with my CV and job applications, which I am really grateful for. Alex was very nice to me, as he taught me many things from how to cryo-clean the DilFridge to his spin-dimer projects. I am always impressed by the amount of intellect (and vocabulary) he has every time we have a conversation. Max and Alex have contributed greatly to the group. The AC elasto-resistivity and Transverse elasto-resistivity that they developed are major tools that I used in this thesis.

Elliott was the first graduate student I met in the lab as he was the one who gave me the lab tour. After knowing him for a while, I see many similarities between the two of us, and he became one of my best friends. I still remember the time we have conversations about my existence as an experimental scientist and sharing each other's struggles in the lab. Looking back, I think we both did very well, and we should be proud of our achievements. I hope this friendship continues, and I am looking forward to many rounds of golf together in the future.

Johanna's presence transformed the lab culture in so many great ways. I remembered that only a month or so after she joined, the bonds between lab members grew much stronger. She has helped me so much in the lab, from crystal growth to cryostat to MatLab coding. I will treasure the time we both spent in Japan, and also thank you for giving me the honor to photograph your wedding. I am so glad she pursued her academic career, and I have no doubt that she will be very successful.

Josh is a role model to me in many ways. His work ethic is through the roof, and his engineering skill is something I have never seen before. I also enjoyed hearing him practice saxophone late in the evening when he has growths in the image furnace. Matt brought positivity into the lab like no one has ever done. Just thinking of him really makes me smile. My conversation with him is always illuminating as he has profound understandings of various topics from condensed matter physics to group theory to politics. I still remember the time he gave Elliott and me a three-hour lecture on the history of the middle-eastern conflict. That was intense. I like to say this to you, Matt, as a theoretical leaning person like you, I know that you may feel struggles as an experimentalist, but you're on the right path. I do not doubt that you will do well. Keep going at it.

To Kaan, Anisha, and Mark, you guys are the bright future of the lab. I do mean it. Your enthusiasm for science is contagious, and you already have so much knowledge even in your early years as graduate students. The Fisher group is really in good hands. Having said that, if there is one regret during my time in Fisher group, it is that I did not do a good job in guiding and helping you guys. So if you feel like my perspective can be useful to you, please do not hesitate to reach out to me, and I will do my best!

I also have so many friends at Stanford and in communities that I am a part of. I thank all my friends in the Thai community in the bay area: Tee, Golf, Po, Mery, Wai, Tum, North, Pinpin, Mike, Win, Toey, Pim, Payut, Earth, Paul, Gina, Matt, Wendy, and so many others. I thank people in the music department, especially Prof. Kumaran Arul and Prof. George Barth, who taught me the piano, and friends in the music department: Yang Joonseok, Patrick Kim, Ben Salman, Jaehyun

Park, Laurie Kost, and Scott Reid (who also briefly joined Fisher lab) and so many others. I also thank people in other communities: people in badminton and table tennis clubs and people in Sokka Gakkai International.

I would like to thank my extended family members, especially My Aunt Chang, my cousins Pong and Pupa, who always encouraged me during my time here.

To my girlfriend Navi Tansaraviput, thank you for always be there for me especially during this last year when the pandemic hit and things started getting very difficult, especially with my mental health. You gave my strength during this hard time. I am truly blessed to have someone like you in my life.

Lastly and most importantly, my parents and my brother. I love you all so much. To my brother, you are such an inspiration to me. Thank you for your enthusiasm and encouragement. I could not have asked for a better brother. To my father, you have sacrificed almost everything and singlehandedly raised both of us for more than 20 years. I am eternally grateful, and I dedicate this thesis to you. And to my late mother, thank you for everything. Wherever you are, if you are watching me, I hope I made you proud.

# Contents

<b>Abstract</b>	<b>v</b>
<b>Acknowledgments</b>	<b>vii</b>
<b>1 Introduction</b>	<b>1</b>
1.1 Big picture . . . . .	1
1.2 A brief introduction to iron-based superconductor . . . . .	2
1.2.1 Crystal and electronic structure . . . . .	2
1.2.2 Phase diagram, magnetism, and superconductivity . . . . .	4
1.2.3 Electronic nematicity in iron pnictide . . . . .	6
1.2.4 Quantum criticality . . . . .	7
1.3 Effect of strain on nematic order . . . . .	9
1.3.1 Representation theory for strain in $D_{4h}$ point group . . . . .	10
1.3.2 Effect of strain on $T_S$ . . . . .	14
1.3.3 Effect of strain on transport properties: Elastoresistivity . . . . .	15
1.3.4 Effect of strain on thermodynamics properties: Elastocaloric effect . . . . .	19
1.4 Thesis layout . . . . .	21
<b>2 Experimental Methods</b>	<b>22</b>
2.1 Material preparation for strain measurements . . . . .	22
2.2 Application of stress to the materials . . . . .	23
2.2.1 Lead-Zirconium-Titanate (PZT) stack . . . . .	24
2.2.2 Uniaxial stress cell . . . . .	25
2.2.3 Hydrostatic pressure . . . . .	29
2.3 Measuring the critical temperatures $T_S$ of the nematic phase transition . . . . .	29
2.3.1 Resistivity . . . . .	30
2.3.2 Elastoresistivity . . . . .	31
2.3.3 Elastocaloric effect . . . . .	33
2.4 Measurement of nematic susceptibility . . . . .	35

<b>3</b>	<b>Establishing symmetry-breaking strain as a tuning parameter</b>	<b>39</b>
3.1	Introduction . . . . .	39
3.2	Experimental Methods . . . . .	42
3.3	Results and Discussion . . . . .	45
3.4	Summary . . . . .	48
3.A	Sample preparation . . . . .	50
3.B	Experimental Methods . . . . .	50
	3.B.1 Uniaxial stress experiments . . . . .	51
	3.B.2 Hydrostatic pressure experiments . . . . .	53
3.C	Finite element simulations . . . . .	54
	3.C.1 Elastic properties of $\text{Ba}(\text{Fe}_{0.975}\text{Co}_{0.025})_2\text{As}_2$ . . . . .	56
3.D	Strain decomposition . . . . .	56
<b>4</b>	<b>Nematic Quantum Criticality Revealed by Strain Tuning</b>	<b>58</b>
4.1	Introduction . . . . .	58
4.2	Effect of Strain of Differing Symmetry to the Critical Temperature $T_S$ . . . . .	60
4.3	Result . . . . .	63
	4.3.1 The effect of variation in elastic moduli to the observed power-law behavior . . . . .	66
4.4	Scaling collapse of $T_S$ as a function of combined tuning parameters . . . . .	67
4.5	Discussion . . . . .	68
<b>5</b>	<b>Probing nematic susceptibility while continuously tuning the system with strain</b>	<b>72</b>
5.1	Introduction . . . . .	72
5.2	The Trilinear coupling . . . . .	73
5.3	Measurement of the Hall viscosity coefficient . . . . .	75
5.4	Experimental setup . . . . .	78
5.5	Result and discussion . . . . .	79
5.A	Strain response of the PZT . . . . .	82
5.B	Comments on the strain dependence of the Hall coefficient . . . . .	84
<b>6</b>	<b>Final summary and future works</b>	<b>85</b>
6.1	Summary of this thesis work . . . . .	85
6.2	Future outlooks . . . . .	86
	<b>Bibliography</b>	<b>88</b>

# List of Tables

1.1	Character table for the $D_{4h}$ crystallographic point group. The list of symmetry elements are shown on the top row, and the irreducible representations are shown on the left column. Reproduced from [51]. . . . .	10
1.2	Product table for the $D_{4h}$ crystallographic point group. Reproduced from [51]. . . . .	13
1.3	Effect of strains of each irreducible representation on the nematic phase transition. The first column shows strains of each irreducible representation. The second column lists the corresponding allowed interaction terms to leading orders. Note that these terms must be symmetry preserving, i.e. $A_{1g}$ quantities. The third column lists the effect of strains of each symmetry on the nematic phase transition. Note that the order parameter can be induced by $B_{2g}$ strain, and hence there will be no true thermodynamic phase transition in the presence of $B_{2g}$ strain. In practice, this strain would smear the signature of the phase transition, turning a sharp feature into a crossover. . . . .	15
3.1	Summary of the mechanical properties used for our finite element simulations. For the tetragonal $Ba(Fe_{0.975}Co_{0.025})_2As_2$ , the Young's modulus is given for stress along [100] ( $E$ ) and [001] ( $E'$ ). In addition, the table also shows the in-plane ( $\nu$ ) and out-of-plane Poisson ratio ( $\nu'$ ), as well as the in-plane ( $C_{66}$ ) and out-of plane shear moduli ( $C_{44}$ ). These properties correspond to the mechanical properties of $Ba(Fe_{0.963}Co_{0.0375})_2As_2$ at 100 K, as found by resonant ultrasound spectroscopy [92]. The mechanical properties of the mounting epoxy (Devcon 2-ton epoxy) at 100 K were assumed to be slightly softer compared to filled Stycast 2850FT [64]. . . . .	54
5.1	There are three terms that contribute to the Hall resistivity in equation 5.11: the Hall effect, the resistivity anisotropy induced by $B_{2g}$ strain, and the resistivity anisotropy induced by the trilinear coupling. These trilinear coupling can be distinguished completely from the other terms by looking at the the field dependence and the frequency dependence of the signal, and the phase of the signal relative to that of the induced strain. . . . .	77

# List of Figures

1.1	Crystal structure of $\text{BaFe}_2\text{As}_2$ - $\text{ThCr}_2\text{Si}_2$ ‘122’ crystal structure with $I4/mmm$ space group and $D_{4h}$ point group. Figure reproduced from [9] with permission of the American Physical Society. . . . .	3
1.2	(a) Top view of the crystal structure of $\text{BaFe}_2\text{As}_2$ . The green and the blue squares indicate one-iron and two-irons unit cells, respectively. (b) 2D Fermi surfaces in the one-iron unit cell. Dash green line indicates the Brillouin zone associated with the one-iron unit cell. (c) 2D Fermi surfaces in the two-iron unit cell after band folding with the wave vector indicated by the blue arrow in (b). Reproduced from [13] with permission of IOP publishing. . . . .	4
1.3	Phase diagram of $\text{Ba}(\text{Fe}_{1-x}\text{Co}_x)_2\text{As}_2$ . Underdoped sample undergoes a electronic nematic transition, which changes the structure from tetragonal to orthorhombic. At temperature slightly below that, it undergoes a magnetic transition. The two phases are suppressed with cobalt doping, and superconductivity can emerge. The dash yellow and green lines are extrapolation of the data points. There is a report that back bending of the phases transition happens underneath the superconducting dome [16], indicating competition between the two phases and superconducting phase. Reproduced from [7] with permission of the American Physical Society. . . . .	5

1.4	(A) A generic quantum critical phase diagram. At the parent state, system undergoes a phase transition to an ordered state at temperature $T$ . This phase can be suppressed by applying a tuning parameter $g$ . Quantum phase transition happens at $g_c$ where the phase transition occurs at zero temperature. If this is a continuous phase transition, this point is called a quantum critical point. The effect of quantum critical point can be seen at higher temperature in the <i>quantum critical fan</i> , where the physical properties is dominated by the thermal excitation of quantum critical ground state. Dash lines denote the cross-over between classical and quantum critical region. (B) Signature of quantum criticality in $\text{BaFe}_2(\text{As}_{1-x}\text{P}_x)_2$ presented in its phase diagram, where $x$ denotes phosphorus concentration. Color scale represents $\alpha$ from the relation $\rho = \rho_0 + AT^\alpha$ . Blue color ( $\alpha \sim 2$ ) and red color ( $\alpha \sim 1$ ) represent non-Fermi and Fermi liquid regimes, respectively. The light green squares and dark green diamonds represent the effective mass normalized by the band mass $m^*/m_b$ measured by the de Haas van Alphen and specific-heat measurement, respectively. Reproduced from [2] with the permission of the Annual Review of Condensed Matter Physics. . . . .	8
1.5	Symmetry coordinates of strain in $D_{4h}$ point group is summarized in this figure. These strains belongs to different irreducible representation. Two types of strain belong to $A_{1g}$ irreducible representation, which preserves symmetry when deform: in plane $A_{1g,1}$ and out of plane $A_{1g,2}$ . Two types of strain belong to B irreducible representation, which breaks $C_4$ rotational symmetry. These are the $B_{1g}$ which break diagonal mirror planes ( $x = y$ and $x = -y$ ), and $B_{2g}$ which breaks horizontal mirror planes ( $x = 0$ and $y = 0$ ). The vertical shears belongs to the two dimensional $E_g$ irreducible representation. . . . .	12
2.1	(A) The design of the <i>Razorbill</i> CS100 cell. Samples is deformed by applying voltages into the outer and the inner PZT stacks. This design compensates for thermal expansion of the PZT (the inner and outer will expand at the same rate, cancelling out each other), and also converts all the length change of the PZT into the sample. (B) Picture of a working <i>Razorbill</i> cell. A Cernox thermometer is attached and thermally anchored to the cell body. Picture taken by Matthias Ikeda. (C) Schematic showing the assembly procedure. The sample is glued on top of bottom mounting plates and is electrically separated by thin cigarette papers. (D) shows the final arrangement where the top mounting plates are glued on top of the sample and affixed to the cell by screws to provide uniform strain along the z-direction. . . . .	26

2.2	(a)(d) Temperature and strain derivatives of the resistance and internal energy $U$ in $\text{Ba}(\text{Fe}_{0.975}\text{Co}_{0.025})_2\text{As}_2$ in proximity to the successive nematic and magnetic transitions, each plotted against a single corresponding axis on the left. The heat capacity $(\frac{\partial U}{\partial T})_\epsilon$ is shown in black. The characteristic mean-field step at $T_S$ is rounded due to inhomogeneity, where with a width of approximately 1K. This figure shows that resistivity (green), elastoresistivity (blue), and elastocaloric effect (red) are appropriate tools for determination of the critical temperatures. Reproduced from [71] with the permission of the American Physical Society. . . . .	31
2.3	Schematic explanation of the amplitude demodulation method. The oscillating voltage signal of frequency $f_c$ is modulated by the change of resistivity via elastoresistivity at frequency $f_s$ . This resulted in the signal in the middle panel which is described by 3 Fourier components. The amplitude of the resistivity change due to strain can be measured by lock in to the sideband signal. The mathematical description can be found in the main text. . . . .	32
2.4	<b>Measurement of the critical temperature <math>T_S</math>.</b> (A) Resistivity traces and their temperature derivatives for a prototypical $x = 4.8\% \pm 0.2\%$ under various hydrostatic pressures. The step like anomalies in $d\rho/dT$ found at high temperature of each trace signify the nematic phase transition. $T_S$ is then located at the peak of $d^2\rho/dT^2$ . (B) sideband traces and their temperature derivatives for a prototypical $x = 4.8\% \pm 0.2\%$ under various uniaxial stresses. The top panel shows the sideband signal which is directly proportional to the elastoresistivity (ER). The nematic phase transition occurs at the step-like anomalies in the ER traces. $T_S$ is thus located at the peaks of $d(ER)/dT$ . Reproduced from [72] with the permission of the American Association for the Advancement of Science. . . . .	34
2.5	Thermal transfer function taken at various temperature. Reproduced from [61] with the permission of the American Institute of Physics. . . . .	35
2.6	Elastocaloric effect with strain in the $B_{1g} + A_{1g}$ configuration measured as a function of temperature for different offset strain. The rounded step-like feature associated with $T_S$ is clearly visible, and its strain dependence can be readily extracted. Reproduced from [61] with the permission of the American Institute of Physics. . . . .	36
2.7	Figure illustrates measurement of elastoresistivity in transverse configuration. Sample is glued $45^\circ$ to the strain axis. The actual transverse voltage can be measured by subtracting the longitudinal contamination from the measured transverse voltage as explained in the main text. . . . .	37

- 3.1 Schematic representation of strains experienced by a tetragonal material while held under (a) hydrostatic pressure, and (b) uniaxial stress applied along the [100] direction. Black arrows indicate stress. The strain tensor (right side of symbolic equations (a) and (b)) is derived by multiplying the stiffness and the stress tensor (left side). White arrows in panel (a) and (b) indicate the orientation of the tetragonal crystal axes. In each case, the strain tensor experienced by the material is decomposed into irreducible representations of the crystal symmetry. For materials with regular mechanical properties (i.e. a positive out-of-plane Poisson ratio and an in-plane Poisson ratio smaller than 1), the symmetric strain modes  $\epsilon_{A_{1g},i}$  share the same sign (are both compressive) during hydrostatic pressure experiments, but have opposite sign during uniaxial stress experiments. Panel (c) illustrates in-plane deformations as well as the associated preserved symmetries (white lines). While symmetric  $A_{1g}$  strain preserves  $C_4$  rotational symmetry (white arrow) as well as vertical, horizontal, and diagonal mirror planes (white dash dotted lines), antisymmetric  $B_{1g}$  and  $B_{2g}$  strains lower the primary rotational symmetry to  $C_2$  and break diagonal and vertical mirror planes, respectively. . . . . 41
- 3.2 (a) Electrical resistivity of  $\text{Ba}(\text{Fe}_{0.975}\text{Co}_{0.025})_2\text{As}_2$  as a function of temperature determined during a uniaxial stress experiment. For each temperature sweep (warming) shown here, the sample is held at a constant strain,  $\epsilon_{xx}^{\text{disp}}$ , indicated by the color scale (blue data points indicate compressive strain, beige points tensile strain, and cyan colored data small strain around the strain neutral point). Panel (b) and (c) show the first and second derivative of the resistivity with respect to temperature. Panel (d) shows  $T_S$  and  $T_N$  versus nominal strain  $\epsilon_{xx}^{\text{disp}}$ . The red lines are fits using a second order polynomial resulting  $T_S(\epsilon_{xx}) = 100 - (521 \pm 4)\epsilon_{xx} - (28300 \pm 1100)\epsilon_{xx}^2$ , and  $T_N(\epsilon_{xx}) = 94.5 - (629 \pm 2)\epsilon_{xx} - (24700 \pm 500)\epsilon_{xx}^2$ . . . . . 43
- 3.3 (a) Temperature dependence of the electrical resistivity  $\rho$  of  $\text{Ba}(\text{Fe}_{0.975}\text{Co}_{0.025})_2\text{As}_2$  for a range of hydrostatic pressures  $p$  determined during slow warming temperature sweeps. Panel (b) and (c) show the first and second derivative with respect to temperature, respectively. The dotted lines in panel (c) shows second derivatives calculated neglecting resistivity data below  $T_N + 1\text{K}$ , avoiding overlap of the smoothed signatures of the features associated with  $T_N$  and  $T_S$ . Similar to Fig. 3.2, blue colored symbols indicate compressive strains. Panel (d) again shows the structural and antiferromagnetic transition temperature as a function of pressure. The red lines in panel (d) are linear fits to the data. . . . . 44

3.4	Normalized linear response of the structural transition to symmetric $\epsilon_{A_{1g},1}$ , and $\epsilon_{A_{1g},2}$ strain during hydrostatic pressure and uniaxial stress experiments. The cyan and purple vertical planes indicate the relative combination of symmetric strains induced during hydrostatic pressure and uniaxial stress experiments, respectively. Experimental data are shown by the cyan (hydrostatic pressure) and purple stars (uniaxial stress), respectively. Linear fits are shown by red lines. The yellow plane defined by these two lines describes the material's linear response to symmetric strain. . . . .	46
3.5	Normalized non linear response of the coupled nematic/structural transition temperature to strain during hydrostatic (cyan stars, top axes) and uniaxial stress (purple stars, bottom axes) experiments. The quadratic contribution evident in the uniaxial stress data is solely due to antisymmetric $B_{1g}$ strain. Red line shows fit to a quadratic function. The origin of the kink near zero strain is currently unknown. The feature is, however, smaller than the error bars and has no statistically significant impact on the fit . . . . .	47
3.6	(a) $Ba(Fe_{0.92}Co_{0.08})_2As_2$ crystal mounted on a Razorbill CS100 cell using bottom and top mounting plates. Panel (b) sketches a sample mounted onto bottom mounting plates, panel (c) sketches a cross sectional view. . . . .	51
3.7	Comparison of the in-plane thermal expansion of $Ba(Fe_{0.92}Co_{0.08})_2As_2$ [91] and the thermal expansion of Ti. [96] . . . . .	52
3.8	(a) Resistivity as a function of temperature for different strains $\epsilon_{xx}^{disp}$ , applied along the tetragonal [110] axis. (b) Derivative of the electrical resistivity with respect to temperature. The step like feature associated with the structural phase transition is suppressed quickly and is fully smeared for strains on the order of $\epsilon_{xx}^{disp} \approx 3 \times 10^{-3}$ . . . . .	53
3.9	(a) Model used for the finite element simulations presented here. The dashed-dotted blue lines on the top view show the mirror planes $m_1$ and $m_2$ used to reduce the model size. (b) Results of our finite element simulation shown on the cross section of our model. (c) Normal strain $\epsilon_{xx}$ along the center line in $x$ direction on the top and bottom surface of the sample. The vertical black solid lines mark the position of the mounting plate edges. Nominally, a strain of $\epsilon_{xx}=1\%$ was applied. The strain relaxation within the mounting plates and the glue result in a strain transfer ratio of 0.7. . . . .	55

- 4.1 **Consequences of uniaxial stress along [100]** (A) In a tetragonal system, deformation caused by the uniaxial stress applied along [100] direction can be expressed as the combination of the symmetry preserving strain  $\epsilon_{A_{1g}}$ , and orthogonal antisymmetric strain  $\epsilon_{B_{1g}}$ . The ratio of these strain components depends on the elastic moduli of the material. Note that orthogonal antisymmetric  $B_{1g}$  strain is defined as  $\epsilon_{B_{1g}} = (\epsilon_{xx} - \epsilon_{yy})/2$ , while symmetry preserving  $A_{1g}$  strain in this scenario is a combination of the in-plane  $\epsilon_{A_{1g,1}} = (\epsilon_{xx} + \epsilon_{yy})/2$ , and out of plane  $\epsilon_{A_{1g,2}} = \epsilon_{zz}$ . Dashed lines indicate the undeformed tetragonal unit cell. (B) The variation of coupled nematic/structural phase transition temperature as a function of the measured strain along [100],  $\epsilon_{xx}$ , for a representative sample with cobalt concentration  $x = 4.8\% \pm 0.2\%$ . The leftmost graph (purple) shows the (linear + quadratic) variation caused by uniaxial stress. The center graph (blue) shows the linear contribution from  $A_{1g}$  strain, and the rightmost graph (red) shows the quadratic contribution from  $B_{1g}$  strain. (C) Schematic  $T_S - \epsilon_{A_{1g}} - \epsilon_{B_{1g}}$  phase diagram. The experimental path lies along the straight line between  $\epsilon_{A_{1g}}$  and  $\epsilon_{B_{1g}}$  axes. The effects of these two tuning parameters are generally uncorrelated. However, in the presence of strong quantum critical fluctuations, the coefficients of both the linear and quadratic strain responses (resulting from the response to the  $A_{1g}$  and  $B_{1g}$  strains, respectively) are both related to the zero-strain transition temperature as  $1/T_0^{1/\theta}$ . . . . . 61
- 4.2 **Response of  $T_S$  to applied hydrostatic pressure for various compositions of  $\text{Ba}(\text{Fe}_{1-x}\text{Co}_x)_2\text{As}_2$ .** The green circles represent the measured critical temperature  $T_S$  as a function of applied hydrostatic pressure  $P$ . The black lines represent the linear fit to the data. It can be seen that in all compositions, the variation is linear. Thus the quadratic variation in uniaxial stress experiment is exclusively caused by the orthogonal antisymmetric  $B_{1g}$  strain. . . . . 62
- 4.3 **Response of  $T_S$  to applied uniaxial stress along [100] in various cobalt concentrations of  $\text{Ba}(\text{Fe}_{1-x}\text{Co}_x)_2\text{As}_2$ .** (A) The purple circles represent the measured critical temperature  $T_S$  as a function of the deduced strain  $\epsilon_{xx}$ . The black lines represent linear + quadratic fits to the data. As the cobalt concentration approaches the critical doping of  $x_c \sim 6.7\%$ , both the quadratic and linear coefficients increase. Panel (B) and (C) represent the linear and quadratic constituents due to  $A_{1g}$  and  $B_{1g}$ , respectively. . . . . 64

- 4.4 **Power law divergence of  $dT_S/d\epsilon_{xx}$  and  $d^2T_S/d\epsilon_{xx}^2$  as a function of cobalt concentration  $x$  in  $\text{Ba}(\text{Fe}_{1-x}\text{Co}_x)_2\text{As}_2$ .** (A) The linear coefficient of the variation of  $T_S$  caused by symmetric  $A_{1g}$  strain, and (B) the quadratic coefficient caused by antisymmetric  $B_{1g}$  strain, each case normalized by the zero-strain critical temperature  $T_0$ . The schematic insets illustrate the appropriate irreducible representations of strain for the two cases. Both the linear and the quadratic coefficient diverge as the cobalt concentration approaches the critical doping of  $x_c \sim 6.7\%$  (vertical dashed line). (c) The same normalized coefficients as a function of zero-strain critical temperature  $T_0$  shown in a log-log scale. The linear behavior seen in this plot at low temperatures indicates similar power law behavior for both symmetry channels. The slopes of the linear regimes are equal to the inverse critical exponent  $1/\theta$ , which is found to be  $1/\theta = 1.75 \pm 0.2$  and  $1/\theta = 1.87 \pm 0.7$  for  $A_{1g}$  and  $B_{1g}$  strain respectively; these values agree within a standard deviation. Note that extracting statistically significant quadratic coefficients requires data extending to relatively large strains. For two experiments (two extra data points in the blue traces), this strain regime could not be reached before the mechanical failure of the sample, so only the linear coefficients are shown. . . . . 65
- 4.5 **Theta scan.** The plot shows the R-square value of the least square fit of Eq.(4.13) for various  $\theta$  values ranging from 0.4 – 0.65.  $\theta = 0.52 \pm 0.02$  give the best fit with R-square of 0.994. . . . . 69
- 4.6 **Scaling collapse of non-thermal tuning parameters.** (A) The scaling collapse described in Eq. 4.12, in which  $T_S^{1/\theta}$  is plotted versus  $\delta$ . The best fit value  $\theta = 0.52 \pm 0.02$  is extracted using the method explained in Section 4.4. Symbols represent samples with differing dopings. The data is expected to collapse onto a single line in the quantum critical regime which is observed for samples within a range of Co concentrations between  $x = 4.8\%$  and  $6.2\%$ . This regime is magnified in the plot in panel (B), which shows a collapse over almost a decade of  $\delta$ . . . . . 69

- 4.7 **Quantum criticality in  $\text{Ba}(\text{Fe}_{1-x}\text{Co}_x)_2\text{As}_2$  phase diagram.** (A) The normalized linear  $\alpha/T_0$  (left axis) and quadratic coefficients  $\beta/T_0$  (right axis), scaled with the expected zero-strain critical temperature dependent  $T_0^{-1/\theta}$ . These quantities are expected to be constant in the quantum critical regime, which spans the higher dopings, as suggested by the dotted line. The green shading represent the ratio of these scaled coefficients with their saturated value. (B) Phase diagram of  $\text{Ba}(\text{Fe}_{1-x}\text{Co}_x)_2\text{As}_2$  [7]. Power law behavior is observed for materials with a cobalt concentration between  $x = 4.8\% \pm 0.2\%$  all the way to  $x = 6.2\% \pm 0.2\%$ , above which  $T_S$  is unobservable due to the presence of superconductivity. This power-law behavior signifies the presence of strong nematic fluctuation of quantum origin due to the presence of the nematic QCP at  $x_c$ . Note that the dotted lines in (B) denotes the phase transition lines which presumably backbend inside the superconducting state [16]. . . . . 71
- 5.1 (A) The geometric of the sample. Biaxial strain  $\epsilon_\alpha = \epsilon_{\alpha,0} + \epsilon_{\alpha,1} \sin(\omega_s t)$ m, ( $\alpha = xx, yy$ ) is induced by gluing the sample onto the PZT stack. The  $\epsilon_{\alpha,0}$  is used to tune the critical temperature  $T_S$ , while the oscillating part  $\epsilon_{\alpha,1} \sin(\omega_s t)$  is used to induce the nematic order parameter with magnetic field  $H_z$ . (B) the phase diagram comparing the three terms in Eq.5.10. The Hall resistivity, and the anisotropy induced by the  $B_{2g}$  strain is in phase with the strain. The anisotropy induced by the trilinear coupling is in quadrature with strain and is linearly dependent on frequency. . . . . 76
- 5.2 (A) Typical microstructure with 6-point-contact geometry. (B) Top view of the microstructure. Labels indicates the current path, and the longitudinal voltage  $V_x$  and the transverse voltage  $V_y$ . These scanning electron microscope pictures were taken inside of the FIB machine by M.D. Bachmann . . . . . 78
- 5.3 (A) The antisymmetrized sideband from the Hall channel. It is linear as a function of the applied magnetic field, and the slope increases as a function of strain frequency. This plot is smoothen using the smoothing spline method in MatLab. (B) The slope  $\frac{\partial}{\partial H_z} S_{xy,t}^{\text{antisym}}$  is plotted as a function of strain frequency, revealing a linear dependence. The slope of this plot,  $\frac{\partial^2}{\partial f_s \partial H_z} S_{xy,t}^{\text{antisym}}$ , is directly proportional to the Hall viscosity coefficient. (C)  $\frac{\partial^2}{\partial f_s \partial H_z} S_{xy,t}^{\text{antisym}}$  is plotted as a function of temperature. The expected Curie-Weiss temperature dependence was not observed, implying the observed Hall viscosity coefficient may come from other origins. . . . . 80
- 5.4 Frequency response of the PZT obtained by attaching a strain gauge to the back of the PZT and measured with amplitude demodulation method described in Section 2.4 83

# Chapter 1

## Introduction

### 1.1 Big picture

Several unconventional superconductors and high-temperature superconductors have phase diagrams where ordered states of one sort or another are suppressed by some tuning parameter such as chemical substitution or hydrostatic pressure. In all of those cases, it is apparent that superconductivity is related to the ordered state in some way. Certainly, they seem to be antagonistic: superconductivity is absent when the ordered state is very strong, yet also is absent very far away from the ordered state, indicating that these are not simply competing phases [1]. Such a phase diagram presents many questions. The most basic question is whether there is a quantum critical point underneath that superconducting dome [2], or whether this is avoided by a number of issues including disorder effects [3, 4]. More subtly, one might ask whether this quantum critical point, if present, matters to the superconductivity beyond simply marking the transition from a region in the phase diagram where an ordered state exists to where it does not. My dissertation will not address the latter question, but it will address the first question, specifically whether the quantum critical point exists, or, more precisely, whether the system behaves as if there is a quantum critical point at the finite temperature at which we perform our experiments.

The particular material system central to my experiments is the Fe-based superconductors. The specific phase transition that I look at is the (electronic) nematic phase transition, which I will discuss later in this chapter. Nematic order breaks rotational symmetry but not translation nor time-reversal symmetry. Since nematic order only break point symmetries, uniform strain (induced, for instance, via external stresses), plays a very special role. Indeed there is a bilinear coupling between nematic order and strain that breaks the same symmetry. As a consequence, strain is an important tuning parameter to the nematic order; and one of the key elements of my thesis is to study the effect of strain of differing symmetry on the nematic order and use them to tune the nematic order. One particular observation from this technique is the observation of power-law

behavior of the critical temperature of the nematic phase transition as a function of non-thermal tuning parameters, providing the first direct evidence for nematic quantum criticality. This will be discussed in Chapter 4.

While the tools and techniques that I introduce in this thesis are applied solely in the context of electronic nematic order in Fe-based superconductivity, these are more generally applicable in other material systems. This is undoubtedly true in the case of order parameter that breaks the same symmetry as strain, but also for any material with a hydrostatic pressure-based phase diagram, which will benefit from the decomposition of strain (see Chapter 3). In addition, the biquadratic coupling between symmetry breaking strain and order parameter is almost always allowed by symmetry, making symmetry-breaking strain a very powerful tool in studying quantum materials.

## 1.2 A brief introduction to iron-based superconductor

In 2008, a new type of superconductor,  $\text{LaFeAs}(\text{O}_{1-x}\text{F}_x)$ , was discovered with superconducting transition temperature  $T_C \sim 26\text{K}$  [5]. It quickly gained interest amongst the condensed matter physics community, as it features a simpler phase diagram compared to the cuprate superconductors, becoming a new promising avenue for studying high-temperature superconductivity, quantum phase transitions, and quantum criticality. The family of Fe-based superconductors can be classified into two groups: the pnictides and the chalcogenides [6]. These two groups have a few things in common. Both the pnictides and the chalcogenides comprise a common structural motif: Fe-pnictogen (or Fe-chalcogens) interconnected tetrahedra structure, which hosts quasi-2d conduction electrons [7]. The stoichiometric compound usually undergoes a coupled nematic/structural phase transition and a magnetic phase transition at a slightly lower temperature. These phases are suppressed by either chemical substitution [7] or hydrostatic pressure [8], and a superconducting dome emerges before the phases are fully suppressed. It is speculated that there may be a quantum critical point beneath the superconducting dome ([2] and references therein), which raises the question as to what role quantum criticality plays in the emergent unconventional superconductivity. The discussion in this thesis will be around the representative material  $\text{Ba}(\text{Fe}_{1-x}\text{Co}_x)_2\text{As}_2$ . This material has several advantages that are suitable for exploring electronic nematicity with strain: the single crystals obtained from the flux growth method are plenty large for mounting on a uniaxial stress cell; the nematic and the magnetic phase transitions are well-separated at higher cobalt concentration, making it easier to distinguish the behavior of each of them; and the amount of cobalt substitution can be well controlled.

### 1.2.1 Crystal and electronic structure

At room temperature, the stoichiometric parent compound  $\text{BaFe}_2\text{As}_2$  has a  $\text{ThCr}_2\text{Si}_2$  ‘122’ crystal structure with  $I4/mmm$  space group and  $D_{4h}$  point group shown in Fig.1.1. The electronic behavior of  $\text{BaFe}_2\text{As}_2$  can be attributed to the strong Hund’s interaction, and the material from the Fe-based

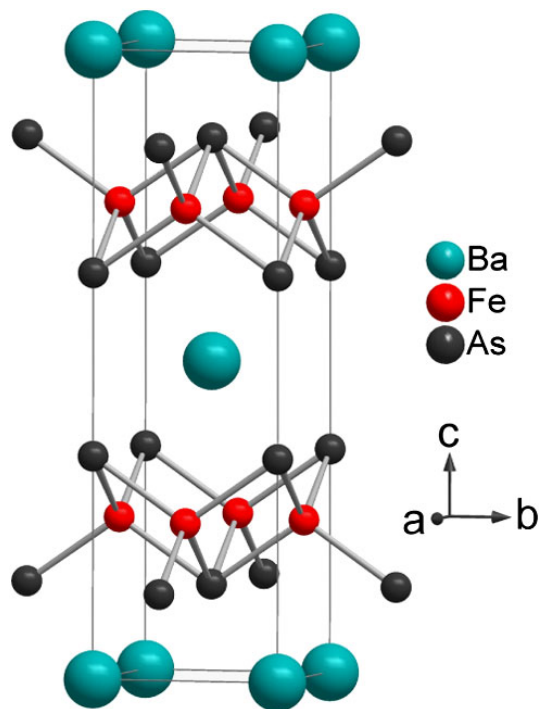


Figure 1.1: Crystal structure of BaFe<sub>2</sub>As<sub>2</sub> - ThCr<sub>2</sub>Si<sub>2</sub> '122' crystal structure with  $I4/mmm$  space group and  $D_{4h}$  point group. Figure reproduced from [9] with permission of the American Physical Society.

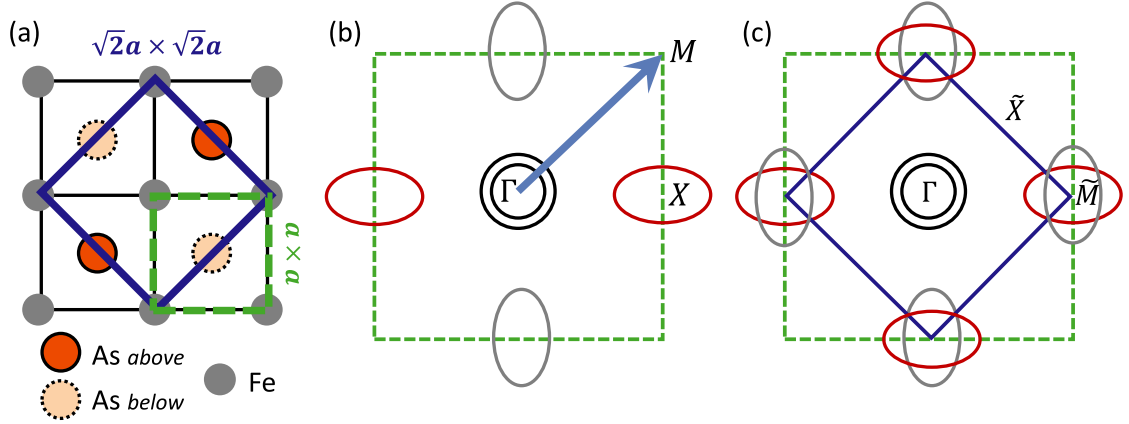


Figure 1.2: (a) Top view of the crystal structure of BaFe<sub>2</sub>As<sub>2</sub>. The green and the blue squares indicate one-iron and two-irons unit cells, respectively. (b) 2D Fermi surfaces in the one-iron unit cell. Dash green line indicates the Brillouin zone associated with the one-iron unit cell. (c) 2D Fermi surfaces in the two-iron unit cell after band folding with the wave vector indicated by the blue arrow in (b). Reproduced from [13] with permission of IOP publishing.

superconductors family can be classified as the ‘Hund’s metal’ [10, 11]. Hund’s metal behavior can be seen in the coherence-incoherence crossover upon increasing temperature. In the normal state, the material is a compensated metal containing equal number of electrons and holes. At a low enough temperature, the electronic structure can be explained by the Fermi-liquid theorem [12]. The Fermi surfaces comprise quasi-two-dimensional cylinders with hole pockets at the center, and electron pockets at the corner of the Brillouin zone as illustrated in Fig.1.2 [12, 13, 14]. In a clean system such as the phosphorus-substituted BaFe<sub>2</sub>(As<sub>1-x</sub>P<sub>x</sub>)<sub>2</sub>, the  $T^2$  dependence of resistivity, which is a transport signature of a Fermi-liquid system, can be observed down to very low temperature [15]. This coherent electronic behavior crosses into an incoherent state at high temperature where it exhibits a bad metal behavior (resistivity  $\sim 400\mu\Omega\cdot\text{cm}$ ) - meaning the resistivity exceed Mott-Ioffe-Regal limit.

## 1.2.2 Phase diagram, magnetism, and superconductivity

The parent compound BaFe<sub>2</sub>As<sub>2</sub> is a tetragonal, paramagnetic phase at high temperature. It undergoes a tetragonal-to-orthorhombic structural transition at the temperature  $\sim 135\text{K}$  and an antiferromagnetic phase transition at a slightly lower temperature. The structural phase transition breaks the  $D_{4h}$  point group in a  $B_{2g}$  fashion - meaning the orthorhombic crystallographic axes are  $45^\circ$  with respect to the tetragonal axes. It is revealed that this structural phase transition is driven by the electronic degrees of freedom [17, 18]. Detail discussion of this phase will be presented in the next section.

The antiferromagnetic phase has the  $(\pi, \pi)$  ordering wave vector (with respect to the ‘two iron’

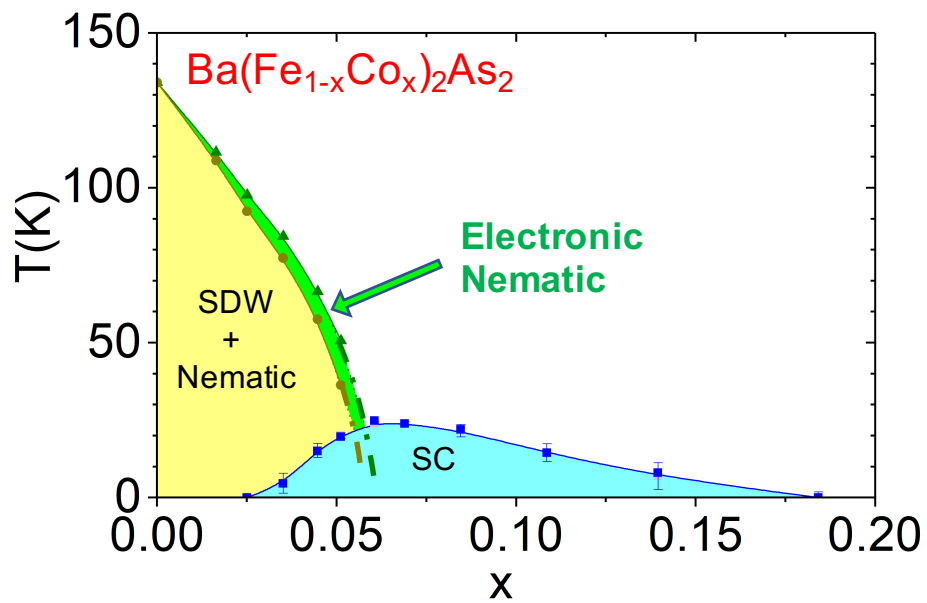


Figure 1.3: Phase diagram of  $\text{Ba}(\text{Fe}_{1-x}\text{Co}_x)_2\text{As}_2$ . Underdoped sample undergoes a electronic nematic transition, which changes the structure from tetragonal to orthorhombic. At temperature slightly below that, it undergoes a magnetic transition. The two phases are suppressed with cobalt doping, and superconductivity can emerge. The dash yellow and green lines are extrapolation of the data points. There is a report that back bending of the phases transition happens underneath the superconducting dome [16], indicating competition between the two phases and superconducting phase. Reproduced from [7] with permission of the American Physical Society.

unit cell). The strong spin-orbit coupling dictates the spin direction to be parallel to the ordering wavevector [19]. It has been proposed that this antiferromagnetism is a spin-density wave state, which is driven by the Fermi-surface nesting [20, 21]. This itinerant picture has a favorable view since the electron and hole Fermi surfaces are well nested by the ordering wave vector  $(\pi, \pi)$  [22]. However, there are also evidences that the itinerant picture cannot sufficiently account for all the phenomenology of the magnetism in this material [23] and a hybrid theory is needed to describe this state.

Superconductivity in Fe-based superconductors usually emerges as the antiferromagnetic phase is suppressed. However, it can also appear in parent compounds of some systems such as FeSe and LiFeAs. The critical temperature of superconducting transition ( $T_c$ ) was found to be as high as 55K in bulk Fe-based superconductor ( $\text{SmFeAsO}_{1-x}\text{F}_x$  [24]) and  $T_c$  of up to 100K was claimed for monolayer FeSe on STO substrate [25], leading some to refer to these as high-temperature superconductors. The standard electron-phonon coupling cannot account for these high superconducting temperatures [26], and therefore an electronic mechanism is proposed [13, 27]. In  $\text{Ba}(\text{Fe}_{1-x}\text{Co}_x)_2\text{As}_2$ , the superconducting phase emerges when nematic and magnetic phases are suppressed. It was quickly proposed that the antiferromagnetic fluctuations are responsible for the pairing, and the associated pairing symmetry is referred to as the  $s^\pm$  wave (see [13] and references therein). Evidence for such a state is provided by the observation of a resonance in inelastic neutron scattering measurements in the superconducting state at the antiferromagnetic wavevector, even for optimally doped compositions for which there is no long range antiferromagnetic order [28]. This pairing gap is isotropic, but the sign changes between electrons and hole pockets. Measurement of thermal conductivity in magnetic field reveals a highly anisotropic s-wave gap structure at higher cobalt concentration [29], which might suggest that antiferromagnetic order reconstructs the Fermi surface by gapping the regions associated with the superconducting gap's minimum.

### 1.2.3 Electronic nematicity in iron pnictide

The interplay between antiferromagnetism and superconductivity seems to be understood within the existing theoretical framework [30]; however, these two are not the only symmetry breaking phases in the material. Preceding the antiferromagnetic phase is the structural tetragonal-to-orthorhombic transition which deforms the material in the  $B_{2g}$  fashion (see Fig.1.5) in two-iron unit cell (Fig.1.2A). This tetragonal-to-orthorhombic transition is ubiquitous in Fe-based superconductors. In this phase, the resistivity anisotropy measured in a de-twinned sample is 500 times larger than the orthorhombicity,  $(a - b)/\frac{1}{2}(a + b)$  [31]. This raises a question of whether the strain is a primary order parameter or merely a conjugate field to a rotational symmetry breaking order driven by the electronic correlation. The elastoresistivity measurement address this problem by measuring the resistivity anisotropy,  $\eta = \frac{\rho_{[110]} - \rho_{[1\bar{1}0]}}{\frac{1}{2}(\rho_{[110]} + \rho_{[1\bar{1}0]})}$ , as a response to applied strain,  $\epsilon$  (both in the same symmetry channel as the orthorhombic distortion) [17]. It is found that the susceptibility  $\chi$  that

relates the two quantities, ( $\eta \sim \chi\epsilon$ ), has a Curie-Weiss temperature dependence. This confirms the latter scenario, where the anisotropy is driven by the electronic correlation. Subsequent elastic stiffness [32], and Raman [33, 34, 35] measurements confirm this perspective.

Borrowing the language from the liquid crystal, the phase is dubbed the *electronic nematic* phase [36]. It is an electronically driven phase that breaks only point group symmetry, but not translational symmetry or time reversal symmetry. There are two schools of thought regarding its origin in the Fe-based superconductors: either it is driven by orbital or spin degrees of freedom. In the former scenario, the interaction between orbitals leads the unequal occupation of  $d_{xz}$  and  $d_{yz}$  orbitals, or in the  $d_{xy}$  orbital hopping ([37] and references therein). The latter scenario happens when the antiferromagnetic order partially melts in a particular fashion, such that the overall spin  $\langle \mathbf{S}_i \rangle = 0$ , but retains its anisotropic correlation to the neighboring site,  $\langle \mathbf{S}_i \cdot \mathbf{S}_{i+x} \rangle = -\langle \mathbf{S}_i \cdot \mathbf{S}_{i+y} \rangle$  (see [38] and references therein). Both of these scenarios have conflicts with the empirical evidence obtain from various measurements [39, 40, 41], and thus it remains an open question. However, its origin may not be relevant to the experiment presented in this thesis - after all, symmetry requires all of these to be present simultaneously.

Since the nematic phase follows the magnetic phase closely, it is fair to conclude that the interplay between nematic and superconductivity can be similar to the magnetic-superconductivity ones; however, the mechanism of this interplay is far from clear. From a theoretical perspective, several lines of reasoning suggest that nematic fluctuations can provide a pairing interaction [42, 43, 44], and hence suggest that the presence of nematic order in the phase diagrams of these high-temperature superconductors may not be coincidental. In particular, nematic fluctuations enhance superconductivity in any symmetry channel [45], and hence could be a key element for increasing the critical temperature even when the dominant pairing interaction arises from spin fluctuations. The observation that the point in the phase diagram at which the nematic transition temperature approaches zero often closely coincides with optimal doping (where the superconducting critical temperature ( $T_C$ ) is maximum) is possibly consistent with such a scenario [46, 2, 47]. The cause of this apparent correlation is, however, far from firmly established, and electronic nematicity may yet prove to be nothing more than an epi-phenomenon. A key open question is whether *quantum critical* nematic fluctuations are present, and if so over how much of the phase diagram.

### 1.2.4 Quantum criticality

Evidence for quantum criticality are observed in a clean system, such as the isovalently-substituted  $\text{BaFe}_2(\text{As}_{1-x}\text{P}_x)_2$ , where quantum oscillation can be observed. Quasiparticle mass enhancement close to the optimally doped composition can be seen from a de Haas van Alphen (dHvA) measurement. This is consistent with the quasiparticle mass enhancement seen in the measurement of the Sommerfeld coefficient via the heat capacity jump of the superconducting transition [48]. The linear temperature dependence of resistivity is observed close to the optimal doping, but the  $T^2$

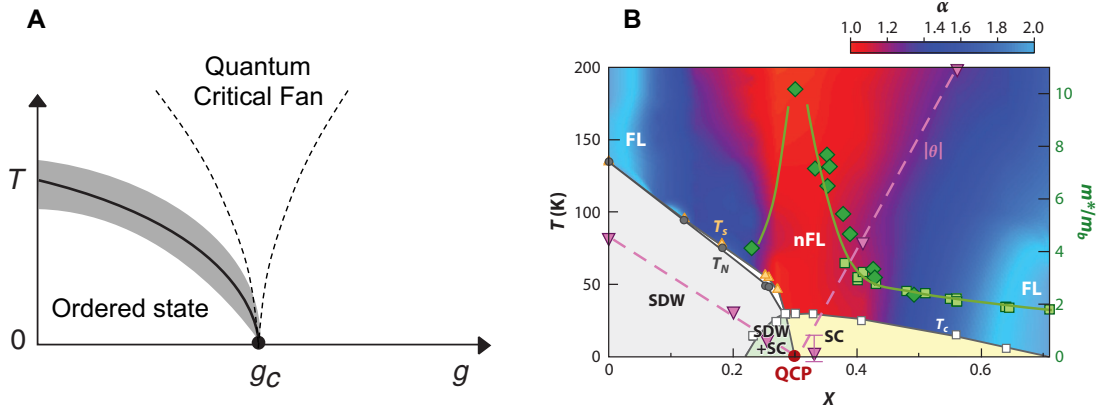


Figure 1.4: (A) A generic quantum critical phase diagram. At the parent state, system undergoes a phase transition to an ordered state at temperature  $T$ . This phase can be suppressed by applying a tuning parameter  $g$ . Quantum phase transition happens at  $g_c$  where the phase transition occurs at zero temperature. If this is a continuous phase transition, this point is called a quantum critical point. The effect of quantum critical point can be seen at higher temperature in the *quantum critical fan*, where the physical properties is dominated by the thermal excitation of quantum critical ground state. Dash lines denote the cross-over between classical and quantum critical region. (B) Signature of quantum criticality in  $\text{BaFe}_2(\text{As}_{1-x}\text{P}_x)_2$  presented in its phase diagram, where  $x$  denotes phosphorus concentration. Color scale represents  $\alpha$  from the relation  $\rho = \rho_0 + AT^\alpha$ . Blue color ( $\alpha \sim 2$ ) and red color ( $\alpha \sim 1$ ) represent non-Fermi and Fermi liquid regimes, respectively. The light green squares and dark green diamonds represent the effective mass normalized by the band mass  $m^*/m_b$  measured by the de Haas van Alphen and specific-heat measurement, respectively. Reproduced from [2] with the permission of the Annual Review of Condensed Matter Physics.

dependence, a signature of Fermi-liquid, is observed at low temperature away from the optimally doped compound. The morphology of this observation resembles a quantum critical phase diagram, where a quantum critical *fan* - the region in which quantum critical fluctuations dominate - extends wider at higher temperature with a non-critical behavior found at lower temperature away from the critical point, as illustrated in Fig.1.4 and [49]. Furthermore, the quasiparticle mass extracted from coefficient  $A$  in of the quadratic temperature dependence of the resistivity,  $\rho = \rho_0 + AT^2$ , is almost identical to that observed in the superconducting heat capacity jump and the dHvA measurements. This comes directly from the Kadowaki-Woods ratio,  $A/\gamma^2 = \text{constant}$ , where  $\gamma$  is the Sommerfeld coefficient. These evidences are compelling; however, they are observed only in the phosphorus-substituted system. They also do not reveal the nature of quantum criticality, i.e. whether the quantum critical point belongs to the magnetic quantum phase transition or the nematic quantum phase transition.

A piece of evidence found in systems across the Fe-based superconductor family is the measurement of nematic susceptibility via elastoresistivity measurement (see Section 1.3.3 for details). Large, diverging nematic susceptibility is observed at the optimally doped composition for several pnictides, and chalcogenides system [47]. This implies via the fluctuation-dissipation theorem that the nematic fluctuations are strong close to the putative nematic quantum critical point. Nematic susceptibility obtained via other method, such as elastic constant measurements [32], Raman scattering [33, 34, 35], and nuclear magnetic resonance [50], also confirms this observation.

An essential missing piece of evidence is the observation of power-law behavior of a thermodynamic quantity as a function of the non-thermal tuning parameters upon approaching the putative quantum critical point, which is a signature for a quantum criticality. In this thesis, I will show how strain can be used to uncover this elusive evidence, and establish the phenomenology of nematic quantum criticality in the representative family of cobalt-substituted  $\text{BaFe}_2\text{As}_2$ .

### 1.3 Effect of strain on nematic order

Throughout this thesis, we will be exploring the effect of strain of differing symmetry on the nematic order, as well as proposing a new conjugate field to the nematic order parameter later in Chapter 5. Before discussing the experiments in any detail, it is necessary first to introduce the representation theory in the context of  $D_{4h}$  point group appropriate for the material studied in this thesis. Then, using this language of irreducible representations, I will discuss the effect of strain on the critical temperatures of the nematic phase transition, the transport properties, and the thermodynamic properties of the material.

### 1.3.1 Representation theory for strain in $D_{4h}$ point group

Continuous phase transitions are characterized by their broken symmetry. In solids, this symmetry refers to discrete symmetry possessed by the atomic arrangements in the crystals. Since there are interactions between the electrons and the lattice, the electronic degrees of freedom must obey the symmetry of the lattice and vice versa. In the broken symmetry phase, usually at a temperature below the phase transition, the symmetry group of the crystal will reduce into a subgroup of the ones preceding it. This motivates us to use the language of group theory and representation theory to describe the interaction between the order parameter and the external influences. I will be focusing only on the broken symmetry of the  $D_{4h}$  point group, possessed by the material  $\text{Ba}(\text{Fe}_{1-x}\text{Co}_x)_2\text{As}_2$ . For readers who are interested in a more in-depth group theory, I refer to the following reference [51]. The objective of this section is not to introduce the notion of group theory from the first principle but rather to introduce the nomenclature used in this thesis and explain why certain coordinates are more intuitive to use than others.

	E	$2C_4$	$C_2$	$2C'_2$	$2C''_2$	i	$2S_4$	$\sigma_h$	$2\sigma_v$	$2\sigma_d$	Linear's Rotation	Cartesian
$A_{1g}$	1	1	1	1	1	1	1	1	1	1		$x^2 + y^2, z^2$
$A_{2g}$	1	1	1	-1	-1	1	1	1	-1	-1	$R_z$	
$B_{1g}$	1	-1	1	1	-1	1	-1	1	1	-1		$x^2 - y^2$
$B_{2g}$	1	-1	1	-1	1	1	-1	1	-1	1		$xy$
$E_g$	2	0	-2	0	0	2	0	-2	0	0	$(R_x, R_y)$	$(xz, yz)$
$A_{1u}$	1	1	1	1	1	-1	-1	-1	-1	-1		
$A_{2u}$	1	1	1	-1	-1	-1	-1	-1	1	1	$z$	
$B_{1u}$	1	-1	1	1	-1	-1	1	-1	-1	1		
$B_{2u}$	1	-1	1	-1	1	-1	1	-1	1	-1		
$E_u$	2	0	-2	0	0	-2	0	2	0	0	$(x, y)$	

Table 1.1: Character table for the  $D_{4h}$  crystallographic point group. The list of symmetry elements are shown on the top row, and the irreducible representations are shown on the left column. Reproduced from [51].

The  $D_{4h}$  point group can be constructed using 3 *generators*: a  $C_4$  rotational symmetry, a horizontal mirror plane ( $z = 0$ ), and inversion symmetry. These generators are the main symmetry elements of the point group, from which all symmetry elements can be constructed. By combining these 3 generators, 16 elements in this symmetry group are generated. *ChemTube3D* provides an excellent 3d simulation that illustrates all the symmetry elements of the  $D_{4h}$  point group [52]. These elements can be grouped into 10 classes, and therefore, according to a theorem [51], the number of *irreducible representations* will be 10 as well. The *character table* (Table 1.1) summarizes the symmetry elements and their irreducible representations. The list of symmetry elements are shown on the top row, and the irreducible representations are shown on the left column. The numbers inside the table are *characters*, which is defined as the traces of the matrices that represent the elements

in the group. For the one dimensional representations (the A's and B's in character), the characters are the representations. The two dimensional representations (E) can be constructed from the trace, and some knowledge of the symmetry.

The *Mulliken symbols* listed on the top indicates the dimensionality of the irreducible representations, and the symmetry that they break. These are the meaning of the symbol:

1. The uppercase Roman character indicates the dimensionality of the representation: A and B indicate 1 dimension, E indicates 2 dimensions, and T indicates 3 dimensions (only relevant to cubic point groups)
  - 1.1 Specifically for 1-dimensional representations, A label indicates symmetric with respect to the principle symmetry component ( $C_4$  rotation for  $D_{4h}$  point group), and B label indicates antisymmetric with respect to the principle symmetry component.
2. The next numeral subscript indicates whether the representation breaks the secondary symmetry element ( $C_2'$  in this case). 1 is symmetric and 2 is antisymmetric with respect to this symmetry operation.
3. The second subscript is in lowercase roman character. It can be either *g* (gerade), indicating symmetric with respect to inversion, or *u* (ungerade), indicating antisymmetric with respect to inversion

The concept of symmetry breaking and irreducible representation may be confusing at first but will become apparent when I introduce the concept of symmetry coordinates.

### Symmetry coordinates

A difficult aspect in constructing a theory is to obtain the right coupling terms within the symmetry constraints. Working in symmetry coordinate, rather than cartesian coordinate, will be much more intuitive since it is the coordinate that belongs to each specific symmetry group. An important feature of the symmetry coordinates is that they transform in a simple way under symmetry transformations. A symmetry coordinates will belong to an irreducible representation, and it will transform according to that irreducible representation. For example, referring to the character table, a  $B_{1g}$  quantity will be antisymmetric (a factor of -1) under  $C_4$  rotational symmetry. Obtaining these symmetry coordinates is no easy task. A standard method is called the *projection operator* method. For interested readers, please refer to [51].

Below is the list of symmetry coordinates of strain (or more generally, a second rank tensor) in

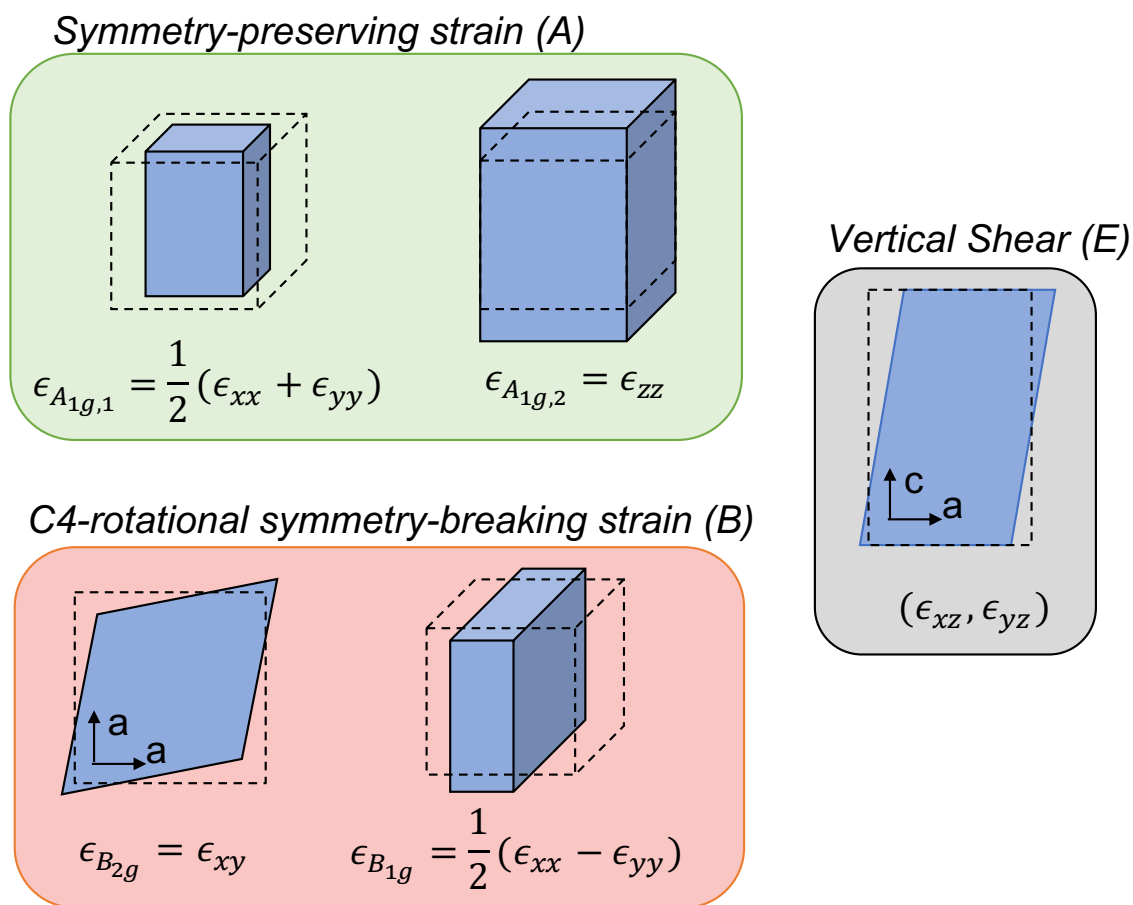


Figure 1.5: Symmetry coordinates of strain in  $D_{4h}$  point group is summarized in this figure. These strains belongs to different irreducible representation. Two types of strain belong to  $A_{1g}$  irreducible representation, which preserves symmetry when deform: in plane  $A_{1g,1}$  and out of plane  $A_{1g,2}$ . Two types of strain belong to B irreducible representation, which breaks  $C_4$  rotational symmetry. These are the  $B_{1g}$  which break diagonal mirror planes ( $x = y$  and  $x = -y$ ), and  $B_{2g}$  which breaks horizontal mirror planes ( $x = 0$  and  $y = 0$ ). The vertical shears belongs to the two dimensional  $E_g$  irreducible representation.

the  $D_{4h}$  point group:

$$\begin{aligned}
\epsilon_{A_{1g},1} &= \frac{1}{2}(\epsilon_{xx} + \epsilon_{yy}) \\
\epsilon_{A_{1g},2} &= \epsilon_{zz} \\
\epsilon_{B_{1g}} &= \frac{1}{2}(\epsilon_{xx} - \epsilon_{yy}) \\
\epsilon_{B_{2g}} &= \epsilon_{xy} \\
\epsilon_{E_g} &= (\epsilon_{xz}, \epsilon_{yz}).
\end{aligned} \tag{1.1}$$

These strains are illustrated in Fig.1.5. The first two strains belong to the  $A_{1g}$  irreducible representation, and since this strain does not break any symmetry, we call it the *symmetry-preserving strain*, or the *symmetric strain*. Note that any linear combination of the  $\epsilon_{A_{1g},1}$  and  $\epsilon_{A_{1g},2}$  belongs to  $A_{1g}$  irreducible representation. The next two strains are labeled by B symbols, meaning they break  $C_4$  rotational symmetry. However, they break different mirror planes. The  $B_{2g}$  strain breaks the vertical ( $x = 0$  and  $y = 0$ ) mirror planes, the same as the nematic order parameter  $\psi_{B_{2g}}$ . Hence we refer to it as the *conjugate strain* or, slightly more colloquially, the *longitudinal strain* since it acts as an effective longitudinal field for the order parameter by virtue of the bilinear coupling. The  $B_{1g}$  strain breaks diagonal mirror planes ( $x + y = 0$  and  $x - y = 0$ ), orthogonal to the nematic order parameter. It is hence dubbed the *orthogonal antisymmetric strain* or the *transverse strain* since it acts as an effective transverse field for the  $B_{2g}$  symmetry nematic order [53]. The  $E_g$  strains are vertical shear that belongs to the two-dimensional irreducible representation  $E_g$ . In our experiment, we control our set up such that there is no shear strain present. Therefore, I shall omit the discussion of this type of strain.

	$A_{1g}$	$A_{2g}$	$B_{1g}$	$B_{2g}$	$E_g$	$A_{1u}$	$A_{2u}$	$B_{1u}$	$B_{2u}$	$E_u$
$A_{1g}$	$A_{1g}$	$A_{2g}$	$B_{1g}$	$B_{2g}$	$E_g$	$A_{1u}$	$A_{2u}$	$B_{1u}$	$B_{2u}$	$E_u$
$A_{2g}$	$A_{2g}$	$A_{1g}$	$B_{2g}$	$B_{1g}$	$E_g$	$A_{2u}$	$A_{1u}$	$B_{2u}$	$B_{1u}$	$E_u$
$B_{1g}$	$B_{1g}$	$B_{2g}$	$A_{1g}$	$A_{2g}$	$E_g$	$B_{1u}$	$B_{2u}$	$A_{1u}$	$A_{2u}$	$E_u$
$B_{2g}$	$B_{2g}$	$B_{1g}$	$A_{2g}$	$A_{1g}$	$E_g$	$B_{2u}$	$B_{1u}$	$A_{2u}$	$A_{1u}$	$E_u$
$E_g$	$E_g$	$E_g$	$E_g$	$E_g$	$A_{1g}+A_{2g}+B_{1g}+B_{2g}$	$E_u$	$E_u$	$E_u$	$E_u$	$A_{1u}+A_{2u}+B_{1u}+B_{2u}$
$A_{1u}$	$A_{1u}$	$A_{2u}$	$B_{1u}$	$B_{2u}$	$E_u$	$A_{1g}$	$A_{2g}$	$B_{1g}$	$B_{2g}$	$E_g$
$A_{2u}$	$A_{2u}$	$A_{1u}$	$B_{2u}$	$B_{1u}$	$E_u$	$A_{2g}$	$A_{1g}$	$B_{2g}$	$B_{1g}$	$E_g$
$B_{1u}$	$B_{1u}$	$B_{2u}$	$A_{1u}$	$A_{2u}$	$E_u$	$B_{1g}$	$B_{2g}$	$A_{1g}$	$A_{2g}$	$E_g$
$B_{2u}$	$B_{2u}$	$B_{1u}$	$A_{2u}$	$A_{1u}$	$E_u$	$B_{2g}$	$B_{1g}$	$A_{2g}$	$A_{1g}$	$E_g$
$E_u$	$E_u$	$E_u$	$E_u$	$E_u$	$A_{1u}+A_{2u}+B_{1u}+B_{2u}$	$E_g$	$E_g$	$E_g$	$E_g$	$A_{1g}+A_{2g}+B_{1g}+B_{2g}$

Table 1.2: Product table for the  $D_{4h}$  crystallographic point group. Reproduced from [51].

### Product table

A product between two objects that belongs to the same or different irreducible representation will produce a new object that belongs to another irreducible representation. The product table summarizes these pair-wise products of objects of different irreducible representations. This is shown in Table 1.2 for  $D_{4h}$  point group.

This is very useful in constructing Landau free energy, as you will see throughout this thesis. The Landau free energy is an  $A_{1g}$  quantity (should not alter under any symmetry transformation), and any combination of nematic order parameter and external field has to be an  $A_{1g}$  quantity. An example is the interaction between  $\psi_{B_{2g}}$  and  $\epsilon_{B_{1g}}$ . It can be seen that the bilinear coupling term  $\psi_{B_{2g}}\epsilon_{B_{1g}}$  will produce an  $A_{2g}$  quantity according to the product table, which is not allowed in the free energy. The leading order term of this interaction is therefore  $\psi_{B_{2g}}^2\epsilon_{B_{1g}}^2$  which has an  $A_{1g}$  symmetry. Another example which you will see in Chapter 5 is that we use a combination of  $\frac{d}{dt}\epsilon_{B_{1g}}$  and magnetic field  $H_z$  to couple directly with the nematic order parameter  $\psi_{B_{2g}}$ . This is allowed because  $H_z$  is an  $A_{2g}$  quantity, and a product between  $A_{2g}$  quantity and a  $B_{1g}$  quantity will produce a  $B_{2g}$  quantity, which can then multiply with  $\psi_{B_{2g}}$  to produce an  $A_{1g}$  quantity. Note that since  $H_z$  is time-reversal odd, the time derivative of strain needed to be there to make the overall term a time-reversal even.

### 1.3.2 Effect of strain on $T_S$

In order to understand the effect of each strain irreducible representation on a given order parameter, one need to consider the allowed coupling terms in Landau free energy. For  $B_{2g}$  nematic order,  $\psi_{B_{2g}}$ , the Landau free energy can generally be written as

$$\Delta F = \frac{1}{2}a_0(T - T_S)\psi_{B_{2g}}^2 + \frac{1}{4}b\psi_{B_{2g}}^4 + f(\psi_{B_{2g}}, \epsilon), \quad (1.2)$$

where  $f$  is the coupling term between the order parameter and the strain. Since the free energy is an  $A_{1g}$  quantity, the interaction term also needs to be an  $A_{1g}$  quantity. This is because when a symmetry operation is performed on the material, it should not alter the free energy. Therefore, arbitrary combinations between  $\psi_{B_{2g}}$  and  $\epsilon$  are not allowed; rather, the combination must result in an  $A_{1g}$  quantity.

For  $A_{1g}$  strain (both  $A_{1g,1}$  and  $A_{1g,2}$ ), the coupling can be in the form  $f \sim \psi_{B_{2g}}^2\epsilon_{A_{1g}} + \psi_{B_{2g}}^2\epsilon_{A_{1g}}^2 + \dots$ . It can be seen that  $\psi_{B_{2g}}^2$  is an  $A_{1g}$  quantity, and therefore this coupling term is allowed. The effect of this coupling can be illuminated by looking at the free energy:

$$\begin{aligned} \Delta F &= \frac{1}{2}a_0(T - T_S)\psi_{B_{2g}}^2 + \frac{1}{4}b\psi_{B_{2g}}^4 + \lambda_1\psi_{B_{2g}}^2\epsilon_{A_{1g}} + \lambda_2\psi_{B_{2g}}^2\epsilon_{A_{1g}}^2 \\ &= \frac{1}{2}a_0 \left( T - \left( T_S - \frac{2\lambda_1}{a_0}\epsilon_{A_{1g}} - \frac{2\lambda_2}{a_0}\epsilon_{A_{1g}}^2 \right) \right) \psi_{B_{2g}}^2 + \frac{1}{4}b\psi_{B_{2g}}^4 \end{aligned} \quad (1.3)$$

Strain irreducible representation	Allowed interaction term	Effect to critical temperature $T_S$
$\epsilon_{A_{1g},1}, \epsilon_{A_{1g},2}$	$\psi_{B_{2g}}^2 \epsilon_{A_{1g}} + \psi_{B_{2g}}^2 \epsilon_{A_{1g}}^2 + \dots$	$T_S \sim \epsilon_{A_{1g}} + \epsilon_{A_{1g}}^2$
$\epsilon_{B_{1g}}$	$\psi_{B_{2g}}^2 \epsilon_{B_{1g}}^2$	$T_S \sim +\epsilon_{B_{1g}}^2$
$\epsilon_{B_{2g}}$	$\psi_{B_{2g}} \epsilon_{B_{2g}}$	Smears the phase transition

Table 1.3: Effect of strains of each irreducible representation on the nematic phase transition. The first column shows strains of each irreducible representation. The second column lists the corresponding allowed interaction terms to leading orders. Note that these terms must be symmetry preserving, i.e.  $A_{1g}$  quantities. The third column lists the effect of strains of each symmetry on the nematic phase transition. Note that the order parameter can be induced by  $B_{2g}$  strain, and hence there will be no true thermodynamic phase transition in the presence of  $B_{2g}$  strain. In practice, this strain would smear the signature of the phase transition, turning a sharp feature into a crossover.

This means the effect of  $A_{1g}$  strain is to shift the phase transition in linear fashion to leading order:  $T_S \sim \epsilon_{A_{1g}} + O(\epsilon_{A_{1g}}^2)$ .

The same analysis can be done with  $B_{1g}$  strain. However, here the first allowed coupling term is  $f \sim \psi_{B_{2g}}^2 \epsilon_{B_{1g}}^2$  since any lower-order term will not be  $A_{1g}$  object, and higher-order terms can only involve even order of  $\epsilon_{B_{1g}}$ . This means that  $T_S$  can only vary quadratically to leading order with  $B_{1g}$  strain:  $T_S \sim \epsilon_{B_{1g}}^2 + O(\epsilon_{B_{1g}}^4)$ .

$B_{2g}$  strain can couple bilinearly to the order parameter. Since the  $B_{2g}$  strain breaks the same symmetry as the nematic order parameter, it will induce nematic order in the disordered state, and hence there will be no true thermodynamic phase transition in the presence of  $B_{2g}$  strain. In practice, this strain would smear the signature of the phase transition, turning a sharp feature into a crossover.

The effects of these strains are summarized in Table 1.3. Note that In my experimental setup, care was taken to ensure that no  $E_g$  strains are present. Therefore, I omit the discussion of its effect.

### 1.3.3 Effect of strain on transport properties: Elastoresistivity

When a material is deformed, its resistance will change from two main mechanisms. Consider a cylindrical shape conductor  $R = \rho \frac{l}{A}$ , the fractional change of the resistance when the cylinder is deformed is:

$$\frac{\Delta R}{R} = \frac{\Delta \rho}{\rho} + \frac{\Delta l}{l} - \frac{\Delta A}{A}, \quad (1.4)$$

where  $R$ ,  $\rho$ ,  $l$ , and  $A$  are the resistance, resistivity, length, and cross section area of the cylinder, respectively. The latter two terms are the *geometric factor*. The first term is the change in the intrinsic property of the material and is the quantity of interest in this section.

The change in resistivity to applied strain is

$$\Delta\rho_{ij}(\boldsymbol{\epsilon}) = \rho_{ij}(\boldsymbol{\epsilon}) - \rho_{ij}(\boldsymbol{\epsilon} = 0), \quad (1.5)$$

and the fractional change in resistivity is defined in the following way:

$$\left(\frac{\Delta\rho}{\rho}\right)_{ij} = \frac{\Delta\rho_{ij}(\boldsymbol{\epsilon})}{\sqrt{\rho_{ii}(\boldsymbol{\epsilon} = 0)}\sqrt{\rho_{jj}(\boldsymbol{\epsilon} = 0)}}. \quad (1.6)$$

Note that the repeated indices  $ii$  and  $jj$  do not indicate summation. This definition may look unintuitive at first, but simply defining  $\left(\frac{\Delta\rho}{\rho}\right)_{ij} = \frac{\Delta\rho_{ij}}{\rho_{ij}}$  does not work, since  $\left(\frac{\Delta\rho}{\rho}\right)_{xy}$  automatically goes to infinity in an absence of magnetic field, as  $\rho_{xy}(\boldsymbol{\epsilon} = 0) = 0$ . The reasoning for this definition can be found in [54].

The elastoresistivity tensor ( $m$ ) is a fourth rank tensor that relates the  $ij$  elastoresistivity component to the  $kl$  strain component. It is defined in the following equation

$$\left(\frac{\Delta\rho}{\rho}\right)_{ij} = \sum_{kl} m_{ijkl}\epsilon_{kl}. \quad (1.7)$$

All the above definition is in cartesian coordinate, which is unintuitive to work with. We then extend the concept of symmetry coordinates introduced above to the definition of the fractional change of the resistivity as well. For the  $D_{4h}$  point group, the fractional change of the resistivity expressed in the symmetry coordinates are

$$\begin{aligned} \left(\frac{\Delta\rho}{\rho}\right)_{A_{1g,1}} &= \frac{1}{2} \left( \left(\frac{\Delta\rho}{\rho}\right)_{xx} + \left(\frac{\Delta\rho}{\rho}\right)_{yy} \right) \\ \left(\frac{\Delta\rho}{\rho}\right)_{A_{1g,2}} &= \left(\frac{\Delta\rho}{\rho}\right)_{zz} \\ \left(\frac{\Delta\rho}{\rho}\right)_{B_{1g}} &= \frac{1}{2} \left( \left(\frac{\Delta\rho}{\rho}\right)_{xx} - \left(\frac{\Delta\rho}{\rho}\right)_{yy} \right) \\ \left(\frac{\Delta\rho}{\rho}\right)_{B_{2g}} &= \left(\frac{\Delta\rho}{\rho}\right)_{xy} \\ \left(\frac{\Delta\rho}{\rho}\right)_{E_g} &= \left( \left(\frac{\Delta\rho}{\rho}\right)_{xz}, \left(\frac{\Delta\rho}{\rho}\right)_{yz} \right). \end{aligned} \quad (1.8)$$

The elasto-resistivity relation can be written in the symmetry coordinates as

$$\left(\frac{\Delta\rho}{\rho}\right)_{\alpha} = \sum_{\alpha'} m_{\alpha\alpha'}\epsilon_{\alpha'}, \quad (1.9)$$

where  $\alpha, \alpha' = A_{1g,1}, A_{1g,2}, B_{1g}, \dots$

The relation above seems to be as complex as the cartesian one. However, let's consider the coefficient  $m_{\alpha\beta}$ . This quantity relates strain of symmetry  $\beta$  to the fractional change of resistivity of symmetry  $\alpha$  through the relation  $\left(\frac{\Delta\rho}{\rho}\right)_\alpha = m_{\alpha\beta}\epsilon_\beta$ . Since  $m_{\alpha\beta}$  is a physical property of the material, it should not change under symmetry transformation. The implication here is that  $m_{\alpha\beta}$  is non-zero only when  $\alpha = \beta$ . This is because for  $\alpha \neq \beta$ , there exist a transformation R that transform  $\left(\frac{\Delta\rho}{\rho}\right)_\alpha$  and  $\epsilon_\beta$  differently, making the relation self contradictory.

The relation 1.9 then reduced to

$$\left(\frac{\Delta\rho}{\rho}\right)_\alpha = m_{\alpha\alpha}\epsilon_\alpha. \quad (1.10)$$

It should also be noted that the fractional change in resistivity and strain of different symmetry can be related to a higher-order expansion, for example  $\left(\frac{\Delta\rho}{\rho}\right)_\alpha = \sum_{\beta\gamma} m_{\alpha,\beta\gamma}\epsilon_\beta\epsilon_\gamma$ , as long as  $\epsilon_\beta\epsilon_\gamma$  has the same symmetry as  $\left(\frac{\Delta\rho}{\rho}\right)_\alpha$ . The full discussion of elastoresistivity tensor under symmetry constraints can be found in references [55, 54].

To measure the elastoresistivity coefficient  $m_{\alpha\alpha}$ , simply dividing  $\left(\frac{\Delta\rho}{\rho}\right)_\alpha$  by  $\epsilon_\alpha$  does not work. This is because  $\left(\frac{\Delta\rho}{\rho}\right)_\alpha$  can depend on higher order polynomial of  $\epsilon_\alpha$ . There is also an experimental concern - a small uncertainty in  $\epsilon_\alpha$  can cause large uncertainty in  $\left(\frac{\Delta\rho}{\rho}\right)_\alpha$ , especially if the measurement has to be done in the small  $\epsilon_\alpha$  region. An accurate way to define and measure the elastoresistivity coefficient is using the following relation:

$$m_{\alpha\alpha} = \frac{d}{d\epsilon_\alpha} \left(\frac{\Delta\rho}{\rho}\right)_\alpha \Big|_{\epsilon=0}. \quad (1.11)$$

This can be achieved by measuring the slope of  $\left(\frac{\Delta\rho}{\rho}\right)_\alpha$  vs  $\epsilon_\alpha$  in the linear regime. In Section 2.4, I will discuss how this is done using oscillating strain.

It is difficult to calculate the elastoresistivity away from the phase transition since one would need to consider all the microscopic details of the system. However, close to the phase transition, Landau theory provides a good phenomenological model that allows us to predict the behavior at this region without having microscopic insights. Next, I will discuss elastoresistivity caused by  $B_{2g}$ ,  $A_{1g}$ , and  $B_{1g}$  strain.

### Elastoresistivity caused by $B_{2g}$ strain

As the temperature is reduced below the nematic phase transition, anisotropy in both electronic and lattice degrees of freedom will appear due to the breaking of the  $C_4$  rotational symmetry. This anisotropy will also manifest in the resistivity of the material (also any other tensor properties of the material). However, since there is a coupling between the lattice and the electronic degrees of freedom, the anisotropy can be induced by applying strain of the same symmetry. This is the origin

of the  $B_{2g}$  elasto-resistivity. In a small anisotropy limit, it is assumed that this anisotropy will be directly proportional to the order parameter, i.e.

$$\left(\frac{\Delta\rho}{\rho}\right)_{B_{2g}} \propto \psi_{B_{2g}} = g_{T,x}\psi_{B_{2g}}, \quad (1.12)$$

where  $g_{T,x}$  is a proportionality constant that in principle can be both temperature dependent and doping dependent. Previous measurements have revealed that the temperature dependence is small [17], but the doping dependence can potentially be significant [56].

To calculate  $\psi_{B_{2g}}$ , consider the free energy in the presence of  $B_{2g}$  strain:

$$\Delta F = \frac{1}{2}a_0(T - T^*)\psi_{B_{2g}}^2 + \frac{1}{4}b\psi_{B_{2g}}^4 + \lambda\psi_{B_{2g}}\epsilon_{B_{2g}}, \quad (1.13)$$

where  $\lambda$  is the nematic-elastic coupling. Minimizing this free energy with respect to the order parameter and assume the quartic term is small in the disorder state, one obtains

$$\psi_{B_{2g}} = \frac{\lambda\epsilon_{B_{2g}}}{a_0(T - T^*)} = \lambda\chi_{B_{2g}}\epsilon_{B_{2g}}. \quad (1.14)$$

Substituting this into Eq. 1.12, the elasto-resistivity caused by  $B_{2g}$  strain is

$$\left(\frac{\Delta\rho}{\rho}\right)_{B_{2g}} = g_{T,x}\psi_{B_{2g}} = \frac{g_{T,x}\lambda\epsilon_{B_{2g}}}{a_0(T - T^*)} = g_{T,x}\lambda\chi_{B_{2g}}\epsilon_{B_{2g}}, \quad (1.15)$$

where  $\chi_{B_{2g}} = 1/a_0(T - T^*)$  is the nematic susceptibility. Comparing this to the relation in Eq. 1.10, one can relate the elasto-resistivity coefficient to the nematic susceptibility as

$$m_{B_{2g},B_{2g}} = g_{T,x}\lambda\chi_{B_{2g}} \propto \chi_{B_{2g}}. \quad (1.16)$$

Our group has developed techniques to measure the elasto-resistivity coefficient, most notably the amplitude demodulation method [57] with either the modified Montgomery geometry [47, 58], or the transverse resistivity configuration [54, 59]. With the geometry of our experiment setup, the transverse resistivity is the most appropriate method. The details will be described in Section 2.4.

### Elastoresistivity caused by $A_{1g}$ and $B_{1g}$ strain

The Landau treatment of  $A_{1g}$  and  $B_{1g}$  strain has been shown in Section 1.3.2, and it is concluded that  $A_{1g}$  and  $B_{1g}$  strain only renormalize the critical temperature  $T_S$  of the  $B_{2g}$  nematic phase transition. It is possible that there may be a  $B_{1g}$  nematic component, in which case, a treatment similar to  $B_{2g}$  elasto-resistivity is required. However it is found that the elasto-resistivity coefficient  $m_{B_{1g},B_{1g}}$ , a quantity that is directly proportional to the  $B_{1g}$  nematic susceptibility  $\chi_{B_{1g}}$ , is very small [17]. This suggests that  $B_{1g}$  strain does not induce noticeable anisotropy to the system.

Close enough to the phase transition, one can express the critical temperature as a function of reduced temperature:  $\rho_{ij} = \rho_{ij}(T - T_S(\epsilon_{A_{1g}}, \epsilon_{B_{1g}}))$ . The elastoresistivity can be calculated by taking a derivative of the resistivity with respect to strain and applying the chain rule:

$$\frac{\partial \rho_{ij}}{\partial \epsilon_{A_{1g}}} = \frac{\partial \rho_{ij}}{\partial T_S} \frac{\partial T_S}{\partial \epsilon_{A_{1g}}}. \quad (1.17)$$

Using the relationship  $\frac{\partial \rho}{\partial T_S} = -\frac{\partial \rho}{\partial T}$  (this comes directly from  $\rho_{ij} = \rho_{ij}(T - T_S(\epsilon_{A_{1g}}, \epsilon_{B_{1g}}))$ ), one finds that

$$\frac{\partial \rho_{ij}}{\partial \epsilon_{A_{1g}}} = -\frac{\partial \rho_{ij}}{\partial T} \frac{\partial T_S}{\partial \epsilon_{A_{1g}}}. \quad (1.18)$$

The same treatment can be done for the  $B_{1g}$  strain. The implication here is that the  $A_{1g}$  and  $B_{1g}$  elastoresistivity will be directly proportional to the temperature derivative of the resistivity. This result will be very useful in determining the critical temperature  $T_S$  via Fisher-Langer relation between  $\partial \rho / \partial T$  and  $C_p$  [60], which will be discussed in Section 2.3.2.

### 1.3.4 Effect of strain on thermodynamics properties: Elastocaloric effect

Strain can also affect the thermodynamic properties of a material. This is due to the change of entropy when the material is deformed. This is precisely the definition of the elastocaloric effect: the change of entropy in response to strain. Under isothermal conditions, the elastocaloric coefficient can be defined as  $\eta_{ij} = \left( \frac{\partial S}{\partial \epsilon_{ij}} \right)_{T, \tilde{\epsilon}}$  in cartesian coordinate, or  $\eta_\alpha = \left( \frac{\partial S}{\partial \epsilon_\alpha} \right)_{T, \tilde{\epsilon}}$  in the symmetry coordinates, where  $\alpha$  labels the different irreducible representations of the point group, and  $\tilde{\epsilon}$  denote other strain components. In this section, I will discuss the elastocaloric effect that comes from  $A_{1g}$  and  $B_{1g}$  strain. The  $B_{2g}$  elastocaloric effect is also very interesting in its own right, but since it is not relevant to this thesis work, I refer the reader to the following reference for more detail [56].

#### Elastocaloric effect caused by $A_{1g}$ and $B_{1g}$ strain

The primary mechanism by which  $A_{1g}$  and  $B_{1g}$  strains change the entropy landscape is by shifting the critical temperature. Presumably smaller, more subtle effects arise from strain-induced changes to the phonon spectrum, but sufficiently close to the critical temperature, these effects are dominated by the critical behavior, which is our focus. Suppose the critical temperature is a function of strain,  $T_S(\epsilon)$ , where  $\epsilon$  is a short hand for  $\epsilon_{A_{1g}}$  or  $\epsilon_{B_{1g}}$ . From Landau theory, thermodynamic quantities close to the phase transition can be written as a function of the ‘distance’ from  $T_S$ . The critical part of the entropy and the heat capacity is then  $S^{\text{crit}} = S^{\text{crit}}(T - T_S(\epsilon))$  and  $C^{\text{crit}} = C^{\text{crit}}(T - T_S(\epsilon))$

respectively. Here the elastocaloric coefficient is then

$$\begin{aligned} \frac{\partial S}{\partial \epsilon} &= \frac{\partial S^{\text{crit}}}{\partial T_S} \frac{dT_S}{d\epsilon} \\ &= -\frac{\partial S^{\text{crit}}}{\partial T} \frac{dT_S}{d\epsilon} = -\frac{C^{\text{crit}}}{T} \frac{dT_S}{d\epsilon}. \end{aligned} \quad (1.19)$$

Note here that since the non-critical part of the entropy varies very little with strain, to a high degree of accuracy  $\frac{\partial S}{\partial \epsilon} \simeq \frac{\partial S^{\text{crit}}}{\partial \epsilon}$ . A direct consequence of this is that the  $A_{1g}$  and  $B_{1g}$  elastocaloric effect are direct measures for the critical part of the heat capacity. This means it can be used as a direct probe for the critical part of the heat capacity.

The method used to measure the elastocaloric effect is the AC elastocaloric effect developed in our group [61]. The signal-to-noise ratio of this method is noticeably higher than the relaxation time method, because it measures the critical part of the heat capacity without having to subtract the phononic background. In addition, as this is an AC technique, the signal can be detected using the lock-in amplifying technique. It is also less time consuming than the usual relaxation time method - one data point would take time in the order of a second compared to a minute for relaxation time method. The measurement can also be done in a quasi-static fashion - there is no need to stabilize the temperature between the data points.

In order to measure this effect, a favorable thermodynamic condition must be met. This effect cannot be observed in an isothermal condition since any heat generated by the elastocaloric effect is dissipated to the thermal reservoir. However, in an adiabatic condition, where the total entropy is constant, the temperature of the material must change to compensate for the entropy generated by the elastocaloric effect. The elastocaloric effect can then be measured in this scenario.

Under an adiabatic condition, the change of entropy has to be zero,  $dS = 0$ . The entropy change can be expressed in terms of partial derivatives of temperature and strain:

$$dS(T, \epsilon) = \left( \frac{\partial S}{\partial T} \right)_{\epsilon} dT + \left( \frac{\partial S}{\partial \epsilon} \right)_T d\epsilon, \quad (1.20)$$

The first term  $\partial S/\partial T$  is the total heat capacity of the sample,  $C/T$ . Substitute the result from Eq. 1.19, and equate this to zero, one arrives at the relation

$$dT = \frac{C^{\text{crit}}}{C} \frac{dT_S}{d\epsilon} d\epsilon. \quad (1.21)$$

Therefore, in an adiabatic condition, the critical part of the specific heat can be probed by measuring the temperature change of the sample induced by the applied  $A_{1g}$  and  $B_{1g}$  strains. This temperature change is usually very small and in the milli-Kelvin range. I will discuss the experimental method to measure this temperature change in the next chapter in Section 2.3.3

## 1.4 Thesis layout

In the next chapter, I present the experimental methods used in this thesis. The experimental process starts from material synthesis and preparation for measurement, including crystal growth, cutting, cleaving, and patterning microstructure (which is relevant in Chapter 5). The samples are then ready for measurements under hydrostatic pressure and uniaxial stress measurements. The technique that we used to determine the critical temperature of the nematic phase transition is explained. Finally, relevant to the experiment in Chapter 5, elastoresitivity formalism is introduced.

The central theme of this thesis is to use symmetry-breaking strain to tune the critical temperature of the nematic phase transition and hence probe nematic quantum criticality. These experiments are presented in Chapter 3 and Chapter 4. First, I established symmetry-breaking strain as an effective tuning parameter in Chapter 3. By comparing the effect of hydrostatic pressure and uniaxial stress on the critical temperature  $T_S$ , the effect of each irreducible representation of strain can be distinguished. This also presents a new perspective in which a stress-based tuning parameter such as hydrostatic pressure can be dissected further into strain of differing symmetries, providing further insights into microscopic physics. The experiment is done for the prototypical iron-based superconductor,  $\text{Ba}(\text{Fe}_{0.975}\text{Co}_{0.025})_2\text{As}_2$ . The technique established in Chapter 3 is then used to systematically study the strain-tuning effect of nematic order in the cobalt-doped series of  $\text{BaFe}_2\text{As}_2$  in Chapter 4. It is found that symmetry breaking strain becomes more effective at tuning nematic order close to the optimally doped composition. This turns out to be a direct consequence of quantum criticality, as a power-law behavior of  $T_S$  is observed as a function of strain, providing direct evidence for nematic quantum criticality. This power-law behavior extends through a wide region of the phase diagram and approximately correlates to where the material superconducts - indicating a possible 'interplay between superconductivity and nematic quantum criticality.

These perspectives open up many possibilities to use strain to probe nematic quantum criticality. One, in particular, is to measure physical properties while tuning the material towards/away from the quantum critical point with strain. I demonstrated this in Chapter 5, where I attempted to measure a nematic susceptibility while tuning with strain. This method is enabled by a novel conjugate field which consists of  $z$ -direction magnetic field  $H_z$  and time-dependent  $B_{1g}$  strain,  $\epsilon_{B_{1g}}$ . Even though the signal associated with this coupling can be observed, it does not have the expected temperature dependence, pointing towards other microscopic origin. Although this final experiment yielded a null result, it builds a framework which can be used in other material system where the coupling could be larger, such as in other Fe-based superconductors, or in  $4f$  quadrupolar system.

## Chapter 2

# Experimental Methods

### 2.1 Material preparation for strain measurements

Cobalt-substituted  $\text{BeFe}_2\text{As}_2$  single crystals were grown from a FeAs flux following the technique which has been published and described in greater detail in papers and theses by previous students in our group [7, 62]. Crystals were extracted mechanically. They tend to grow in a plate-like shape with [001] crystallographic direction perpendicular to the plane and have facets along [100] crystallographic direction. Samples were cleaved along [001] to a thickness of  $50\mu\text{m}$  before cutting along [100], as it is more challenging to cut long [100] for a thick sample. To cleave the sample, it is advised to hold it vertically (with the sample surface perpendicular to the working surface), then slowly press a scalpel blade parallel to the plate's surface. If done correctly, the sample should break into two pieces with minimum steps on the surface. This technique should be applicable for samples thicker than  $50\mu\text{m}$ . For smaller samples, place the sample on a flat surface, lay the scalpel blade parallel to the sample's surface and slowly push the blade into the sample. To cut the sample along [100], align the scalpel along the facets of the crystal, then use the tip of the scalpel to nick at the edge of the crystal (wiggle slightly if needed), the crack should propagate along the [100] direction.

Samples prepared for the uniaxial stress experiments should be  $>1\text{mm}$  in length,  $\sim 300 - 500\mu\text{m}$  in width in width, and between  $20\mu\text{m}$  to  $40\mu\text{m}$  in thickness. We found that thinner samples mechanically fail more often, and we found a drop in strain transmitted for thicker samples. Since the strain transmission depends on the cross-section area, narrower samples can tolerate more thickness. 4-point Electrical contacts were made by affixing gold wires onto the sample surface using *Chipquik* SMD291AX10T5 solder and cured at  $200^\circ\text{C}$  until the solder hardens (this usually takes only 15 seconds). Contact resistance should be checked with a multimeter and have a value of  $\sim 1\Omega$ . This sample is then ready for mounting on a uniaxial stress cell which will be described in Section 2.2.2.

For experiments described towards the end of my thesis (Chapter 5), it becomes extremely important to have very well controlled electrical contact placement, as the signal is anticipated to be

extremely small. This necessitated preparations of crystals using Focused Ion Beam (FIB). This is a standard technique, and interested readers are pointed to other literature for a detailed description of how it works [63]. For the purpose of this thesis, it is sufficient to say that beams of high energy ions are used to mill away parts of samples, revealing a well-defined path for current flow and accurately defined voltage contacts.

Before milling in the FIB, samples were cut and cleaved into typical dimensions of  $300\mu\text{m}\times 300\mu\text{m}\times 10\mu\text{m}$ . It is crucial to have the samples no thicker than  $20\mu\text{m}$ , as this will present many problems during the milling process. Gold was sputtered on top of the sample to create a well-connected electrical contact using a *Cressington* 108 Manual Sputter Coater. The sample was then glued onto the PZT stack using *Angstrom Bond* AB9110LV epoxy. Scale bar in the microscopes can be used as an aid when aligning samples to the strain axis. Be careful to keep the sample surface clean during the whole process. The *Angstrom Bond* is fully cured by leaving at room temperature for 18 hours, or at  $65^\circ\text{C}$  for 1 hour. If the ( $65^\circ\text{C}$ ) cure option is needed, it is advised to leave the *Angstrom Bond* at room temperature for 1 hour to stiffen up before starting the ( $65^\circ\text{C}$ ) cure. This is because fresh *Angstrom Bond* has very low viscosity at ( $65^\circ\text{C}$ ). Heating the epoxy right after the application can cause it to move around due to capillary force, changing the sample orientation. After the epoxy is set, gold wires are then affixed to the sample using the *EPO-TEK* H-20E 2-part silver epoxy cured at  $120^\circ\text{C}$  for 15 minutes. During these high temperature cures (both for the *Angstrom Bond* and the H-20E), the + and - leads of the PZT stack should be shorted together to prevent voltage build up on the PZT. The sample is then ready for a FIB milling process.

After the milling process, the sample should be checked for contact resistance. Do not use a multimeter to measure the resistance directly, as the current output from the multimeter can permanently damage the microstructure. Instead, in my experiment, the current was sourced using *Stanford Research* SR860 through a  $1\text{k}\Omega$  resistor, and the voltage was measured using the same instrument. The current should be kept small ( $\sim 100\mu\text{A}$ ) during this measurement. Typical 2-point contact resistance for  $1\mu\text{m}$  thick microstructure is around  $20\Omega - 30\Omega$ , and the resistance between two voltage contact measuring with 4-point method should be  $\sim 5\Omega - 10\Omega$ . The transverse voltage due to contact misalignment should be  $< 1\%$  of the longitudinal voltage. If these numbers fall too far out of range, they should be inspected for short circuit or mechanical failures using either a high-resolution microscope or SEM inside the FIB machine. Depending on the issue found, the sample may be salvaged by milling it for the second time, or a new sample has to be prepared.

## 2.2 Application of stress to the materials

This section outlines three techniques utilized to deform the material: sample on PZT, uniaxial stress, and hydrostatic pressure. Each of these techniques has different stress characteristics and, therefore, will yield different combinations of strains. A combination of uniaxial stress and hydrostatic pressure

is the basis for the symmetry decomposition technique. The sample on PZT stack was used in Chapter 5, due to the need for microstructuring the sample.

### 2.2.1 Lead-Zirconium-Titanate (PZT) stack

Lead-zirconium-titanate (PZT) is a piezoelectric material - i.e. a material that deforms when applying voltage. It can be used to apply stress to the samples; simply gluing the sample on top of a PZT stack can transmit stress through the glue. Moreover, PZT stacks are active components inside the uniaxial stress cell that will be discussed in the next section.

#### Strain characteristic

The PZT stack used in the experiments is from *Piezomechanik GmbH* model PSt150/5×5/7 cryo 1. This type of PZT deforms in a biaxial fashion when voltage is applied. Under positive voltage, the PZT will elongate along its poling axis and contract along its transverse axis. The Poisson ratio of the PZT stack  $\nu_P$  characterizes the ratio between the strain in the x- and y-direction according to the relation  $\epsilon_{yy} = -\nu_P \epsilon_{xx}$ . This number is slightly temperature dependent, but in the temperature range of my experiment, the value is approximately temperature independent at  $\sim 2.3$  [47]. In an ideal situation, where there is no strain relaxation through the glue, the strain response of the sample should be exactly the same as the PZT, i.e.  $\epsilon_{xx}^{\text{sample}} = \epsilon_{xx}^{\text{PZT}} = \epsilon_{xx}$  and  $\epsilon_{yy}^{\text{sample}} = \epsilon_{yy}^{\text{PZT}} = \epsilon_{yy}$ , and since the sample is not fixed in the z-axis, it will deform according to its out of plane Poisson's ratio. However, since the glue is not infinitely stiff, there will be strain relaxation, and the strain response of the sample will be reduced. The strain relaxation has been characterized elsewhere [47] by fixing a strain gauge on top of a large sample. It is found that the strain response of the sample is  $\sim 80\%$  of the strain on the PZT and only has a weak temperature dependence. Since I am looking for a divergence in elastoresistivity as a function of temperature, this weak temperature dependence does not affect the conclusion of my experiment in Chapter 5 as long as there is enough strain transmitted to the sample.

Various types of glue can be used to fix the sample to the PZT, for example, *Devcon* 5-minute epoxy, *Devcon* two-tonne epoxy, and *Angstrom Bond* AB9110LV. These have been tested to deliver adequate strain transmission for temperature under 250K ( $> 80\%$ ). *Angstrom Bond* AB9110LV is my preferred choice. The *Angstrom Bond* is fully cured by leaving at room temperature for 18 hours, or at  $65^\circ\text{C}$  for 1 hour. If the ( $65^\circ\text{C}$ ) cure option is needed, it is advised to leave the *Angstrom Bond* at room temperature for 1 hour to stiffen up before starting the ( $65^\circ\text{C}$ ) cure. This is because fresh *Angstrom Bond* has very low viscosity at ( $65^\circ\text{C}$ ). Heating the epoxy right after the application can cause it to move around due to capillary force, changing the sample orientation.

### Measuring strain

Strain can be estimated by affixing a resistive strain gauge (*Vishay Precision* WK-06-062TT-350) to the back of the PZT stack. Under the assumption that the sample (affixed to the other side of the PZT stack) is sufficiently thin so as to not affect the PZT deformation, and also assuming a similar strain relaxation in the glue layer on each side of the stack, the strain experienced by the strain gauge can then be used to estimate that of the sample. This has been tested by also affixing a strain gauge to the top of the sample [47]. This strain gauge has very small elastic moduli and will experience almost 100% of the strain, making the measurement very accurate. Since this strain gauge is made of Karma alloy folded into a meander shape, it will only be sensitive to the deformation in the meander direction. The gauge factor (GF), usually provided by the manufacturer, is defined as the ratio between the fractional change of resistance  $\Delta R/R$  and strain  $\epsilon$ :

$$GF = \frac{\Delta R}{R_0} / \epsilon, \quad (2.1)$$

where  $R_0$  is the free-standing resistance value ( $\sim 350 \Omega$ ), and the gauge factor is  $\sim 2$ . The strain can therefore be inferred from this relation.

The change in resistance of the strain gauge is measured using the usual four point resistance probes with offset expand mode in *Stanford Research* SR860 Lock-In amplifier. Current is sourced by connecting the output of the lock-in amplifier in series with a  $1\text{k}\Omega$  resistor ensures a constant current through the strain gauge.

### 2.2.2 Uniaxial stress cell

The uniaxial stress experiment is carried out in a commercially available strain device ((CS100, *Razorbill Instrument*). The device is constructed using three piezoelectric stacks (PZT) based on the design by Hicks *et al.*[64] this is illustrated in figure 2.1. This design enables the full utilization of the PZT's expansions - yielding up to 1.5% tensile and compressive strain, which in our case exceeds the yield strength of the samples. Furthermore, the design compensates for the thermal expansion of the PZT stacks. The only other source of any eventual temperature dependence of strain at a fixed voltage is the difference in thermal expansion of the sample and the cell body. In this case, it is found that the thermal expansion of titanium and  $\text{Ba}(\text{Fe}_{1-x}\text{Co}_x)_2\text{As}_2$  are matched at all temperatures [65]. This means the strain response of the sample is almost perfectly independent of temperature at a fixed voltage applied to the PZT stacks.

### Mounting procedure

After several trial and error, summary of the most recent mounting procedure is presented below:

1. First, the bottom mounting plate needs to be glued onto the cell body using *Devcon* 2-part

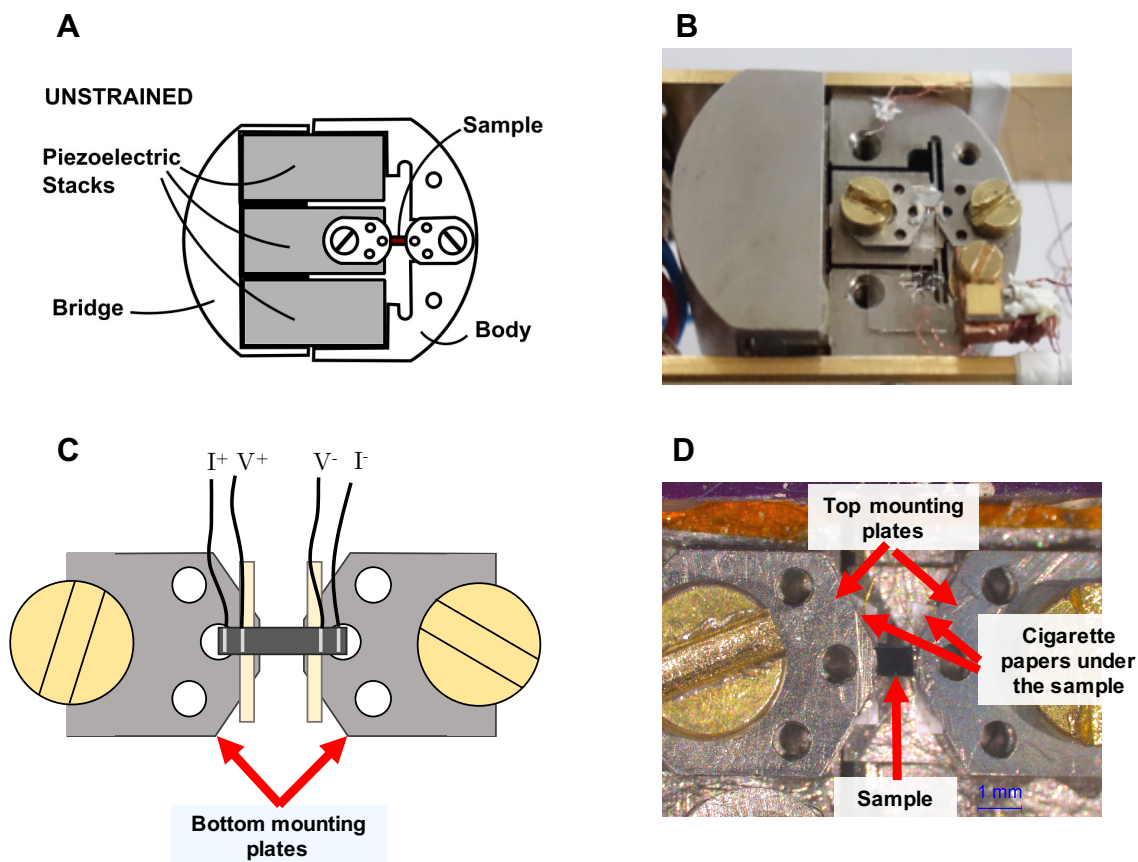


Figure 2.1: (A) The design of the *Razorbill* CS100 cell. Samples is deformed by applying voltages into the outer and the inner PZT stacks. This design compensates for thermal expansion of the PZT (the inner and outer will expand at the same rate, cancelling out each other), and also converts all the length change of the PZT into the sample. (B) Picture of a working *Razorbill* cell. A Cernox thermometer is attached and thermally anchored to the cell body. Picture taken by Matthias Ikeda. (C) Schematic showing the assembly procedure. The sample is glued on top of bottom mounting plates and is electrically separated by thin cigarette papers. (D) shows the final arrangement where the top mounting plates are glued on top of the sample and affixed to the cell by screws to provide uniform strain along the z-direction.

five-minute epoxy. This can be done by screwing the bottom mounting plates to the cell body at an appropriate position. Make sure that the plate separation is correct and the mounting plates are aligned to the strain axis. The glue can then be applied to the side of the mounting plate. The capillary force will draw in the glue.

2. Once the epoxy dries, remove the screws. (The plates should not move when removing the screws. Reapply the glue if the plates move.) Glue cigarette papers ( $\sim 30\mu\text{m}$  in thickness) or any thin insulators to the tip of the lower mounting plates using *Devcon* 2-part five minute epoxy. This step is to electrically insulate the sample and the cell body.
3. Once the epoxy dries, glue the sample onto the bottom mounting plate using 2-part five-minute epoxy. Press the end of the samples lightly with a small, thin wooden piece to ensure good contact with the mounting plate. Adjust the alignment as needed. Wait until the epoxy dries.
4. Screw the top mounting plate on top of the lower mounting plate separated by washers of fixed thickness to obtain uniform stress across the sample's cross-section. Make sure the top mounting plate is aligned with the lower mounting plate. At this stage, check for an electrical connection between the sample and the plate. If the sample and the top mounting plate are shorted together, insert small pieces of cigarette paper between the sample and the top mounting plates.
5. Gluing the sample and top mounting plate together by dropping *Devcon* two-tonne epoxy in the middle hole of the top mounting plate, until the epoxy started to come out on the side. Be careful not to have this spilled onto the sample surface. It was found that the 5-minute epoxy cannot sustain maximum strain exerted by the strain cell, so a stronger epoxy like the two-tonne is recommended.
6. It should be noted that it takes 30 minutes for two-tonne epoxy to be stable and 24 hours to harden fully. The hardening can be sped up by heating the probe at  $80^\circ\text{C}$  for 40-minute. WARNING: the PZT inside the cell must be shorted together during this curing process to prevent voltage build-up in the PZT stacks, which can permanently damage the cell.
7. (Optional) Thin layer of glue (*Angstrom Bond* AB9110LV is recommended) can be used to coat the sample to increase the strength of the sample. This is because the glue can penetrate small cracks inside the sample, preventing the cracks from propagating. This will increase the strain range significantly.

### **Applying stress**

Stress is applied to the sample by controlling voltage to the outer and inner PZT stacks of the stress cell. We use the inner PZT stack to apply only DC offset stress, while the outer stacks apply

oscillating stress on top of DC offset stress. The voltages across the outer stacks are controlled using *Stanford Research* SR860 Lock-In amplifier and amplified by a factor of 25 through a *Tegam* 2350 precision power amplifier. The inner stacks are controlled using an auxiliary output of the SR860 and amplified by a factor of 25 through a *Piezosystem Jena* SVR 350-1 bipolar voltage amplifier.

### Measuring strain

The CS100 uniaxial stress cell is equipped with a capacitance sensor for measuring the change in mounting plate separation. The capacitance is sampled using an *Andeen-Hagerling* AH2550A capacitance bridge. To calculate strain, capacitance is converted to displacement using the displacement-capacitance curve characterized by *Razorbill*. This curve relates mounting plate displacement  $d$  and change in capacitance from its zero displacement point  $C - C_0$ . The tricky aspect of this conversion is that the zero-displacement capacitance  $C_0$  is temperature dependent due to the thermal expansion of the titanium. It is also not the same in each run, e.g.  $C_0(300\text{ K})$  change from run to run. This effect comes from a few factors. The PZT has hysteresis, and the zero-displacement capacitance will depend on where the PZT is in the hysteresis loop. Also, when the sample is attached to the cell, a small amount of strain can be imposed on the cell body due to glue hardening, which can alter the capacitance slightly. In order to account for this effect, first, the zero displacement capacitance is normalized by its value at 300K  $C/C(300\text{K})$ . Then this quantity is fitted as a function of temperature to a 4th order polynomials. The capacitance value at 300K should be recorded at the start of a measurement. The zero-displacement point at any temperature can then be deduced by putting in the temperature and  $C(300\text{K})$  into this fit.

Once the displacement  $d$  is calculated using the method outlined above, the nominal strain along the x-direction,  $\epsilon_{xx}^{\text{disp}}$ , can be calculated by divide this displacement by the zero-volt mounting plate separation. Due to strain relaxation effects within the glue layers and the mounting plates, the actual strain,  $\epsilon_{xx}$  will be different from the nominal value  $\epsilon_{xx}^{\text{disp}}$  due to glue relaxation. Finite element simulation shows this relaxation causes the strain response of the sample to drop from its nominal value by a factor of  $0.7 \pm 0.07$  [65] This will be discussed further in Chapter 3.

### Thermometry

Since the cell has a sizable thermal mass, there will be a significant temperature lag between the cell body and the cryostat. Therefore, to achieve accurate temperature measurement, a Cernox CX-150 temperature sensor was attached to the strain device's body and sampled using Lakeshore 336. The sensor is attached firmly with the body with a screw and a washer, and the wires are thermally anchored to the cell body by wrapping it at least three turns around a stainless steel pole that was screwed to the cell body. The temperature sweep rate is set to 0.5K/minute for all measurements yielding a temperature lag of the sample to the cell body of around 0.1K. The cooldown and warm-up rate should never exceed 10K/minute, and the voltage across the PZTs need to be monitored

during the cooldown/warm-up (by shorting or connecting to a voltage source) to prevent damages to the cell.

### 2.2.3 Hydrostatic pressure

Hydrostatic pressure experiments were performed using a *Quantum Design* HPC-30 Cu-Be based self-clamping pressure cell. Although this version is no longer commercially available, information on the very similar updated version, HPC-33, can be found on the *Quantum Design* website. The sample was loaded according to the procedure suggested by the manufacturer. Hydrostatic pressure up to  $\sim 2.5$  GPa can be applied using a hydraulic press, and Daphne Oil 7373 is used as a pressure transfer medium. The freezing point of the Daphne oil is always below room temperature for pressures less than 2 GPa, which ensures a high degree of hydrostaticity throughout the pressure range [66]. Pressure measurements were performed by probing the superconducting transition temperature of a lead manometer [67]. In addition, the temperature dependence of the hydrostatic pressure within the HPC-30 pressure cell was determined by calibration measurements using both a lead and a manganin manometer [68]. Below 100K, the hydrostatic pressure was found to be almost independent of temperature. All the hydrostatic pressure measurements were done using the resistivity option in *Quantum Design* Physical Properties Measurement System (PPMS).

## 2.3 Measuring the critical temperatures $T_S$ of the nematic phase transition

The primary experiments described in this thesis revolve around measuring the change in the critical temperature of the nematic phase transition of certain iron-based superconductors as a function of strain. Hence, we need first to establish how best to measure  $T_S$ .

The signature of a phase transition usually comes in the form of anomalies in thermodynamic quantities because a phase transition is characterized by divergence of certain derivatives of appropriate thermodynamic potentials. Examples are a peak-like anomaly with hysteresis in heat capacity, which indicates a first-order transition, or a step-like anomaly in heat capacity, which indicates mean-field second-order transition. When a true thermodynamic transition occurs, the critical temperature of the phase transition can be determined without ambiguity - because the transition is sharp, the critical temperature is at the point of anomaly. In reality, the anomaly is often rounded to some extent, due to imperfection or the presence of conjugate field to the order parameter. In this work, we are concerned to measure the critical temperature of the nematic phase transition,  $T_S$ . As mentioned in chapter 1, the nematic is characterized by an Ising order parameter. The upper critical dimension of the Ising model with long range strain interaction is 2 [69, 70] and hence the

phase transition is mean-field. As a consequence, the heat capacity in an ideal case, is the characteristic vertical step. The critical temperature of the nematic phase transition is approximated to be at the extremum of the temperature derivative of the heat capacity. This may present some inaccuracy in  $T_S$ , as there is no guarantee that any rounding due to sample inhomogeneity will be symmetrical around  $T_S$ ; however, this is not significant because we are interested in the variation in  $T_S$  as a function of strain, not its absolute value. We then fit the feature to Gaussian distribution.  $T_S$  is then defined as the mean, and the standard deviation is the 95% confident interval of the fit parameter.

There are, however, problems associated with using heat capacity to determine the transition temperatures. With the relaxation time method, there is a need to thermally isolate the sample, which is very difficult to do while deforming the material. It is also time-consuming, and the signal-to-noise ratio is low. The problems here can be avoided using transport measurement, enabled by Fisher-Langer theorem [60], which relates heat capacity of the critical degrees of freedom and temperature derivatives of heat capacity. This is the basis for using resistivity and elastoresistivity to determine  $T_S$ . In some samples, elastocaloric effect is also used to determine  $T_S$ , since this is a direct probe to the critical part of heat capacity (see Section 1.3.4).

### The Fisher-Langer theorem

Before jumping into the experimental details, I would like to discuss the Fisher-Langer theorem briefly. Fisher and Langer argued in their seminal paper [60] that the dominant contribution to the magnetic resistivity  $\rho_{\text{mag}}$  of a metal is due to short-range magnetic fluctuation, and  $d\rho_{\text{mag}}/dT$  should vary like the magnetic specific heat. The derivation is carried out in a localized ferromagnet with conduction electrons; however, empirical evidence and further theoretical treatments have shown that this result is also pertinent with other types of long-range orders such as itinerant magnet or electronic nematic order [71]. Figure 2.2 shows the comparison between heat capacity, the temperature derivative of the resistivity, elastoresistivity, and elastocaloric measurements in the prototypical  $\text{Ba}(\text{Fe}_{0.975}\text{Co}_{0.025})_2\text{As}_2$ . Even though some differences can be seen between these measurements, the critical temperatures determined from each method are identical. This guarantees that the three techniques I will discuss below are valid ways to measure the critical temperature.

#### 2.3.1 Resistivity

The anomaly associated with nematic phase transition in heat capacity comes in the form of a mean-field step. This anomaly is usually sharp at lower cobalt concentrations but broadens at higher concentrations. According to the Fisher-Langer relation, this step-like anomaly will be seen in the temperature derivative of the resistivity. Therefore, one can extract the critical temperature  $T_S$  by fitting a Gaussian distribution to the second derivative of the resistivity  $d^2\rho/dT^2$ . The example can be seen in Fig.2.4A, taken from the hydrostatic pressure experiment. At 4.8% cobalt concentration,

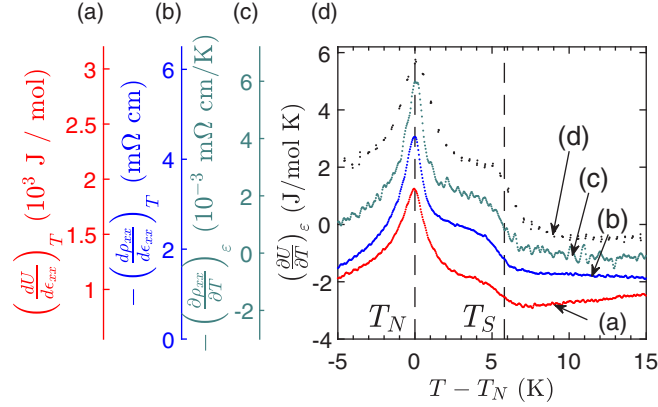


Figure 2.2: (a)(d) Temperature and strain derivatives of the resistance and internal energy  $U$  in  $\text{Ba}(\text{Fe}_{0.975}\text{Co}_{0.025})_2\text{As}_2$  in proximity to the successive nematic and magnetic transitions, each plotted against a single corresponding axis on the left. The heat capacity  $(\frac{\partial U}{\partial T})_\epsilon$  is shown in black. The characteristic mean-field step at  $T_S$  is rounded due to inhomogeneity, where with a width of approximately 1K. This figure shows that resistivity (green), elasto-resistivity (blue), and elastocaloric effect (red) are appropriate tools for determination of the critical temperatures. Reproduced from [71] with the permission of the American Physical Society.

the disorder effect broadens this step-like anomaly. The critical temperature can be determined by fitting a Gaussian distribution to the data in the vicinity of the peak.

This method is suitable for measuring under hydrostatic pressure environment. However, there can be more strain inhomogeneity in uniaxial stress environment, making the feature less pronounced. There is a need for a better way to extract the critical temperature, which I address below.

### 2.3.2 Elasto-resistivity

The problem with using the second derivative of the resistivity is that it is done numerically, and if inadequate smoothing is applied, it will result in oscillations in the second derivative. We found an alternative way to avoid numerical second derivative using oscillating stress.

Since  $A_{1g}$  and  $B_{1g}$  strain only shift the transition temperature and nothing else, at least close to the critical point, one can write the resistivity as a function of reduced temperature:  $\rho = \rho(T - T_S(\epsilon_{xx}))$ . Note that  $\epsilon_{A_{1g}}$  and  $\epsilon_{B_{1g}}$  can be deduced from  $\epsilon_{xx}$  and the material's Poisson's ratio. The elasto-resistivity with respect to  $\epsilon_{xx}$  is:

$$\frac{\partial}{\partial \epsilon_{xx}} \rho(T - T_S(\epsilon_{xx})) = \frac{\partial \rho}{\partial T_S} \frac{\partial T_S}{\partial \epsilon_{xx}}. \quad (2.2)$$

Since  $\rho = \rho(T - T_S(\epsilon_{xx}))$ , one notices the relation  $\frac{\partial \rho}{\partial T} = -\frac{\partial \rho}{\partial T_S}$ . This gives us the relationship between

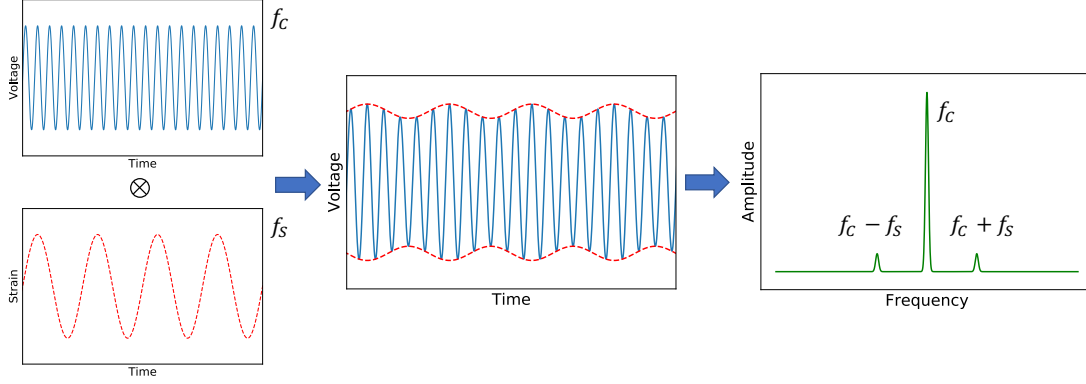


Figure 2.3: Schematic explanation of the amplitude demodulation method. The oscillating voltage signal of frequency  $f_c$  is modulated by the change of resistivity via elasto-resistivity at frequency  $f_s$ . This resulted in the signal in the middle panel which is described by 3 Fourier components. The amplitude of the resistivity change due to strain can be measured by lock in to the sideband signal. The mathematical description can be found in the main text.

$A_{1g}$  and  $B_{1g}$  elasto-resistivity and the temperature derivative of the resistivity as

$$\frac{\partial \rho}{\partial \epsilon_{xx}} = -\frac{\partial \rho}{\partial T} \frac{\partial T_S}{\partial \epsilon_{xx}} \propto \frac{\partial \rho}{\partial T} \propto C^{\text{crit}}. \quad (2.3)$$

This result suggests that elasto-resistivity can also be used as a probe for heat capacity close to the phase transition. In order to measure this quantity, we use the amplitude demodulation method developed in [57]. Here I briefly explain the method below.

### The amplitude demodulation method

Measurement of elasto-resistivity via amplitude demodulation method was developed in our group and explained in this paper [57]. Below is a brief outline of how the method works in the context of my experiment, and the schematic explanation is shown in Fig.2.3.

When oscillating strain is applied to the sample, the resistance of the sample will oscillate as a response to strain via the elasto-resistivity effect. The key is to measure the amplitude of this resistance oscillation. Slow oscillating strain (usually around 3 Hz) is applied on top of DC offset strain by applying a corresponding voltage signal to the outer PZT stacks. The resistance of the sample as a function of time can be expressed as

$$R(\epsilon_{xx,0} + \delta(t)) = R(\epsilon_0) + \left. \frac{dR}{d\epsilon_{xx}} \right|_{\epsilon=\epsilon_0} \times \delta_0 \sin(\omega_s t). \quad (2.4)$$

Here,  $\delta(t)$  is a small oscillating strain, and  $\omega_s$  is its frequency. AC current of  $\sim 100$ Hz is passed through the sample resulting in an AC voltage with slowly varying amplitude which can be expressed

as

$$V = I(t)R(t) = I_0 \sin(\omega_c t) \times R(\epsilon_0) + \frac{I_0}{2} \left. \frac{dR}{d\epsilon_{xx}} \right|_{\epsilon=\epsilon_0} \delta_0 \times [\cos(\omega_c - \omega_s)t - \cos(\omega_c + \omega_s)t] \quad (2.5)$$

where  $\omega_c$  is the carrier frequency, and the last term is obtained from trigonometry product identity. Notice that the quantity  $dR/d\epsilon_{xx}$  in the second term on the right-hand side of the equation is precisely elastoresistance of the sample, which is directly proportional to the critical part of the heat capacity. This can be measured by lock-in detection of the sideband (at either frequency  $\omega_c \pm \omega_s$ ) using the dual mode of a *Stanford Research* SR860 lock-in amplifier. The signal will appear in the Y-component of the sideband, (since the sideband is  $\cos(\omega_c \pm \omega_s)$ ). A step-like anomaly in this sideband signal can then be used to identify the critical temperature (Fig.2.4B).

This technique is particularly useful in uniaxial stress experiments on samples with higher cobalt concentrations. For these materials, the signature of the phase transition is smeared by disorder and strain anisotropy. Thus a superior signal-to-noise ratio of this technique significantly reduces the uncertainty in  $T_S$ .

### 2.3.3 Elastocaloric effect

Another method to obtain the critical temperature is to use the elastocaloric method, as shown in Section 1.3.4, the temperature change due to elastocaloric effect in an adiabatic condition is directly proportional to the critical part of the heat capacity:  $dT = \frac{C^{\text{crit}}}{C} \frac{dT_S}{d\epsilon} d\epsilon$ . The tricky part of this measurement is how to find an appropriate thermodynamic condition. Traditional elastocaloric measurement is done using the relaxation time method: quickly ramping the applied stress to the material and measuring temperature response. This method requires a high precision measurement of a tiny signal. Instead, I use the new AC elastocaloric technique developed in our group [61]. Below is a brief outline of the technique.

#### AC Elastocaloric effect

The following technique was developed in our group and published in this seminal paper [61]. Here is a outline of this method in the context of my experiment.

First and foremost, this method must be done in an environment with minimal thermal contact to the thermal reservoir. The uniaxial stress setup with *Razorbill instrument* stress cell is a desirable choice. Temperature oscillation caused by oscillating strain via elastocaloric effect is measured by affixing a type-E thermocouple onto the sample with a thin layer of Angstrom bond AB9110LV. The thermocouple consists of Constantan and Chromel wires, each with diameters of 12.5  $\mu\text{m}$ , spot welded together. The other ends of the thermocouple are attached to the cell body as a reference temperature. The signal is amplified using *Stanford Research* SR554 transformer preamplifier before feeding into *Stanford Research* SR860 lock-in amplifier. (Note that the strain cell is excited using

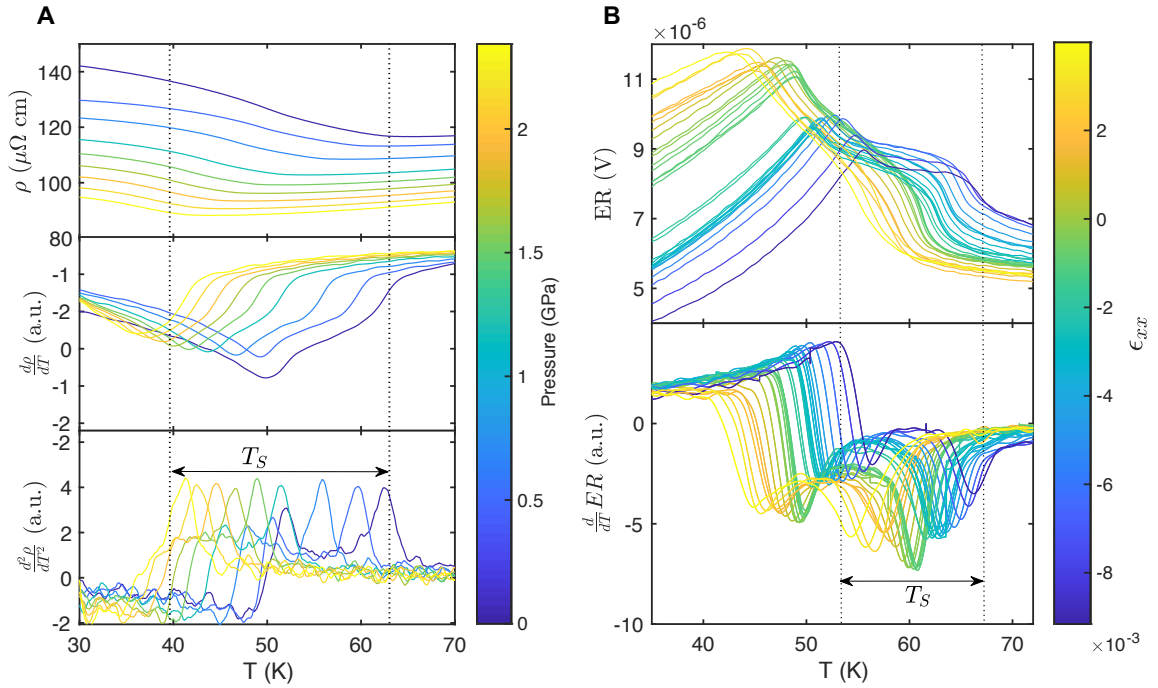


Figure 2.4: **Measurement of the critical temperature  $T_S$ .** (A) Resistivity traces and their temperature derivatives for a prototypical  $x = 4.8\% \pm 0.2\%$  under various hydrostatic pressures. The step like anomalies in  $d\rho/dT$  found at high temperature of each trace signify the nematic phase transition.  $T_S$  is then located at the peak of  $d^2\rho/dT^2$ . (B) sideband traces and their temperature derivatives for a prototypical  $x = 4.8\% \pm 0.2\%$  under various uniaxial stresses. The top panel shows the sideband signal which is directly proportional to the elasto-resistivity (ER). The nematic phase transition occurs at the step-like anomalies in the ER traces.  $T_S$  is thus located at the peaks of  $d(ER)/dT$ . Reproduced from [72] with the permission of the American Association for the Advancement of Science.

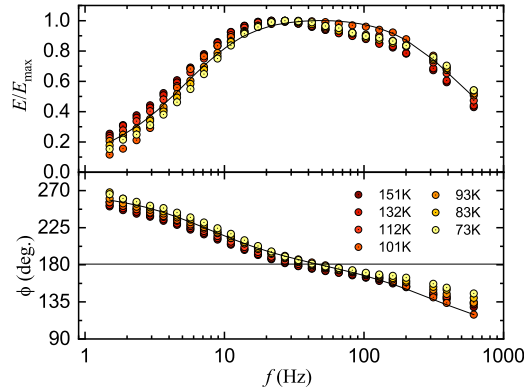


Figure 2.5: Thermal transfer function taken at various temperature. Reproduced from [61] with the permission of the American Institute of Physics.

the same lock-in amplifier and *Tegam* 2350 power amplifier, the lock-in is therefore set into internal reference mode).

In order to obtain an appropriate thermodynamic condition (i.e. quasi-adiabatic), the strain frequency needs to be at an appropriate value. In theory, the true adiabatic condition is met at infinite strain frequency. However, there will be no heat leak into the environment at this frequency, including to the thermocouple, rendering the measurement impossible. At low frequency limit, the sample will be in thermal equilibrium with the heat bath at all times, yielding isothermal condition. It is only in the intermediate frequency where a quasi-adiabatic condition is satisfied. The amount of temperature oscillation detected by the thermocouple when changing frequency (and thus change thermodynamics condition) is called the thermal transfer function.

Fig.2.5 shows a typical thermal transfer function. The y-axis is the signal from the thermocouple, normalized by its maximum value. The middle part (frequency  $\sim 30\text{Hz}$ ) presents a plateau in which the quasi-adiabatic condition is met. The temperature dependence of this frequency plateau is small; therefore, setting the frequency at this plateau guarantee quasi-adiabatic condition throughout the measurement. An example of elastocaloric measurement as a function of temperature and uniaxial stress can be seen in Fig.2.6.

## 2.4 Measurement of nematic susceptibility

As I have shown in Section 1.3.3, the elastoresistivity coefficient  $m_{B_{2g}, B_{2g}}$  is a proxy for the nematic susceptibility. The technique I will be using to measure this quantity is called the *transverse elastoresistivity* method developed in [59]. This section will outline how to measure the  $m_{B_{2g}, B_{2g}}$ , however the quantity measured in Chapter 5 is not exactly  $m_{B_{2g}, B_{2g}}$  since the nematic order parameter is not induced by  $\epsilon_{B_{2g}}$ , but rather a new conjugate field  $\epsilon_{B_{2g}} H_z$ . This section will hopefully elucidate the

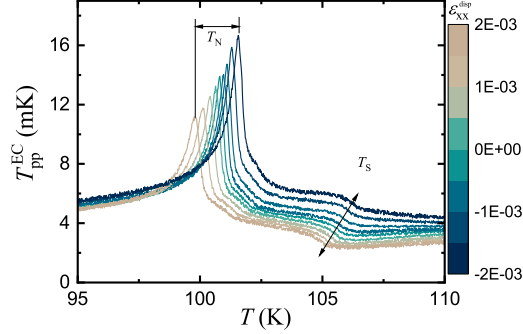


Figure 2.6: Elastocaloric effect with strain in the  $B_{1g} + A_{1g}$  configuration measured as a function of temperature for different offset strain. The rounded step-like feature associated with  $T_S$  is clearly visible, and its strain dependence can be readily extracted. Reproduced from [61] with the permission of the American Institute of Physics.

readers on how the nematic susceptibility is usually measured, and then we will discuss the specifics in Chapter 5.

### Transverse elastoresistivity technique

To measure  $\left(\frac{\Delta\rho}{\rho}\right)_{B_{2g}}$  using the transverse elastoresistivity method, the sample needs to be cut and aligned along  $[100]$  crystallographic direction. The sample is then glued at  $45^\circ$  to the PZT stack, inducing the  $B_{2g}$  strain. In this orientation, the  $B_{2g}$  fractional change in resistivity,  $\left(\frac{\Delta\rho}{\rho}\right)_{B_{2g}}$ , can be expressed in the cartesian coordinate as

$$\left(\frac{\Delta\rho}{\rho}\right)_{B_{2g}} = \left(\frac{\Delta\rho}{\rho}\right)_{xy} = \frac{\Delta\rho_{xy}(\epsilon)}{\sqrt{\rho_{xx}(\epsilon=0)}\sqrt{\rho_{yy}(\epsilon=0)}} = \frac{\Delta\rho_{xy}}{\rho_{xx}}, \quad (2.6)$$

according to their definition in Eq. 1.6 and Eq. 1.8. The last equality comes from the fact that  $\rho_{xx} = \rho_{yy}$  in the tetragonal phase. Therefore, simply measuring the transverse resistivity in tandem with longitudinal resistivity is sufficient to calculate  $\left(\frac{\Delta\rho}{\rho}\right)_{B_{2g}}$ . It is important, however, to note that the measurement of the transverse voltage  $V_y$  will have some part of the longitudinal voltage  $V_x$  bleed into it due to the contact misalignment. To correct this, the measured transverse voltage is written as

$$V_y^{\text{measured}} = V_y + l \times V_x, \quad (2.7)$$

where  $l$  is the geometric factor, which can be determined by measuring  $V_y^{\text{measured}}$  and  $V_x$  at room temperature and zero strain, where  $V_y = 0$ . The setup is illustrated in Fig.2.7.

To measure the elastoresistivity coefficient, one resort to the definition introduced in Section

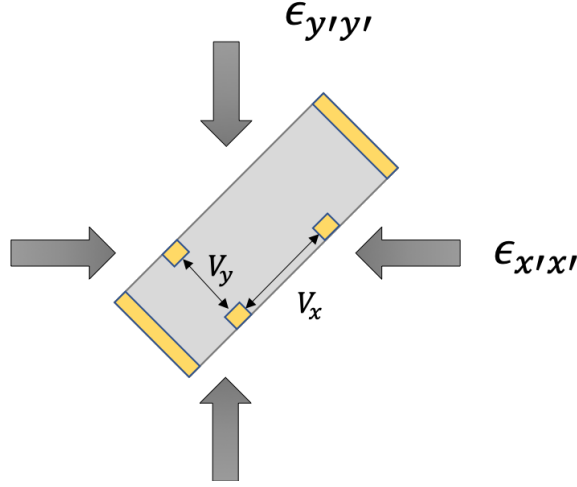


Figure 2.7: Figure illustrates measurement of elastoresistivity in transverse configuration. Sample is glued 45° to the strain axis. The actual transverse voltage can be measured by subtracting the longitudinal contamination from the measured transverse voltage as explained in the main text.

1.3.3:

$$m_{B_{2g}, B_{2g}} = \frac{d}{d\epsilon_{B_{2g}}} \left( \frac{\Delta\rho}{\rho} \right) \Big|_{B_{2g}} \Big|_{\epsilon=0} = \frac{1}{\rho_{xx}(\epsilon=0)} \frac{d\rho_{xy}}{d\epsilon_{B_{2g}}}, \quad (2.8)$$

where the last equality comes from Eq. 2.6 and that  $\frac{d\Delta\rho_{xy}}{d\epsilon_{B_{2g}}} = \frac{d\rho_{xy}}{d\epsilon_{B_{2g}}}$ .  $\rho_{xx}$  is measured using the standard lock-in technique using either *Stanford Research* SR830 or SR860. Similar to the previous section, the quantity  $\frac{d\rho_{xy}}{d\epsilon_{B_{2g}}}$  can be measured using the amplitude demodulation method.

### The amplitude demodulation method

Just like in the previous section, oscillating strain is applied to the sample, causing the transverse resistivity, and then transverse resistance  $R_{xy}$ , of the sample to oscillate:

$$R_{xy}(\epsilon_{B_{2g},0} + \delta(t)) = R_{xy}(\epsilon_0) + \frac{dR_{xy}}{d\epsilon_{B_{2g}}} \Big|_{\epsilon=\epsilon_0} \times \delta_0 \sin(\omega_s t), \quad (2.9)$$

Here,  $\delta(t)$  is a small oscillating  $B_{2g}$  strain, and  $\omega_s$  is its frequency. Since the setup is sample-on-PZT, there will be some offset  $B_{2g}$  strain that causes by the thermal expansion of the PZT and by the glue hardening. This is represented by the term  $\epsilon_{B_{2g},0}$  that is temperature-dependent. This offset strain will not affect the measured  $m_{B_{2g}, B_{2g}}$  as long as it is in the linear dependence region, and it has been shown previously with a prototypical iron-based superconductor using DC elastoresistivity [73] that this is the case at all temperatures.

Sourcing current through the sample at frequency  $\omega_c$ , the total overall voltage would result in 3

frequency components in Fourier space:

$$V_y = I_x(t)R_{xy}(t) = I_0 \sin(\omega_c t) \times R(\epsilon_0) + \frac{I_0}{2} \left. \frac{dR_{xy}}{d\epsilon_{B_{2g}}} \right|_{\epsilon=\epsilon_0} \delta_0 \times (\cos(\omega_c - \omega_s)t - \cos(\omega_c + \omega_s)t) \quad (2.10)$$

where  $\omega_c$  is the carrier frequency, and the last term is obtained from trigonometry product identity. The signal will appear in the Y-component of the sideband, (since the sideband is  $\cos(\omega_c \pm \omega_s)$ ). It is detected using the dual mode of a *Stanford Research* SR860 lock-in amplifier. From the sideband,  $S = \frac{I_0}{2} \left. \frac{dR_{xy}}{d\epsilon_{B_{2g}}} \right|_{\epsilon=\epsilon_0} \delta_0$ , the elastoresistivity  $d\rho/d\epsilon_{B_{2g}}$  can be calculated

$$\frac{d\rho_{xy}}{d\epsilon_{B_{2g}}} = \frac{2St}{I_0\delta_0}, \quad (2.11)$$

where  $t$  is the thickness of the sample.

The amplitude of the  $B_{2g}$  strain,  $\delta_0$ , can also be measured by measuring the change in resistance of the strain gauge, glued on the bottom of the PZT, using the amplitude demodulation method. Similar to Eq. 2.10, the voltage on the strain gauge is

$$V_{SG} = I_{0,SG} \sin(\omega'_c t) \times R_{SG}(\epsilon_0) + \frac{I_{0,SG}}{2} \left. \frac{dR_{SG}}{d\epsilon_{xx}} \right|_{\epsilon=\epsilon_0} \delta_{0,xx} \times (\cos(\omega'_c - \omega_s)t - \cos(\omega'_c + \omega_s)t), \quad (2.12)$$

where  $\omega'_c$  is the frequency of the current through strain gauge, and since the strain gauge measures either  $\epsilon_{xx}$  or  $\epsilon_{yy}$ , the  $\delta$  measured will be in the  $xx$  or  $yy$  components. Using the definition of gauge factor from Eq. 2.1,

$$GF = \frac{1}{R_{SG}} \frac{dR_{SG}}{d\epsilon_{xx}}. \quad (2.13)$$

Since the gauge factor GF is measured accurately by the manufacturer, the strain amplitude  $\delta_{0,xx}$  can be calculated by dividing the sideband amplitude  $S_{SG} = \frac{I_{0,SG}}{2} \left. \frac{dR_{SG}}{d\epsilon_{xx}} \right|_{\epsilon=\epsilon_0} \delta_{0,xx}$  by the central band amplitude  $C_{SG} = I_{0,SG}R_{SG}(\epsilon_0)$ .

$$\frac{S_{SG}}{C_{SG}} = \frac{1}{2} \frac{1}{R_{SG}} \left. \frac{dR_{SG}}{d\epsilon_{xx}} \right|_{\epsilon=\epsilon_0} \delta_{0,xx} = \frac{1}{2} GF \times \delta_{0,xx}. \quad (2.14)$$

Since  $GF \simeq 2$ , the strain amplitude is simply

$$\delta_{0,xx} = S_{SG}/C_{SG}. \quad (2.15)$$

To calculate  $\delta_{0,B_{2g}}$ , one can measure both  $\delta_{0,xx}$  and  $\delta_{0,yy}$ . Then  $\delta_{0,B_{2g}} = \frac{1}{2}(\delta_{0,xx} - \delta_{0,yy})$ . Alternatively, one can approximate this using the Poisson's ratio of the PZT. Since  $\delta_{0,yy} = -\nu_P \delta_{0,xx}$ ,  $\delta_{0,B_{2g}} = \frac{1}{2}(1 + \nu_P)\delta_{0,xx}$ .

## Chapter 3

# Establishing symmetry-breaking strain as a tuning parameter

We report the separate response of the critical temperature of the nematic phase transition  $T_S$  to symmetric and antisymmetric strains for the prototypical underdoped iron pnictide  $\text{Ba}(\text{Fe}_{0.975}\text{Co}_{0.025})_2\text{As}_2$ . This decomposition is achieved by comparing the response of  $T_S$  to in-plane uniaxial stress and hydrostatic pressure. In addition to quantifying the two distinct linear responses to symmetric strains, we find a quadratic variation of  $T_S$  as a response to antisymmetric strains  $\varepsilon_{B_{1g}} = \frac{1}{2}(\varepsilon_{xx} - \varepsilon_{yy})$ , exceeding the non linear response to symmetric strains by at least two orders of magnitude. These observations establish orthogonal antisymmetric strain as a powerful tuning parameter for nematic order. The results in this chapter are published in [65] and the text and figures are reproduced from that reference with the permission of the American Physical Society. The experiment performed in this chapter was done in close collaboration with M.S. Ikeda.

### 3.1 Introduction

Electronic nematic order is found in several families of Fe-based superconductors [74, 75, 76, 31, 17, 32, 77] and also suggested to be an important aspect within the phase diagram of at least some cuprate high-temperature superconductors [78, 79, 80, 81, 82, 83, 84]. In order to assess the relevance of nematic fluctuations for superconductivity [85, 86, 43, 42, 45, 47, 44, 87], new methods are required to continuously tune the critical temperature of the nematic phase transition, with the ultimate goal of potentially providing access to a nematic quantum phase transition with a smoothly adjustable external parameter. Here we show how symmetric and antisymmetric strains induced by external stresses can be used as separate tuning parameters for nematic order. We demonstrate this for a representative underdoped Fe-pnictide,  $\text{Ba}(\text{Fe}_{0.975}\text{Co}_{0.025})_2\text{As}_2$ , but emphasize that these ideas

are quite general for nematic order. More broadly, the notions of symmetry decomposition that we employ can be applied to access strains as tuning parameters for other types of phase transitions, thus offering a road map to gain further insight into most existing stress based phase diagrams.

The irreducible representations of the crystallographic point group provide a natural basis in which to express strains experienced by a solid. Within the  $D_{4h}$  point group, appropriate for the specific material discussed in this paper, the 6 independent components of the strain tensor can be decomposed into two components that are symmetric with respect to the primary ( $C_4$ ) rotation of the point group ( $\epsilon_{A_{1g},1} = \frac{1}{2}(\epsilon_{xx} + \epsilon_{yy})$ ,  $\epsilon_{A_{1g},2} = \epsilon_{zz}$ , Fig. 3.1(c)(i)), two components that are antisymmetric ( $\epsilon_{B_{1g}} = \frac{1}{2}(\epsilon_{xx} - \epsilon_{yy})$  and  $\epsilon_{B_{2g}} = \epsilon_{xy}$ , Fig. 3.1(c)(ii) and (iii)) and two components that belong to an  $E_g$  representation, comprising vertical shear,  $\epsilon_{E_g} = (\epsilon_{xz}, \epsilon_{yz})$ . The specific challenge is to separately determine the effects of each of these strain components on the critical temperature  $T_c$  of a phase transition. In this paper we demonstrate how this can be achieved by comparison of the response to two (or more) different stress conditions (illustrated in Fig. 3.1(a,b)). This decomposition not only reveals the relative roles of in-plane and out-of-plane symmetric strains, but also establishes orthogonal antisymmetric strain as a powerful new tuning parameter for nematic order.

As broken symmetries are the most fundamental organizing principle for (solids and) phase transitions, we start by reviewing the symmetry constraints for the nematic transition in underdoped Fe-pnictide superconductors, like  $\text{Ba}(\text{Fe}_{0.975}\text{Co}_{0.025})_2\text{As}_2$  studied here. The nematic order parameter and associated lattice distortion that onset at the coupled nematic/structural phase transition at  $T_S$  have a  $B_{2g}$  symmetry (broken  $C_4$  rotation and horizontal and vertical mirrors/rotations). Hence, an external stress that induces an antisymmetric strain with a  $B_{2g}$  symmetry (Fig. 3.1(c)(iii)) necessarily induces a finite order parameter at all temperatures and therefore smears the phase transition [31, 88, 89, 90]. Stresses that induce the *orthogonal* antisymmetric strain,  $\epsilon_{B_{1g}}$ , however, preserve the horizontal and vertical mirrors/rotations (Fig. 3.1(c)(ii)). Consequently, a nematic phase transition is still permitted and  $\epsilon_{B_{1g}}$  can therefore be used as a continuous tuning parameter for the phase transition. Since  $T_S$  is an isotropic quantity (invariant under ( $C_4$ ) rotation), antisymmetric strain  $\epsilon_{B_{1g}}$  can affect  $T_S$  only in even powers, thus  $\lambda_{B_{1g}} \equiv \partial T_S / \partial \epsilon_{B_{1g}} = 0$  ( $\lambda_{(B_{1g}, A_{1g}, i)} \equiv \partial^2 T_S / \partial \epsilon_{B_{1g}} \partial \epsilon_{A_{1g}, i} = 0$ ). In contrast, the two symmetric strain components  $\epsilon_{A_{1g},1}$  and  $\epsilon_{A_{1g},2}$  do not lower the crystal symmetry (Fig. 3.1(c)(i)) and therefore to leading order affect  $T_S$  linearly. Hence, considering both  $A_{1g}$  and  $B_{1g}$  symmetry strains, to second order the critical temperature  $T_S$  is given by

$$\begin{aligned}
 T_S = T_S(0) &+ \sum_{i=1}^2 \lambda_{(A_{1g}, i)} \epsilon_{A_{1g}, i} + \\
 &+ \sum_{i \leq j=1}^2 \lambda_{(A_{1g}, i, A_{1g}, j)} \epsilon_{A_{1g}, i} \epsilon_{A_{1g}, j} + \lambda_{(B_{1g}, B_{1g})} \epsilon_{B_{1g}}^2,
 \end{aligned} \tag{3.1}$$

defining the coefficients  $\lambda_i$  that are to be measured. This is achieved by comparing measurements of  $T_S(\epsilon)$  obtained from uniaxial stress and hydrostatic pressure experiments.

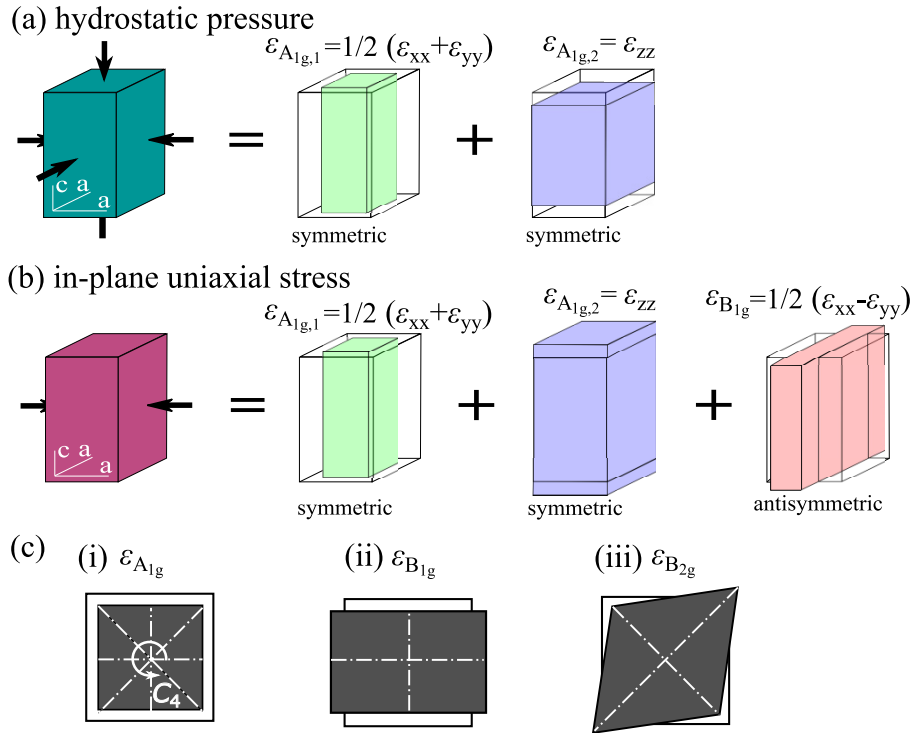


Figure 3.1: Schematic representation of strains experienced by a tetragonal material while held under (a) hydrostatic pressure, and (b) uniaxial stress applied along the  $[100]$  direction. Black arrows indicate stress. The strain tensor (right side of symbolic equations (a) and (b)) is derived by multiplying the stiffness and the stress tensor (left side). White arrows in panel (a) and (b) indicate the orientation of the tetragonal crystal axes. In each case, the strain tensor experienced by the material is decomposed into irreducible representations of the crystal symmetry. For materials with regular mechanical properties (i.e. a positive out-of-plane Poisson ratio and an in-plane Poisson ratio smaller than 1), the symmetric strain modes  $\epsilon_{A_{1g},i}$  share the same sign (are both compressive) during hydrostatic pressure experiments, but have opposite sign during uniaxial stress experiments. Panel (c) illustrates in-plane deformations as well as the associated preserved symmetries (white lines). While symmetric  $A_{1g}$  strain preserves  $C_4$  rotational symmetry (white arrow) as well as vertical, horizontal, and diagonal mirror planes (white dash dotted lines), antisymmetric  $B_{1g}$  and  $B_{2g}$  strains lower the primary rotational symmetry to  $C_2$  and break diagonal and vertical mirror planes, respectively.

## 3.2 Experimental Methods

For both hydrostatic, and uniaxial stress experiments, the transition temperatures are determined from resistivity data (Fig. 3.2,3.3 (a)). The longitudinal resistivity  $\rho_{xx}$  as a function of temperature was determined during slow temperature sweeps (down and up for each  $\epsilon_{xx}$ ) using a standard four probe technique (see Appendix 3.B) on a crystal contacted using PbSn reflow solder (for more details see Appendix 3.A ). The coupled structural/nematic transition temperature  $T_S$  was determined from the center of a Gaussian function fit to a local maximum in the second derivative (Fig. 3.2,3.3 (c)), the magnetic transition temperature  $T_N$  from a minimum in the first derivative (Fig. 3.2,3.3 (b)). An upper bound for the error bar around  $T_S$  is estimated by half the standard deviation of the Gaussian function <sup>1</sup>.

Uniaxial stress experiments were performed using a commercially available strain apparatus (CS100, *Razorbill instruments*). Uniaxial stress was applied along a bar shaped sample of  $\text{Ba}(\text{Fe}_{0.975}\text{Co}_{0.025})_2\text{As}_2$  (with typical dimension  $2000 \times 400 \times 35 \mu\text{m}$ ) by affixing it in between two mounting plates that are pushed together/pulled apart using voltage controlled lead zirconate titanate (PZT) stacks. The cell is designed to compensate for the thermal expansion of the PZT stacks [64]. Furthermore, due to matching of the thermal expansion of  $\text{Ba}(\text{Fe}_{1-x}\text{Co}_x)_2\text{As}_2$  [91] and the sample mounting plates (titanium) (see Appendix 3.B.1, Fig. 3.7 ), the strain on the sample is almost perfectly independent of temperature for a fixed voltage applied to the PZT stacks. Stress was applied along the tetragonal [100] axis resulting in a combination of  $\epsilon_{A_{1g},1}$ ,  $\epsilon_{A_{1g},2}$ , and  $\epsilon_{B_{1g}}$  (see Fig. 3.1 (b)). The misalignment of the [100] crystal and the stress axis was estimated to be smaller than  $2.5^\circ$  by comparing to a uniaxial stress experiment on a crystal oriented such that stress was applied along the tetragonal [110] axis (see Appendix 3.B.1). The nominal strain along the tetragonal [100] axis ( $\epsilon_{xx}^{\text{disp}}$ ) was determined by the zero strain length of the sample between the mounting plates and the length change measured by sampling a capacitance sensor using an *Andeen-Hagerling* AH2550A capacitance bridge. Due to strain relaxation effects in the mounting plates and the mounting glue, the actual strain  $\epsilon_{xx}$  experienced by the sample is smaller than  $\epsilon_{xx}^{\text{disp}}$ . Using finite element simulations (see Appendix 3.C ), we estimate  $\epsilon_{xx} = (0.7 \pm 0.07)\epsilon_{xx}^{\text{disp}}$ . The extracted critical temperature can be well fit by  $T_S(\epsilon_{xx}) = T_S(\epsilon_{xx} = 0) + \alpha\epsilon_{xx} + \beta\epsilon_{xx}^2$  (red line, <sup>2</sup>), with  $\alpha = -521 \pm 4 \text{ K}$  and  $\beta = -28300 \pm 1100 \text{ K}$ . As we will show later, the surprisingly large quadratic response is due solely to antisymmetric strain,  $\epsilon_{B_{1g}}$ .

The second experiment reported here is electrical resistivity on a bar shaped ( $1000 \times 600 \times 30 \mu\text{m}$ ) crystal of  $\text{Ba}(\text{Fe}_{0.975}\text{Co}_{0.025})_2\text{As}_2$  as a function of temperature under hydrostatic pressure (Fig. 3.3). The measurements were performed using a HPC-30 pressure cell within a PPMS from *Quantum*

<sup>1</sup>The 95% confidence interval of the center of the Gaussian function is smaller than  $\pm 50 \text{ mK}$  in each case. To also take into account systematic uncertainty introduced by data smoothing or the potentially asymmetric shape of the peak around  $T_S$ , we empirically determined half the standard deviation as an upper bound for the experimental uncertainty.

<sup>2</sup>Note that Fig. 3.2 (d) shows the fits on the original data, before correction for strain relaxation effects using  $\epsilon_{xx} = 0.7\epsilon_{xx}^{\text{disp}}$

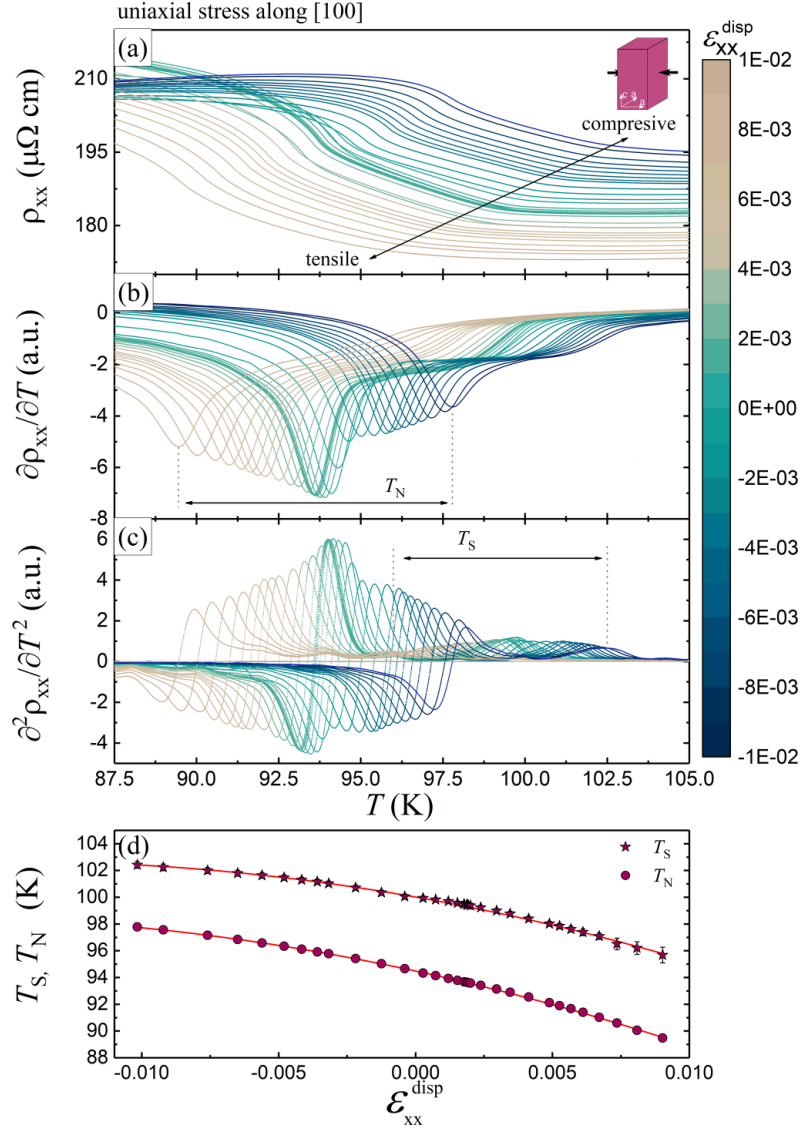


Figure 3.2: (a) Electrical resistivity of  $\text{Ba}(\text{Fe}_{0.975}\text{Co}_{0.025})_2\text{As}_2$  as a function of temperature determined during a uniaxial stress experiment. For each temperature sweep (warming) shown here, the sample is held at a constant strain,  $\epsilon_{xx}^{\text{disp}}$ , indicated by the color scale (blue data points indicate compressive strain, beige points tensile strain, and cyan colored data small strain around the strain neutral point). Panel (b) and (c) show the first and second derivative of the resistivity with respect to temperature. Panel (d) shows  $T_S$  and  $T_N$  versus nominal strain  $\epsilon_{xx}^{\text{disp}}$ . The red lines are fits using a second order polynomial resulting  $T_S(\epsilon_{xx}) = 100 - (521 \pm 4)\epsilon_{xx} - (28300 \pm 1100)\epsilon_{xx}^2$ , and  $T_N(\epsilon_{xx}) = 94.5 - (629 \pm 2)\epsilon_{xx} - (24700 \pm 500)\epsilon_{xx}^2$ .

*Design* using Daphne oil 7373 as pressure medium . The hydrostatic pressure was determined by measuring the superconducting transition temperature of a lead manometer. Under perfectly hydrostatic conditions (for details see Appendix 3.B.2) the strain is purely symmetric, and both  $\epsilon_{A_{1g},1}$  and  $\epsilon_{A_{1g},2}$  are compressive (Fig. 3.1(a)). Both transitions are found to vary almost perfectly linearly

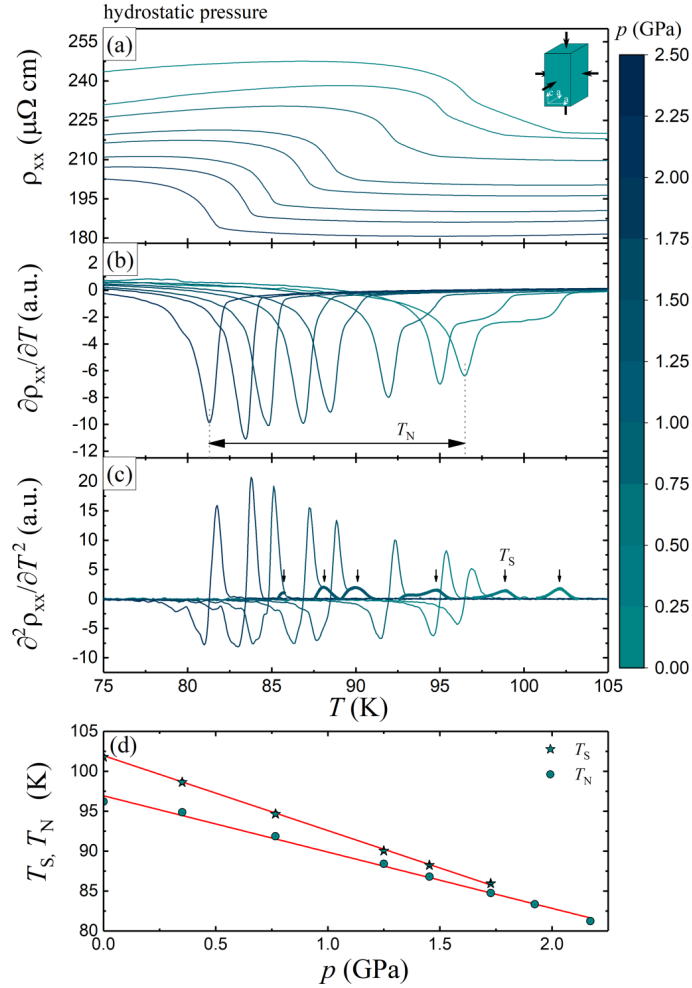


Figure 3.3: (a) Temperature dependence of the electrical resistivity  $\rho$  of  $\text{Ba}(\text{Fe}_{0.975}\text{Co}_{0.025})_2\text{As}_2$  for a range of hydrostatic pressures  $p$  determined during slow warming temperature sweeps. Panel (b) and (c) show the first and second derivative with respect to temperature, respectively. The dotted lines in panel (c) shows second derivatives calculated neglecting resistivity data below  $T_N + 1\text{K}$ , avoiding overlap of the smoothed signatures of the features associated with  $T_N$  and  $T_S$  . Similar to Fig. 3.2, blue colored symbols indicate compressive strains. Panel (d) again shows the structural and antiferromagnetic transition temperature as a function of pressure. The red lines in panel (d) are linear fits to the data.

under hydrostatic pressure, though with a slightly different slope (see Fig. 3.3(d)), thus merging for

pressures greater than approximately 1.75 GPa. A linear fit results in  $T_S(P) = T_S(P = 0) + \tilde{\alpha}P$ , where  $\tilde{\alpha} = -9.38 \pm 0.08$  K/GPa.

### 3.3 Results and Discussion

To decompose the strain induced changes of  $T_S$ , the relative amount of strains within each of the different symmetry channels is first determined, based on the measured elastic stiffness tensor [92] (see Appendix 3.C.1). The linear response (which, as described earlier, can only arise due to symmetric strain) can then be plotted as a function of the decomposed strains  $\epsilon_{A_{1g},1}$  and  $\epsilon_{A_{1g},2}$  (Fig. 3.4). For hydrostatic pressure (cyan plane in Fig. 3.4) the response is purely linear, so no subtraction is necessary. For uniaxial stress, the quadratic term ( $\beta\epsilon_{xx}^2$ , defined earlier) is first subtracted using the fitted value of  $\beta$ , to leave the linear response:  $T_S^{\text{lin}}(\epsilon_{xx}) = T_S(\epsilon_{xx}) - \beta\epsilon_{xx}^2$  (purple stars in Fig. 3.4). Since the ratio of  $\epsilon_{A_{1g},1}$  and  $\epsilon_{A_{1g},2}$  is different for the two experiments, the purple and cyan planes in Fig. 3.4 are not parallel. Moreover, since two lines define a plane, the material's response to symmetric strain (yellow plane in Fig. 3.4) is uniquely defined by these two sets of measurements. A full decomposition of the response to symmetric strains is now possible, and the associated partial derivatives are readily determined;  $\lambda_{(A_{1g},1)} = -6.35 \pm 0.23$  K/%, and  $\lambda_{(A_{1g},2)} = 16.70 \pm 0.32$  K/%<sup>3</sup> (for details see Appendix 3.D). The ratio of these terms  $\lambda_{(A_{1g},2)}/\lambda_{(A_{1g},1)} = -2.63 \pm 0.11$  demonstrates that c-axis strains have a considerably larger effect on  $T_S$  than symmetric in-plane strains. Considering the contributions of symmetric strain to a standard Landau free energy expansion of the nematic phase transition (discussed further below), we note that the finite values of  $\lambda_{(A_{1g},1)}$  and  $\lambda_{(A_{1g},2)}$  necessarily imply the formation of spontaneous symmetric strains  $\epsilon_{A_{1g},1}$  and  $\epsilon_{A_{1g},2}$  upon cooling below  $T_S$ . That  $\lambda_{(A_{1g},1)}$  and  $\lambda_{(A_{1g},2)}$  have opposite signs, is consistent<sup>4</sup> with the observation that the spontaneous strains as measured in recent thermal expansion experiments [93] have opposite signs.

Having decomposed the linear response, we turn to the quadratic response. Figure 3.5 shows the normalized non-linear response of  $T_S$  to strain calculated by subtracting the linear response (i.e. subtracting  $\alpha\epsilon_{xx}$  and  $\tilde{\alpha}P$  from the data shown in Figs. 2(d) and 3(d) respectively, using the fitted values of  $\alpha$  and  $\tilde{\alpha}$ ). Data are shown as a function of the three (two) strain components present for the uniaxial stress (hydrostatic pressure) experiments on the bottom (top) axes. While quadratic responses to symmetric  $A_{1g,i}$  strain are allowed by symmetry, no such response is observed during our hydrostatic pressure experiment (cyan data points). Moreover,  $A_{1g}$  strains experienced in the hydrostatic pressure experiments exceed by nearly a factor of four those experienced by samples held under uniaxial stress. Hence, the quadratic response observed during our uniaxial stress experiment

<sup>3</sup>Error bars represent statistical uncertainty. A more comprehensive error analysis is given in Appendix 3.D

<sup>4</sup>The sign of  $\epsilon_{A_{1g},1}/\epsilon_{A_{1g},2}$  is expected to match the sign of  $\lambda_{(A_{1g},1)}/\lambda_{(A_{1g},2)}$  in case  $C_{A_{1g},1,1}, C_{A_{1g},2,2}, C_{A_{1g},1,2} > 0$ , where  $C_{A_{1g},i,j} = \frac{\partial^2 F}{\partial \epsilon_{A_{1g},i} \partial \epsilon_{A_{1g},j}}$ .

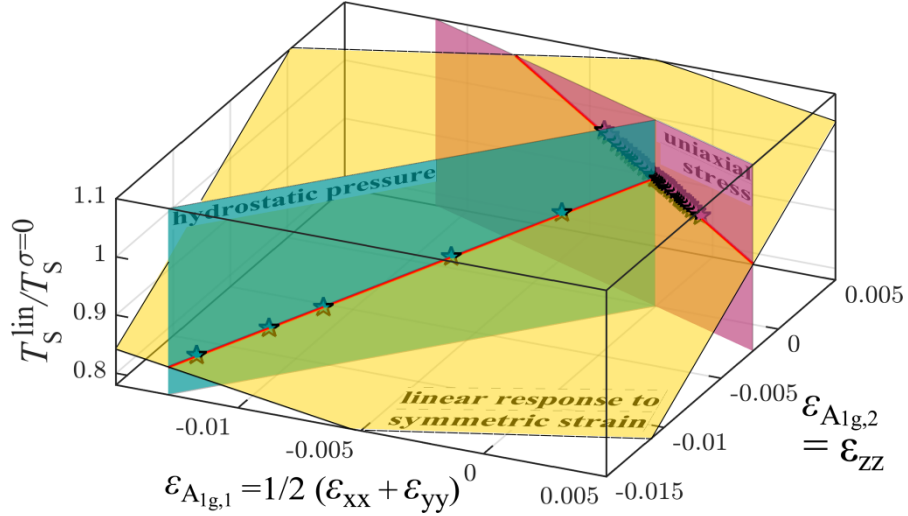


Figure 3.4: Normalized linear response of the structural transition to symmetric  $\epsilon_{A_{1g,1}}$ , and  $\epsilon_{A_{1g,2}}$  strain during hydrostatic pressure and uniaxial stress experiments. The cyan and purple vertical planes indicate the relative combination of symmetric strains induced during hydrostatic pressure and uniaxial stress experiments, respectively. Experimental data are shown by the cyan (hydrostatic pressure) and purple stars (uniaxial stress), respectively. Linear fits are shown by red lines. The yellow plane defined by these two lines describes the material’s linear response to symmetric strain.

(purple curve in Fig. 5) is caused exclusively by anti-symmetric  $B_{1g}$  strain. The fit parameters then yield  $\lambda_{(B_{1g},B_{1g})} = \partial^2 T_S / \partial \epsilon_{B_{1g}}^2 = -7.25 \pm 0.25 \text{ K}/\%^2$ .

The quadratic functional form of  $T_S(\epsilon_{B_{1g}})$  is understood based on symmetry, but the magnitude and sign of  $\lambda_{(B_{1g},B_{1g})}$  are not determined by symmetry alone. Our measurements reveal that the ratio  $\lambda_{(B_{1g},B_{1g})} / \lambda_{(A_{1g,i},A_{1g,i})}$  is at least 100, and possibly even larger<sup>5</sup>. The surprisingly large value of  $\lambda_{(B_{1g},B_{1g})}$  means that for tensile strains larger than  $\epsilon_{xx}^{\text{disp}} \approx 1.84\%$ ,  $\epsilon_{B_{1g}}$  strain dominates the suppression of  $T_S$ . The physical origin of this very large effect remains to be determined, but we emphasize one important difference between strains of these two symmetries. Specifically,  $A_{1g}$  strains do not break any symmetries (Fig. 3.1c(i)) and therefore do not introduce any new terms to the low-energy effective Hamiltonian describing the system. However,  $B_{1g}$  symmetry strain explicitly breaks specific symmetries (Fig. 3.1c(ii)) and therefore introduces new operators to the effective Hamiltonian. Acting on an  $E_g$  orbital doublet (for example, degenerate  $d_{xz}$  and  $d_{yz}$  orbitals), operators with  $B_{1g}$  and  $B_{2g}$  symmetry do not commute; consequently  $B_{1g}$  symmetry strain induces quantum fluctuations in a  $B_{2g}$  symmetry order parameter [53], possibly accounting for (or at least

<sup>5</sup>Quadratic fits to the hydrostatic pressure data yield  $\lambda_{(A_{1g,1},A_{1g,1})} = 0.06 \pm 0.07 \text{ K}/\%^2$  and  $\lambda_{(A_{1g,2},A_{1g,2})} = 0.05 \pm 0.05 \text{ K}/\%^2$ . The quadratic response of  $T_S$  to  $\epsilon_{B_{1g}}$  is thus found to be at least two orders of magnitude larger. Since the uncertainty in  $\lambda_{(A_{1g,i},A_{1g,i})}$  ( $i = 1, 2$ ) is so large, this is essentially a lower bound on the ratios  $\lambda_{(B_{1g},B_{1g})} / \lambda_{(A_{1g,i},A_{1g,i})}$ , which could therefore be considerably larger.

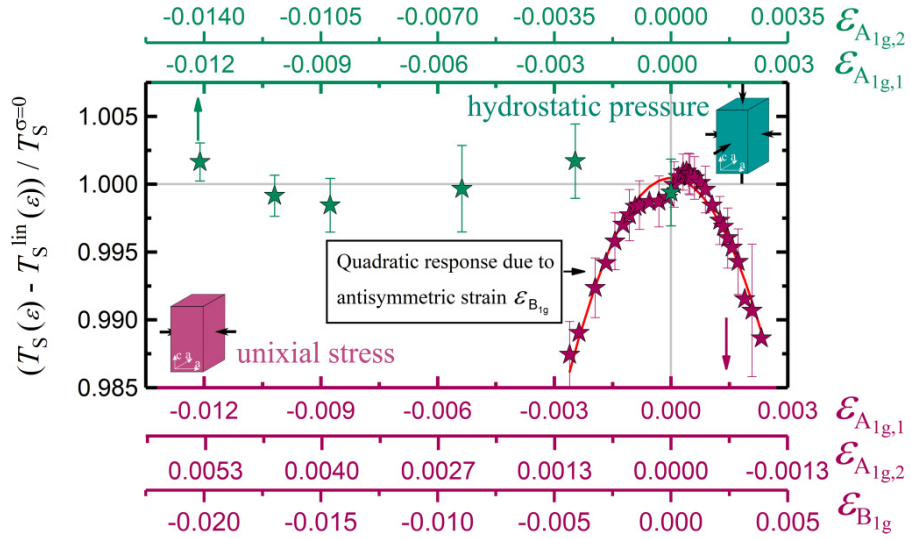


Figure 3.5: Normalized non linear response of the coupled nematic/structural transition temperature to strain during hydrostatic (cyan stars, top axes) and uniaxial stress (purple stars, bottom axes) experiments. The quadratic contribution evident in the uniaxial stress data is solely due to antisymmetric  $B_{1g}$  strain. Red line shows fit to a quadratic function. The origin of the kink near zero strain is currently unknown. The feature is, however, smaller than the error bars and has no statistically significant impact on the fit .

contributing to) the large negative value of  $\lambda_{(B_{1g}, B_{1g})}$ .

On a phenomenological level, we note that the negative sign of  $\lambda_{(B_{1g}, B_{1g})}$  for  $\text{Ba}(\text{Fe}_{0.975}\text{Co}_{0.025})_2\text{As}_2$  is entirely consistent with observations that the  $B_{1g}$  component of the elastic tensor,  $\frac{1}{2}(c_{11} - c_{12})$  hardens upon cooling through  $T_S$  [92]. This can be readily appreciated by turning to the standard Landau treatment of the nematic phase transition [17]. Writing the free energy in even powers of the nematic order parameter and including coupling to strains  $\epsilon_{A_{1g},1}$ ,  $\epsilon_{A_{1g},2}$ ,  $\epsilon_{B_{1g}}$ , and  $\epsilon_{B_{2g}}$  we obtain

$$\begin{aligned} \Delta F = & \frac{a}{2}(T - T^*)\Phi_{B_{2g}}^2 + \frac{b}{4}\Phi_{B_{2g}}^4 + \lambda_{B_{2g}}\epsilon_{B_{2g}}\Phi_{B_{2g}} - \\ & - \frac{a}{2}\lambda_{B_{1g}}\epsilon_{B_{1g}}^2\Phi_{B_{2g}}^2 - \frac{a}{2}\lambda_{A_{1g}}\epsilon_{A_{1g}}^{\text{eff}}\Phi_{B_{2g}}^2 + \frac{1}{2}C_{66}^{(0)}\epsilon_{B_{2g}}^2 + \\ & + \frac{1}{2}\left(\frac{C_{11} - C_{12}}{2}\right)^{(0)}\epsilon_{B_{1g}}^2 + \frac{1}{2}C_{A_{1g}}^{\text{eff}}\left(\epsilon_{A_{1g}}^{\text{eff}}\right)^2, \end{aligned} \quad (3.2)$$

where  $\Phi_{B_{2g}}$  is the nematic order parameter, the coupling coefficients  $\lambda_{B_{1g}}$ ,  $\lambda_{A_{1g},1}$  and  $\lambda_{A_{1g},2}$  are determined by our measurements, and  $\epsilon_{A_{1g}}^{\text{eff}}$  and  $C_{A_{1g}}^{\text{eff}}$  are appropriate combinations of  $A_{1g}$  symmetry strains and terms in the elastic stiffness tensor, determined by the Poisson ratio of the material. Significantly, the biquadratic coupling of  $\Phi_{B_{2g}}$  to  $\epsilon_{B_{1g}}$  not only provides means to tune  $T_S$ , but also renormalizes the bare elastic modulus  $C_{B_{1g}} = \left(\frac{C_{11} - C_{12}}{2}\right)^{(0)}$  for free-standing samples, such that

$$C_{B_{1g}}^{\text{eff}} = \frac{\partial^2 F}{\partial \epsilon_{B_{1g}}^2} = \left(\frac{C_{11} - C_{12}}{2}\right)^{(0)} - a\lambda_{B_{1g}}\Phi_{B_{2g}}^2. \quad (3.3)$$

In other words, since  $a > 0$  our observation of a negative value of  $\lambda_{B_{1g}} = -7.25 \pm 0.25 \frac{\text{K}}{\%}$  is consistent with observations that the  $B_{1g}$  component of the elastic tensor,  $\frac{C_{11} - C_{12}}{2}$  hardens [92] upon cooling through  $T_S$ .

### 3.4 Summary

In-plane strain has previously been demonstrated as suitable means to induce phase transitions [94]. Here we have shown how a complete symmetry decomposition, made possible by comparison to hydrostatic pressure, reveals the separate effects of symmetric and antisymmetric strains that are necessarily both present when a sample is held under in-plane uniaxial stress. We emphasize that anti-symmetric strain is a powerful continuous tuning parameter for nematic phase transitions. While values of  $\epsilon_{B_{1g}}$  that would be necessary to completely suppress the coupled nematic/structural phase transition in  $\text{Ba}(\text{Fe}_{0.975}\text{Co}_{0.025})_2\text{As}_2$  are slightly out of reach, this is not necessarily the case for other materials, raising the distinct possibility that antisymmetric strain could be used to continuously tune a suitable material to a nematic quantum phase transition [53]. Finally, we report that symmetric c-axis strain has a significantly stronger effect on the nematic

transition in  $\text{Ba}(\text{Fe}_{0.975}\text{Co}_{0.025})_2\text{As}_2$  as compared to symmetric in-plane strain.

### 3.A Sample preparation

The  $\text{Ba}(\text{Fe}_{0.975}\text{Co}_{0.025})_2\text{As}_2$  single crystals characterized here were grown using a FeAs self flux technique described elsewhere [7]. The crystals were cleaved into thin plates and cut into rectilinear bars. Typical samples dimensions for uniaxial stress and hydrostatic pressure experiments were  $2000 \times 400 \times 35 \mu\text{m}$  and  $1000 \times 300 \times 35 \mu\text{m}$ , respectively. Electrical contacts were made by a reflow soldering technique using a Sn63Pb37 solder paste with a solder particle size of 15-25  $\mu\text{m}$  (Chip Quick SMD291AX10T5). The initial steps of the contacting procedure using solder paste are similar to contacting methods using silver paint or silver epoxy. The ends of short ( $\sim 10$  mm) pieces of 25  $\mu\text{m}$  wide gold wire were dipped into the solder paste and positioned onto the freshly cleaved sample surface. The sample, resting on a 1 mm thick glass slide, is then placed on a hot plate preheated to 200 °C to reflow the solder beads. To prevent oxidation of the contacts, the sample and glass slide are taken off the hot plate as soon as the solder particles melt. This can be easily seen as the contact appearance changes from matte to shiny. The typical contact resistance of such solder joints was estimated by a quasi 4 point measurement to be smaller than 20 mOhm per contact. While the contact resistance of soldered contacts is superior to silver paint and silver epoxy, it is important to note that the superconductivity of the solder ( $T_c \sim 7.1$  K) [95] might be problematic for measurements at low temperatures. These solder joints are also significantly more mechanically robust and are better able to survive thermal cycling than silver paint contacts.

### 3.B Experimental Methods

Four point resistivity measurements during our uniaxial stress and hydrostatic pressure experiments were performed using a Stanford Research Lock In amplifier (SR830). The output of the lock-in amplifier was converted to a constant current source using a 1 kOhm series resistor. The voltage signal was amplified with a Stanford Research transformer preamplifier (SR554).

All resistivity measurements used the same cryostat, a PPMS from Quantum Design. The temperature was swept slowly at a rate of 0.5K/min. The sample temperature was measured using a Cernox CX-1050 temperature sensor from Lakeshore mounted on the Ti body of the CS100 cell (for uniaxial stress experiments) and the Cu-Be body of the hydrostatic pressure cell, respectively. The temperature sensors were sampled using a Lakeshore 340 temperature controller. The thermal lag of the sample as compared to the measured cell temperature was estimated by taking resistivity measurements during cooling and warming runs. Thermal lags of about 0.1 K and 0.25 K were found for our uniaxial stress and hydrostatic pressure experiments, respectively.

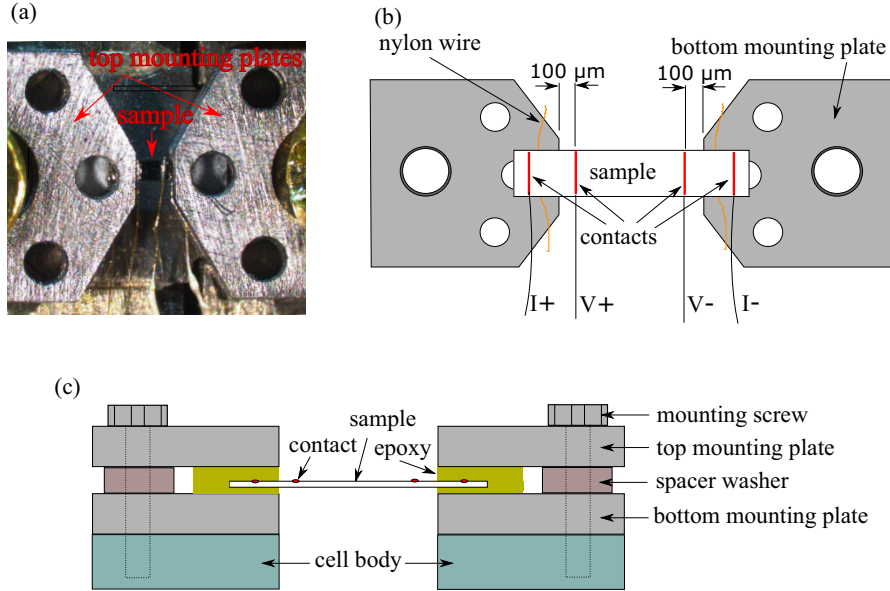


Figure 3.6: (a)  $\text{Ba}(\text{Fe}_{0.92}\text{Co}_{0.08})_2\text{As}_2$  crystal mounted on a Razorbill CS100 cell using bottom and top mounting plates. Panel (b) sketches a sample mounted onto bottom mounting plates, panel (c) sketches a cross sectional view.

### 3.B.1 Uniaxial stress experiments

Uniaxial stress experiments were performed using a commercially available CS100 cell from Razorbill Instruments. This cell uses piezo electric (PZT) stacks to separate two mounting plates. The exact working principle of such a cell is described in detail elsewhere [64]. Samples were affixed onto the mounting plates of the uniaxial stress cell (see Figure 3.6) using Devcon 2-ton epoxy. The glue layer thickness between the sample and the bottom mounting plates was controlled using Nylon wire spacer with a diameter of  $25\ \mu\text{m}$ . The glue layer thickness between the sample and the top mounting plates was controlled by the thickness of spacer washers between the top and bottom mounting plates. Typically, the glue layer on top of the sample was approximately double the thickness of the bottom glue layer.

The zero-volt strain (zero volts across the PZT stacks results in zero piezoelectric extension or contraction of the stacks) experienced by the sample during uniaxial stress experiments is determined by the differential thermal expansion of the sample and the sample mounting plates and thus, in general, is not temperature independent. In this case however, the thermal expansion of the Ti mounting plates and the in-plane expansion of  $\text{Ba}(\text{Fe}_{0.92}\text{Co}_{0.08})_2\text{As}_2$  are very similar (Fig. 3.7). Therefore we can approximate the strain as independent of temperature and fully controlled by the voltages applied to the Piezo electric stacks. Due to the hysteresis of the PZT stacks, zero volts across all three PZT stacks does not necessarily correspond to zero strain.

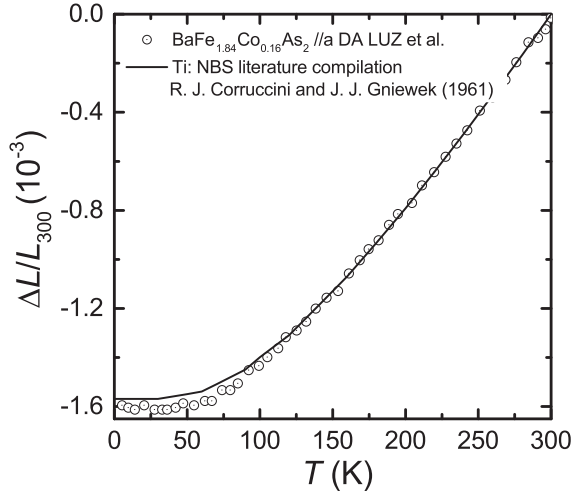


Figure 3.7: Comparison of the in-plane thermal expansion of  $\text{Ba}(\text{Fe}_{0.92}\text{Co}_{0.08})_2\text{As}_2$  [91] and the thermal expansion of Ti. [96]

The nominal strain along the transport direction ( $\epsilon_{xx}^{disp}$ ) was determined by measuring the displacement of the two sides of the cell (using a capacitive displacement sensor sampled by an Andeen Hagerling AH2550 capacitance bridge) with respect to the initial distance between the lower sample mounting plates. Since the zero-volt distance of the capacitor plates is not independent of temperature (due to the thermal expansion of the epoxy holding these plates), first a calibration of the zero volt capacitance has to be determined as function of temperature. Ideally, this is done by affixing a relatively stiff bar of titanium (to match the thermal expansion of the cell made of titanium) across the two sides of the cell and measuring the capacitance as a function of temperature. Since the zero volt capacitance changes between each measurement run due to the hysteresis of the PZT stacks, it is important to record this value before the mounting procedure of each sample. The calibration can then be adjusted from measurement to measurement. The change of the capacitance with changing distance of the capacitor plates, on the other hand is almost temperature independent (the thermal contraction of the plates as well as the change of the dielectric permittivity of helium gas within the experimental temperature range are small). The manufacturer supplied calibration is thus almost temperature independent.

Due to strain relaxation effects within the glue layers and the Ti mounting plates, the actual strain on the sample differs from the nominal value. In this work, we estimated the strain relaxation effects using finite element simulations (more details given below). The strain experienced by the sample was calculated to be  $\epsilon_{xx} = (0.7 \pm 0.07)\epsilon_{xx}^{disp}$ . The difference in strain on the top and bottom surface of the sample was found to be less than 2%, despite the asymmetric glue layer thicknesses. The normal strains within the sample were found to be approximately constant in distances over  $100 \mu\text{m}$  of the plates. The voltage contacts on our samples were placed so that only the section of the

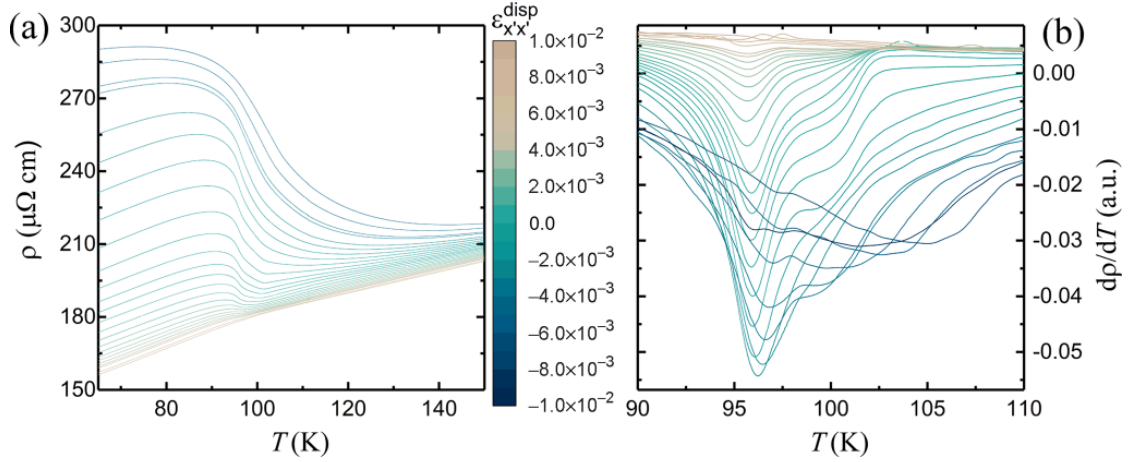


Figure 3.8: (a) Resistivity as a function of temperature for different strains  $\epsilon_{xx}^{disp}$ , applied along the tetragonal [110] axis. (b) Derivative of the electrical resistivity with respect to temperature. The step like feature associated with the structural phase transition is suppressed quickly and is fully smeared for strains on the order of  $\epsilon_{xx}^{disp} \approx 3 \times 10^{-3}$ .

sample experiencing uniform strain was probed. To avoid shear strains introduced into the sample by asymmetric, point shaped contacts, the voltage (and the current) contacts were line shaped and spanned the entire width of the sample (see Fig. 6b).

### Uniaxial stress along the tetragonal [110] axis

$B_{2g}$  strain is known to turn the phase transition into a cross over and smear all the related features. This is indeed what we observe in our experiment applying uniaxial stress along the tetragonal [110] axis. Figure 3.8 shows the data for the  $B_{2g}$  strain experiment. The feature corresponding to the nematic phase transition (step change in the derivative of the resistivity with respect to temperature) is quickly suppressed and replaced by a broad cross over. A relatively small strain  $\epsilon_{xx}^{disp}$  of about  $3 \times 10^{-3}$  is sufficient to fully suppress the feature associated with the nematic phase transition. Considering the evolution of the feature of the nematic phase transition in our  $B_{1g}$  data presented in the manuscript, (and the rotated compliance tensor), we estimate a misalignment of  $2.25^\circ$ . As the feature associated with the nematic phase transition stays sharp and clearly observable within the whole investigated strain range, the contamination (which to some extent might also originate from our voltage contacts) has no significance for our results.

### 3.B.2 Hydrostatic pressure experiments

Hydrostatic pressure experiments were performed using a Quantum Design HPC-30 Cu-Be based self-clamping pressure cell. Although this version is no longer commercially available, information

on the very similar updated version, HPC-33, can be found on the Quantum Design website. Hydrostatic pressure up to  $\sim 3$  GPa is applied using a hydraulic press. Daphne Oil 7373 is used as a pressure transfer medium. Note that the freezing point of the Daphne oil is always below room temperature for pressures less than 2 GPa. This ensures a high degree of hydrostaticity throughout the experimental range [66]. Pressure measurements were performed by probing the superconducting transition temperature of a lead manometer [67]. In addition, the temperature dependence of the hydrostatic pressure within the HPC-30 pressure cell was determined by calibration measurements using both, a lead and a manganin manometer [97]. Below 100 K the hydrostatic pressure was found to be almost independent of temperature.

### 3.C Finite element simulations

The goal of our finite element simulation was to estimate the strain relaxation effects in the glue layers as well as the Ti mounting plates. The mechanical properties used within our simulations are summarized in Tab. 3.1 below.

Table 3.1: Summary of the mechanical properties used for our finite element simulations. For the tetragonal  $\text{Ba}(\text{Fe}_{0.975}\text{Co}_{0.025})_2\text{As}_2$ , the Young's modulus is given for stress along [100] ( $E$ ) and [001] ( $E'$ ). In addition, the table also shows the in-plane ( $\nu$ ) and out-of-plane Poisson ratio ( $\nu'$ ), as well as the in-plane ( $C_{66}$ ) and out-of plane shear moduli ( $C_{44}$ ). These properties correspond to the mechanical properties of  $\text{Ba}(\text{Fe}_{0.963}\text{Co}_{0.0375})_2\text{As}_2$  at 100 K, as found by resonant ultrasound spectroscopy [92]. The mechanical properties of the mounting epoxy (Devcon 2-ton epoxy) at 100 K were assumed to be slightly softer compared to filled Stycast 2850FT [64].

Material	$E$ (GPa)	$E'$ (GPa)	$C_{66}$ (GPa)	$C_{44}$ (GPa)	$\nu$	$\nu'$
Titanium grade2	105	-	39.5	-	0.33	-
Epoxy	10	-	3.8	-	0.3	-
$\text{Ba}(\text{Fe}_{0.975}\text{Co}_{0.025})_2\text{As}_2$	82	82	10	39	0.26	0.164

The elastic properties of  $\text{Ba}(\text{Fe}_{0.975}\text{Co}_{0.025})_2\text{As}_2$  were estimated using the elastic stiffness tensor for 3.7% Co doped  $\text{BaFe}_2\text{As}_2$  at 100 K [92]. The mechanical properties of the epoxy were estimated to lie in between the properties of filled Stycast 2850FT and unfilled Stycast 1260 [64]. To our knowledge, the actual mechanical properties of Devcon two-ton epoxy are not characterized down to 100 K. To justify the assumed mechanical properties we compared measurements on samples mounted using Devcon two-ton epoxy to measurements using Stycast 2850FT. Judged from the strain dependence of the structural and magnetic transition temperature of  $\text{Ba}(\text{Fe}_{0.975}\text{Co}_{0.025})_2\text{As}_2$ , Devcon two-ton epoxy yields only a moderately smaller strain transmission as compared to Stycast 2850FT. Since the exact mechanical properties are unknown, we estimated the associated systematic error by varying the mechanical properties used within our finite element simulations by  $\pm 50\%$ .

In order to minimize the computational requirements, the model shown in Fig. 3.9 was cut along mirror planes such that effectively only 25% of the model had to be meshed and simulated. The model

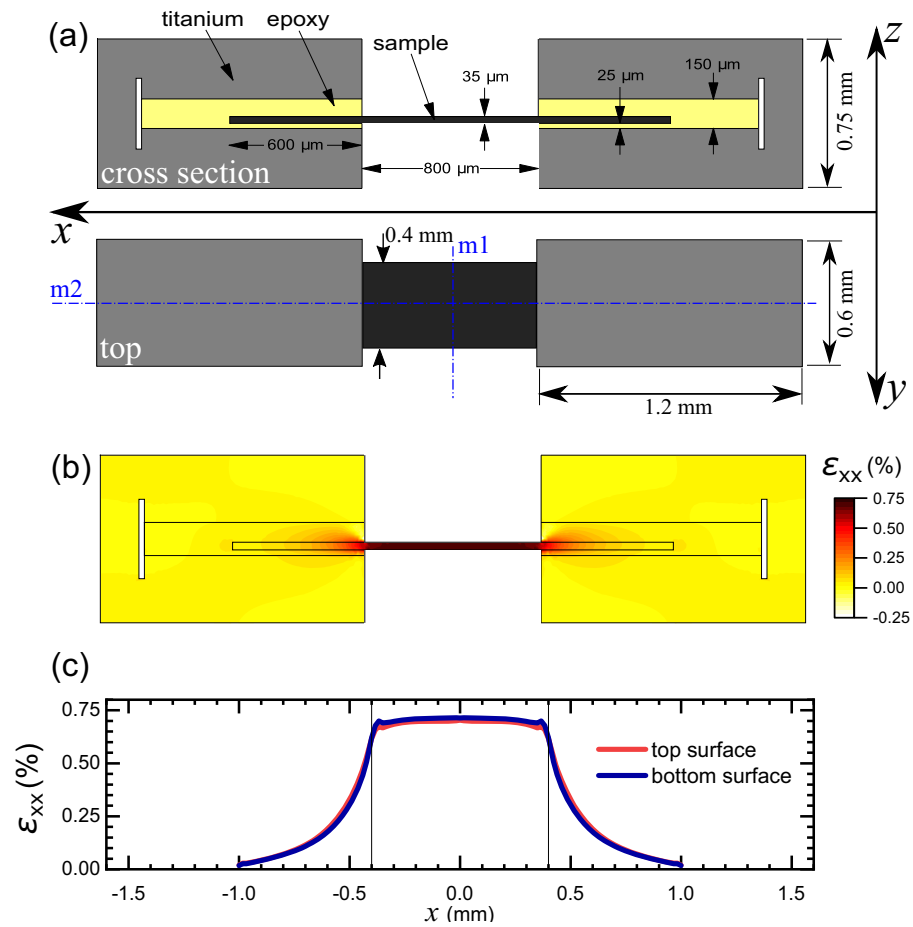


Figure 3.9: (a) Model used for the finite element simulations presented here. The dashed-dotted blue lines on the top view show the mirror planes  $m_1$  and  $m_2$  used to reduce the model size. (b) Results of our finite element simulation shown on the cross section of our model. (c) Normal strain  $\epsilon_{xx}$  along the center line in  $x$  direction on the top and bottom surface of the sample. The vertical black solid lines mark the position of the mounting plate edges. Nominally, a strain of  $\epsilon_{xx}=1\%$  was applied. The strain relaxation within the mounting plates and the glue result in a strain transfer ratio of 0.7.

has been constrained such that the mounting plates were free to move only along a path parallel to  $x$ . A symmetric displacement corresponding to a reduction in the distance of the mounting plates by  $8\ \mu\text{m}$  (corresponding to a nominal  $\epsilon_{xx}^{\text{disp}}$  of 1%) was applied. For meshing, brick shaped elements were chosen. The element size was set to be  $15\ \mu\text{m}$ . The contacts between the sample and the epoxy as well as the epoxy and the mounting plates were chosen to be perfectly rigid.

The strain within the sample along  $x$  was found to be nearly constant  $100\ \mu\text{m}$  away from the mounting plate edges. As can be seen from the results shown in Fig. 9, out of plane shear strain (introduced by the asymmetric glue layer thickness on top and bottom) is small, resulting in a difference of  $\epsilon_{xx}$  on the top and bottom surface of the sample of only about 2% (Fig. 3.9(c)). The strain transfer ratio  $\epsilon_{xx}/\epsilon_{xx}^{\text{disp}}$  used for analyzing our data was found to be  $0.7 \pm 0.07$ . The error bar was estimated from varying the mechanical properties of the epoxy within  $\pm 50\%$  as well as the thickness of the bottom glue layer by  $\pm 15\ \mu\text{m}$ .

### 3.C.1 Elastic properties of $\text{Ba}(\text{Fe}_{0.975}\text{Co}_{0.025})_2\text{As}_2$

Since we focus on vertical shear-free deformations (as indicated by our finite element simulations), the elastic constants  $C_{ij}$  with  $i, j \leq 3$  (Voigt notation:  $1 \equiv xx, 2 \equiv yy, 3 \equiv zz$ ) fully describe the stress-strain relations relevant for our experiments. Out of the four independent elastic constants<sup>6</sup>,  $C_{11}$ ,  $C_{12}$ , and  $C_{33}$  have recently been reported by a resonant ultrasound spectroscopy (RUS) study [92] for 3.7% Co doped  $\text{BaFe}_2\text{As}_2$  as a function of temperature. We here determine the missing  $C_{13}$  by assuming an equal in- and out-of-plane Young's modulus (as suggested by a recent instrumented indentation experiment [98]) and arrive at

$$\mathbf{C} = \begin{pmatrix} 92.5 & 27.3 & 19.7 \\ 27.3 & 92.5 & 19.7 \\ 19.7 & 19.7 & 88.3 \end{pmatrix} \text{ GPa}$$

for 3.7% Co doped  $\text{BaFe}_2\text{As}_2$  at 100 K. Using this tensor as an estimation for the shear-free mechanical properties of 2.5% Co doped  $\text{BaFe}_2\text{As}_2$  in the vicinity of its structural transition, it is straightforward to calculate the symmetry decomposed strain fields from the measured hydrostatic pressure and  $\epsilon_{xx}$  for the two sets of experiments.

## 3.D Strain decomposition

The relation between  $\epsilon_{A_{1g,1}} = 1/2(\epsilon_{xx} + \epsilon_{yy})$  and  $\epsilon_{A_{1g,2}} = \epsilon_{zz}$  under the two stress conditions studied here is determined by the elastic properties (the elastic stiffness tensor) of the investigated material.

---

<sup>6</sup> $C_{ij} = C_{ji}$  due to the symmetry of the free energy derivatives  $\frac{\partial}{\partial \epsilon_i} \left( \frac{\partial F}{\partial \epsilon_j} \right) = C_{ij}$ , and  $C_{11} = C_{22}$  due to crystal symmetry

For hydrostatic pressure ( $\sigma_{xx} = \sigma_{yy} = \sigma_{zz}$ ),  $\epsilon_{A_{1g,2}} = \frac{1-2\nu'}{1-\nu-\nu'}\epsilon_{A_{1g,1}}$ , for uniaxial stress ( $\sigma_{xx} \neq 0, \sigma_{yy} = \sigma_{zz}=0$ ),  $\epsilon_{A_{1g,2}} = \frac{-2\nu'}{1-\nu}\epsilon_{A_{1g,1}}$ , where  $\nu$  and  $\nu'$  are the in- and out-of-plane Poisson ratio.

Using these relations the total response of  $T_S$  to  $\epsilon_{A_{1g,1}}$  can be written as

$$\begin{aligned} \left( \frac{dT_S}{d\epsilon_{A_{1g,1}}} \right)^{\text{hyd}} &= \frac{\partial T_S}{\partial \epsilon_{A_{1g,1}}} + \frac{1-2\nu'}{1-\nu-\nu'} \frac{\partial T_S}{\partial \epsilon_{A_{1g,2}}} \\ \left( \frac{dT_S}{d\epsilon_{A_{1g,1}}} \right)^{\text{uni}} &= \frac{\partial T_S}{\partial \epsilon_{A_{1g,1}}} - \frac{2\nu'}{1-\nu} \frac{\partial T_S}{\partial \epsilon_{A_{1g,2}}} \end{aligned} \quad (3.4)$$

for the hydrostatic pressure and the uniaxial stress experiment, respectively. Using the in- and out-of-plane Poisson ratio determined from the elastic stiffness tensor  $\mathbf{C}$  ( $\nu = 0.26$  and  $\nu' = 0.164$ ) as well as the experimentally determined responses  $\left( \frac{dT_S}{d\epsilon_{A_{1g,1}}} \right)^{\text{hyd}}$  and  $\left( \frac{dT_S}{d\epsilon_{A_{1g,1}}} \right)^{\text{uni}}$ , the above equations can be solved for  $\frac{\partial T_S}{\partial \epsilon_{A_{1g,i}}}$ . We find  $\frac{\partial T_S}{\partial \epsilon_{A_{1g,1}}} = -6.35 \frac{\text{K}}{\%}$  and  $\frac{\partial T_S}{\partial \epsilon_{A_{1g,2}}} = +16.7 \frac{\text{K}}{\%}$  for the investigated  $\text{Ba}(\text{Fe}_{0.975}\text{Co}_{0.025})_2\text{As}_2$  confirming the largest linear contribution comes from  $\epsilon_{A_{1g,2}}$ .

Errors reported in the paper represent statistical uncertainty. A full error analysis considering also systematic uncertainty yields,  $\frac{\partial T_S}{\partial \epsilon_{A_{1g,1}}} = -6.35 \pm (0.23 \frac{\text{K}}{\%})^{\text{statistical}} \pm (2.28 \frac{\text{K}}{\%})^{\text{systematic}}$  and  $\frac{\partial T_S}{\partial \epsilon_{A_{1g,2}}} = 16.7 \pm (0.32 \frac{\text{K}}{\%})^{\text{statistical}} \pm (1.45 \frac{\text{K}}{\%})^{\text{systematic}}$ . The main systematic errors considered are a 5% uncertainty in the elastic constants as well as the measured hydrostatic pressure, and a 10% uncertainty in the strain relaxation factor. All errors were assumed to be uncorrelated. As the sign of our measured responses is robust within the error bars, our main results and discussion are unaffected by the systematic errors mentioned here.

## Chapter 4

# Nematic Quantum Criticality Revealed by Strain Tuning

In this chapter, the strain-tuning technique established in the previous chapter is utilized to systematically study the effect of  $A_{1g}$  and  $B_{1g}$  strains on the critical temperature of the coupled nematic/structural phase transition  $T_S$  in  $\text{Ba}(\text{Fe}_{1-x}\text{Co}_x)_2\text{As}_2$  for various cobalt concentrations,  $x$ . A power-law behavior of the critical temperature is observed as a function of a linear combination of the tuning parameters,  $\epsilon_{A_{1g}}$ ,  $\epsilon_{B_{1g}}$ , and  $x$ , providing a direct evidence for nematic quantum criticality in a representative material of iron-based superconductor family. Results from this chapter are published in [72]. The figures are reproduced and the text is taken nearly verbatim from the reference with the permission of the American Association for the Advancement of Science.

### 4.1 Introduction

Long range electronic nematic order, defined as electronic order that only breaks point group symmetries, is a ubiquitous feature of iron-based superconductors (see for example references [74, 6] and references therein). For cuprate superconductors, mounting evidence points towards a generic in-plane electronic anisotropy for underdoped compositions, implying the presence of at least a nematic component to an electronic ordered state, and possibly even a vestigial nematic state (see for example references [99, 100] and references therein). From a theoretical perspective, several lines of reasoning suggest that nematic fluctuations can provide a pairing interaction [42, 43, 44], and hence suggest that the presence of nematic order in the phase diagrams of these high temperature superconductors may not be coincidental. In particular, nematic fluctuations enhance superconductivity in any symmetry channel [45], and hence could be a key element for increasing the critical temperature even when the dominant pairing interaction arises from spin fluctuations. A key open

question is whether *quantum critical* nematic fluctuations are present, and if so over how much of the phase diagram. Here, we directly address this latter question for a representative family of Fe-based superconductors, revealing the presence of quantum critical nematic fluctuations by power-law variation of the critical temperature of the nematic phase transition with respect to non-thermal tuning parameters.

Direct evidence for a quantum critical regime in the Fe-based superconductors has been limited thus far. A divergence of the effective mass in  $\text{BaFe}_2(\text{As}_{1-x}\text{P}_x)_2$  has been inferred from penetration depth, quantum oscillation, heat capacity, and resistivity measurements [101, 102, 48, 15, 2], suggesting the presence of a quantum critical point. These measurements cannot, however, establish the character of the fluctuating order, in particular whether it is nematic or magnetic. In comparison, nuclear magnetic resonance measurements in  $\text{NaFe}_{1-x}\text{Co}_x\text{As}$  indicate the possible presence of well-separated magnetic and nematic quantum critical points in that system [103]. Measurements of the doping and temperature dependence of the nematic susceptibility for a wide variety of Fe-based superconductors, obtained via elastoresistivity [17, 47], elastic constant measurements [32], Raman scattering [33, 34, 35], and nuclear magnetic resonance [50], reveal the presence of strong nematic fluctuations and thus are suggestive of the presence of a nematic quantum critical point beneath the superconducting ‘dome’ in all of these materials. Recent elastoresistivity measurements in  $\text{Ba}(\text{Fe}_{1-x}\text{Co}_x)_2\text{As}_2$  for a fine comb of overdoped compositions approaching the critical doping ( $x_c$ ) are consistent with a power-law divergence of the nematic susceptibility with respect to  $(x - x_c)$ ; however, the temperature dependence is not currently understood in detail, and hence the regime over which quantum critical fluctuations extends is unknown [104].

Attempts to observe power-law behavior in thermodynamic quantities as a response to non-thermal tuning parameters upon approaching the putative QCP face daunting challenges. These challenges are associated either with difficulties in accurately determining the magnitude of the tuning parameters as the material is tuned infinitesimally close to the putative QCP (which is the case for chemical substitution) or in obtaining sufficient fine-tuning of the tuning parameter in that regime (which can be the case for hydrostatic pressure, another common tuning parameter). Here we bypass these difficulties by using symmetric strain ( $\epsilon_{A_{1g}}$ ) and orthogonal antisymmetric strain ( $\epsilon_{B_{1g}}$ ) induced by in-plane uniaxial stress as essentially-continuously-variable tuning parameters. By doing so, we are able to show for underdoped compositions of the representative Fe-based superconductors  $\text{Ba}(\text{Fe}_{1-x}\text{Co}_x)_2\text{As}_2$  that a single power law governs the variation rate of the critical temperature of the coupled nematic/structural phase transition ( $T_S$ ) with respect to *both* of these symmetry-inequivalent tuning parameters. This provides direct evidence of quantum critical power-law behavior in this representative material. Moreover, the perspective is widely applicable with a variety of tuning parameters and phase transitions, assuming the condition of uniform tuning parameter is achievable, establishing a useful framework to observe quantum criticality in other materials in this class and beyond.

Strain induced by external stresses breaks only point symmetries and consequently has a special role to play in the study of electronic nematicity. In recent years, considerable progress has been made by exploiting the fact that strain with the same symmetry as the nematic order acts as an effective conjugate field because of the bilinear coupling between the strain and the nematic order parameter [17, 55, 18]. Here, we explore how strains of different symmetries couple to Ising nematic order and determine the shape of the phase boundary in temperature-strain space. These ideas are not specific to nematicity because they do not rely on bilinear coupling, and they could be applied to an even wider set of strain-tuned phase transitions.

## 4.2 Effect of Strain of Differing Symmetry to the Critical Temperature $T_S$

The representative materials,  $\text{Ba}(\text{Fe}_{1-x}\text{Co}_x)_2\text{As}_2$ , belong to the  $D_{4h}$  point group (corresponding to the tetragonal system) and undergo a phase transition to an electronic nematic state with  $B_{2g}$  symmetry. Because the coupling between the electronic and lattice degrees of freedom, the phase is also characterized by a spontaneous  $B_{2g}$  strain,  $\epsilon_{B_{2g}} \equiv \epsilon_{xy}$ . We consider the effects of strains belonging to two other irreducible representations of the point group, namely the symmetry preserving strain  $\epsilon_{A_{1g}}$ , and the *orthogonal* antisymmetric strain  $\epsilon_{B_{1g}}$  (fig.4.1A center and right panels). Here  $\epsilon_{A_{1g}}$  is a combination of in-plane ( $\epsilon_{A_{1g,1}} \equiv (\epsilon_{xx} + \epsilon_{yy})/2$ ) and out-of-plane ( $\epsilon_{A_{1g,2}} \equiv \epsilon_{zz}$ ) symmetric strains, and  $\epsilon_{B_{1g}}$  is defined as  $\epsilon_{B_{1g}} \equiv (\epsilon_{xx} - \epsilon_{yy})/2$ . Note here that the coordinates are defined in the two-iron unit cell, i.e.  $\epsilon_{xx}$  and  $\epsilon_{xy}$  are the deformation along Fe-As bond and Fe-Fe bond, corresponding to [100] and [110] crystallographic directions respectively. The tuning effect of  $A_{1g}$  and  $B_{1g}$  strains are different, as has been shown previously [65]. In the small strain regime (which applies to this work),  $A_{1g}$  strain tunes the critical temperature  $T_S$  linearly to leading order. The orthogonal antisymmetric strain  $\epsilon_{B_{1g}}$ , however, can vary the critical temperature  $T_S$  only quadratically to leading order; linear variation with respect to  $\epsilon_{B_{1g}}$  is prohibited by symmetry [105]. Therefore, up to quadratic order, the variation of the critical temperature  $T_S$  in the presence of  $\epsilon_{A_{1g}}$  and  $\epsilon_{B_{1g}}$  strains is as follow:

$$T_S(\epsilon_{A_{1g}}, \epsilon_{B_{1g}}) = T_0 + a\epsilon_{A_{1g}} + a'\epsilon_{A_{1g}}^2 + b\epsilon_{B_{1g}}^2 \quad (4.1)$$

where  $T_0 \equiv T_S(0,0)$  is the free standing critical temperature, and  $a$ ,  $a'$  and  $b$  are coefficients to be determined. Of particular relevance to the present work, measurements performed under hydrostatic pressure conditions reveal that the coefficient  $a$  is negligibly small for all compositions studied (Fig. 4.2). Hence, the tuning effect of  $\epsilon_{A_{1g}}$  and  $\epsilon_{B_{1g}}$  can be unambiguously disentangled, even in the presence of both symmetry strains. Because the  $A_{1g}$  and  $B_{1g}$  strains belong to different irreducible representations, the coefficients  $a$  and  $b$  are ordinarily anticipated to be completely independent - i.e. unrelated by any symmetry operations. As we will demonstrate below, this is no longer the case

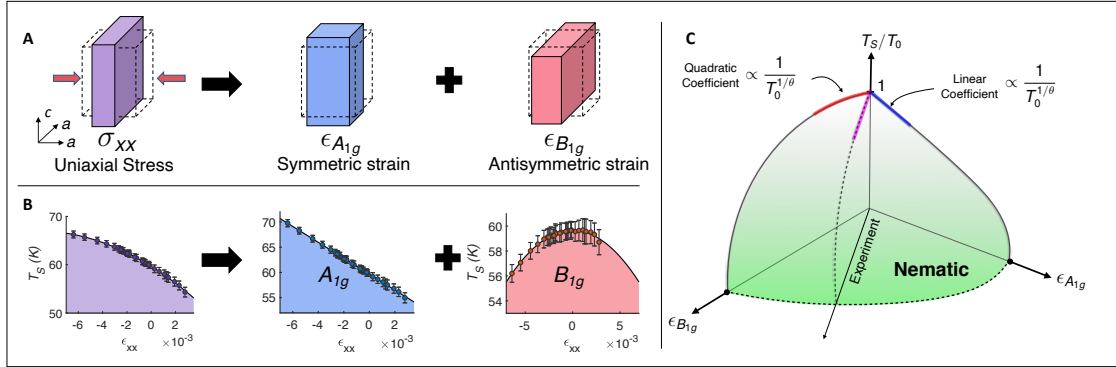


Figure 4.1: **Consequences of uniaxial stress along [100]** (A) In a tetragonal system, deformation caused by the uniaxial stress applied along [100] direction can be expressed as the combination of the symmetry preserving strain  $\epsilon_{A_{1g}}$ , and orthogonal antisymmetric strain  $\epsilon_{B_{1g}}$ . The ratio of these strain components depends on the elastic moduli of the material. Note that orthogonal antisymmetric  $B_{1g}$  strain is defined as  $\epsilon_{B_{1g}} = (\epsilon_{xx} - \epsilon_{yy})/2$ , while symmetry preserving  $A_{1g}$  strain in this scenario is a combination of the in-plane  $\epsilon_{A_{1g,1}} = (\epsilon_{xx} - \epsilon_{yy})/2$ , and out of plane  $\epsilon_{A_{1g,2}} = \epsilon_{zz}$ . Dashed lines indicate the undeformed tetragonal unit cell. (B) The variation of coupled nematic/structural phase transition temperature as a function of the measured strain along [100],  $\epsilon_{xx}$ , for a representative sample with cobalt concentration  $x = 4.8\% \pm 0.2\%$ . The leftmost graph (purple) shows the (linear + quadratic) variation caused by uniaxial stress. The center graph (blue) shows the linear contribution from  $A_{1g}$  strain, and the rightmost graph (red) shows the quadratic contribution from  $B_{1g}$  strain. (C) Schematic  $T_S - \epsilon_{A_{1g}} - \epsilon_{B_{1g}}$  phase diagram. The experimental path lies along the straight line between  $\epsilon_{A_{1g}}$  and  $\epsilon_{B_{1g}}$  axes. The effects of these two tuning parameters are generally uncorrelated. However, in the presence of strong quantum critical fluctuations, the coefficients of both the linear and quadratic strain responses (resulting from the response to the  $A_{1g}$  and  $B_{1g}$  strains, respectively) are both related to the zero-strain transition temperature as  $1/T_0^{1/\theta}$ .

in the presence of strong quantum critical fluctuations.

Uniaxial stress was applied to  $\text{Ba}(\text{Fe}_{1-x}\text{Co}_x)_2\text{As}_2$  single crystals using a commercially available strain cell (CS100, *Razorbill Instrument*) and varied in-situ in an almost continuous fashion. Bar-shaped single-crystalline samples (with typical dimensions of  $2000 \times 500 \times 35 \mu\text{m}$ , cut along [100] direction) are glued onto two mounting plates, that can be pushed/pulled by varying the voltage to sets of lead-zirconium-titanate (PZT) piezoelectric stacks. The strain cell is designed to compensate for thermal expansion of the PZT [64], and because the differential thermal expansion of the cell body and the sample is negligible, the strain is almost perfectly temperature independent at a fixed voltage [65]. Strain along the [100] crystallographic direction,  $\epsilon_{xx}$ , can be inferred from the change in the mounting plate separation by measuring the change in capacitance of the capacitive sensor inside the cell body using a capacitance bridge (*Andeen-Hagerling AH2550A*). Through finite element simulation, the strain relaxation through the glue can be estimated, and the strain experienced by the sample is found to be approximately  $\sim 70\%$  of the measured strain [65]. The strains  $\epsilon_{A_{1g}}$  and

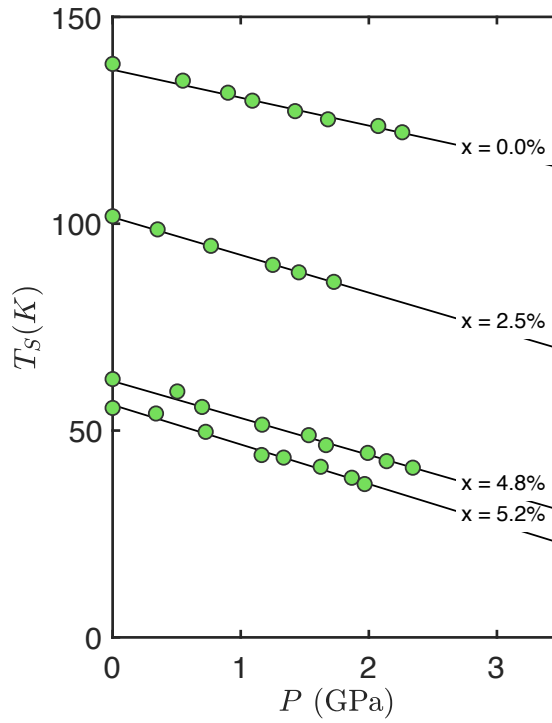


Figure 4.2: **Response of  $T_S$  to applied hydrostatic pressure for various compositions of  $\text{Ba}(\text{Fe}_{1-x}\text{Co}_x)_2\text{As}_2$ .** The green circles represent the measured critical temperature  $T_S$  as a function of applied hydrostatic pressure  $P$ . The black lines represent the linear fit to the data. It can be seen that in all compositions, the variation is linear. Thus the quadratic variation in uniaxial stress experiment is exclusively caused by the orthogonal antisymmetric  $B_{1g}$  strain.

$\epsilon_{B_{1g}}$  are related to  $\epsilon_{xx}$  via the elastic moduli  $c_{ijkl}$  of the samples. It can be shown that a variation in  $c_{ijkl}$  within the composition and temperature range investigated here has no effect on the conclusions of this work. The critical temperature  $T_S$  is determined using AC elastoresistivity [57], as well as in some cases AC elastocaloric effect described in detail elsewhere [61].

### 4.3 Result

Fig.4.1 illustrates schematically how the deformation stemming from the [100] uniaxial stress can be expressed as a linear combination of the symmetric and antisymmetric strains  $\epsilon_{A_{1g}}$  and  $\epsilon_{B_{1g}}$ . Because  $\epsilon_{A_{1g}}$  and  $\epsilon_{B_{1g}}$  are both linearly proportional to  $\epsilon_{xx}$ , and that the coefficient  $a'$  is vanishingly small, the variation of  $T_S$  due to [100] uniaxial stress is

$$T_S(\epsilon_{xx}) = T_0 + \alpha\epsilon_{xx} + \beta\epsilon_{xx}^2, \quad (4.2)$$

where  $\alpha = dT_S/d\epsilon_{xx} \propto \partial T_S/\partial\epsilon_{A_{1g}}$  and  $\beta = 1/2 \times d^2T_S/d\epsilon_{xx}^2 \propto \partial^2 T_S/\partial\epsilon_{B_{1g}}^2$ . Fig.4.1B shows representative data for a sample with composition  $x = 4.8\% \pm 0.2\%$  revealing the linear and quadratic behavior.

Further investigation of the coefficients  $\alpha$  and  $\beta$  within the doping series of  $\text{Ba}(\text{Fe}_{1-x}\text{Co}_x)_2\text{As}_2$  reveals a notable result. Figure 4.3 shows the critical temperature  $T_S$  becomes more sensitive to the applied uniaxial stress as the cobalt concentration approaches the optimally doped composition. To be more specific, the linear coefficient  $\alpha$  and the quadratic coefficient  $\beta$  grow towards the optimally doped composition.

Fig.4.4A shows the normalized coefficients  $\alpha/T_0$  and  $\beta/T_0$  as a function of cobalt concentration  $x$ . Both normalized coefficients grow monotonically and appear to diverge as the cobalt concentration approaches the critical doping,  $x_c$ . Here,  $x_c$  is defined in the absence of superconductivity, and it was recently measured to be  $x_c \sim 6.7 \pm 0.2\%$  using high magnetic fields to suppress the superconducting phase [104].

In what follows, we argue that a power law describing the divergence of  $\alpha/T_0$  and  $\beta/T_0$  is a hallmark for quantum critical fluctuations. We start from the ansatz:

$$T_S \sim (g_C - g)^\theta. \quad (4.3)$$

This suggests that within a regime dominated by quantum critical fluctuations, the finite temperature phase transition is governed by a power law of some (relevant) nonthermal tuning parameter,  $g$  [49]. Here,  $g_C$  is the value of  $g$  at the QCP, and  $\theta$  is the critical exponent governing the phase boundary in the immediate vicinity of the QCP [106]. In the context of this work,  $g$  can be varied by varying either  $\epsilon_{A_{1g}}$  or  $\epsilon_{B_{1g}}^2$  [107], and we reiterate that these are distinct tuning parameters belonging to orthogonal symmetry channels.

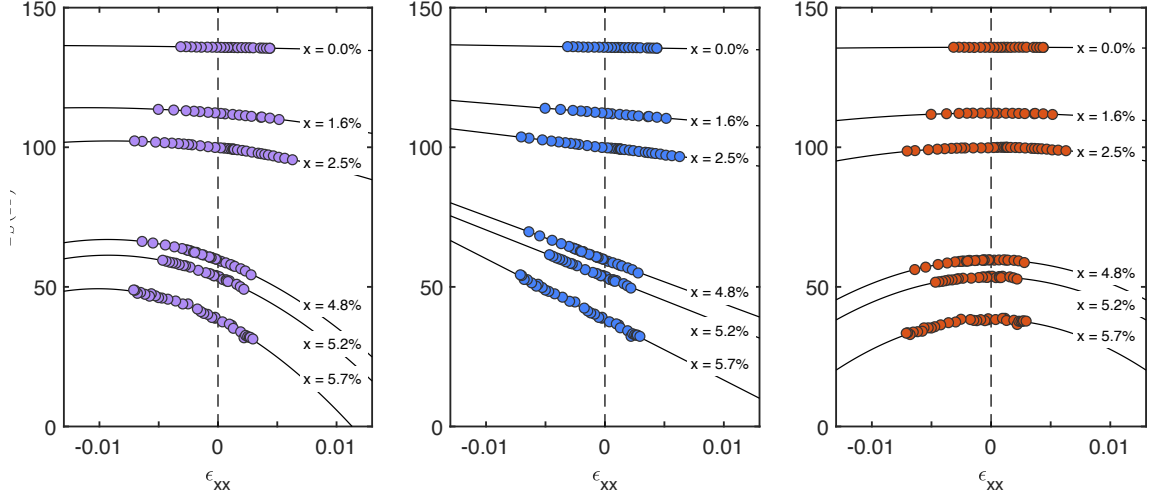


Figure 4.3: **Response of  $T_S$  to applied uniaxial stress along [100] in various cobalt concentrations of  $\text{Ba}(\text{Fe}_{1-x}\text{Co}_x)_2\text{As}_2$ .** (A) The purple circles represent the measured critical temperature  $T_S$  as a function of the deduced strain  $\epsilon_{xx}$ . The black lines represent linear + quadratic fits to the data. As the cobalt concentration approaches the critical doping of  $x_c \sim 6.7\%$ , both the quadratic and linear coefficients increase. Panel (B) and (C) represent the linear and quadratic constituents due to  $A_{1g}$  and  $B_{1g}$ , respectively.

Taylor expanding Eq. 4.3 in a small-strain region around zero strain and substituting  $g_C \sim T_0^{1/\theta}$ , we arrive at a simple expression for the leading order effect of the tuning parameter  $g$  on  $T_S$  in the quantum critical regime:

$$\frac{T_S}{T_0} = 1 - \frac{C\theta}{T_0^{1/\theta}} g + O(g^2), \quad (4.4)$$

where  $C$  is a constant. Substituting  $\epsilon_{A_{1g}}$  or  $\epsilon_{B_{1g}}^2$  for  $g$  gives  $\alpha/T_0 \sim -T_0^{-1/\theta}$  and  $\beta/T_0 \sim -T_0^{-1/\theta}$  respectively. This is the power law that governs the morphology of the strain-tuned phase diagram in the presence of quantum critical fluctuations. Notice in particular that in the quantum critical regime, the same power law governs the behavior of both symmetry channels, even though these two strains belong to distinct irreducible representations of the point group (fig.4.1C). Notice also how the composition  $x$  does not enter into Eq. 4.4. All that is needed is a measurement of  $T_0$  and of the rate of suppression of  $T_S$  with respect to  $\epsilon_{A_{1g}}$  and  $\epsilon_{B_{1g}}^2$ . If the material is in the quantum critical regime tuned by  $x$ , then these two coefficients will follow the same power-law behavior.

The distinct advantages of this perspective lie in (i) the fine tunability of  $\epsilon_{xx}$ , allowing for the accurate determination of  $dT_S/d\epsilon_{xx}$  and  $d^2T_S/d\epsilon_{xx}^2$ ; (ii) the simultaneous determination of the effect of two tuning parameters (symmetric and antisymmetric strains) within a single experiment; (iii) the circumvention of the large uncertainties in determining the chemical composition, i.e., the determination of the chemical composition is unnecessary; and (iv) our approach completely bypasses the

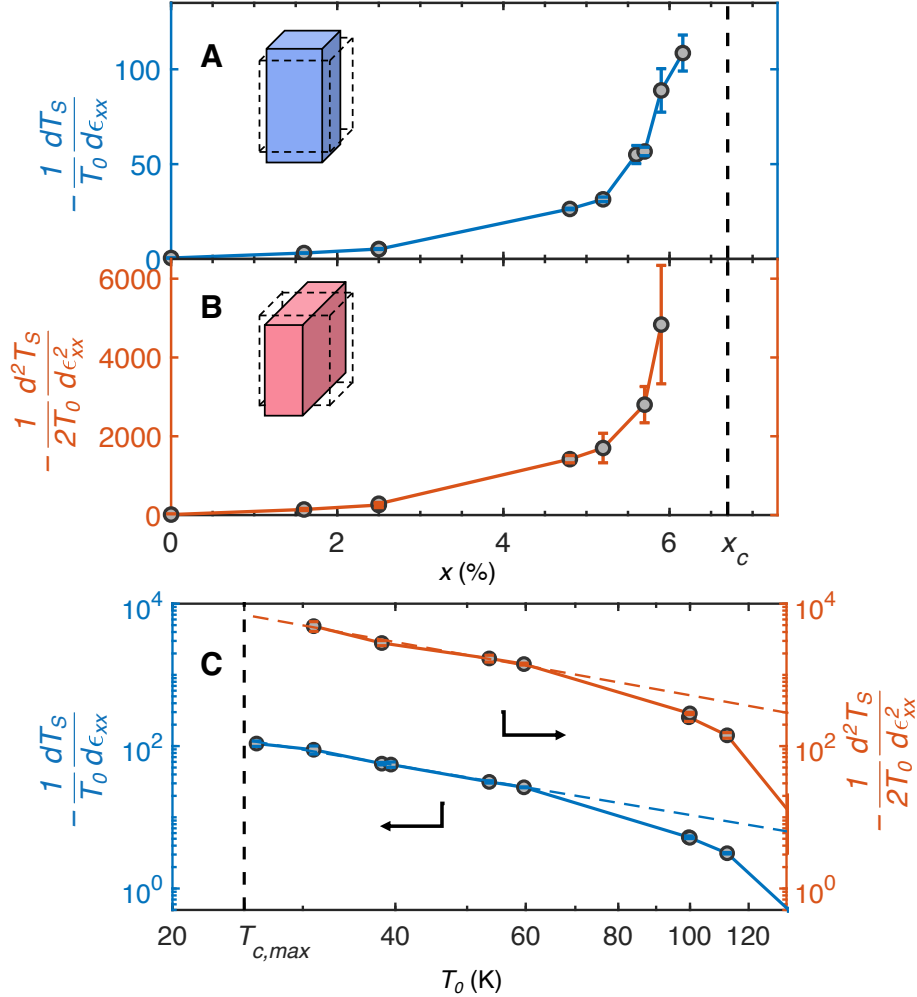


Figure 4.4: **Power law divergence of  $dT_S/d\epsilon_{xx}$  and  $d^2T_S/d\epsilon_{xx}^2$  as a function of cobalt concentration  $x$  in  $\text{Ba}(\text{Fe}_{1-x}\text{Co}_x)_2\text{As}_2$ .** (A) The linear coefficient of the variation of  $T_S$  caused by symmetric  $A_{1g}$  strain, and (B) the quadratic coefficient caused by antisymmetric  $B_{1g}$  strain, each case normalized by the zero-strain critical temperature  $T_0$ . The schematic insets illustrate the appropriate irreducible representations of strain for the two cases. Both the linear and the quadratic coefficient diverge as the cobalt concentration approaches the critical doping of  $x_c \sim 6.7\%$  (vertical dashed line). (c) The same normalized coefficients as a function of zero-strain critical temperature  $T_0$  shown in a log-log scale. The linear behavior seen in this plot at low temperatures indicates similar power law behavior for both symmetry channels. The slopes of the linear regimes are equal to the inverse critical exponent  $1/\theta$ , which is found to be  $1/\theta = 1.75 \pm 0.2$  and  $1/\theta = 1.87 \pm 0.7$  for  $A_{1g}$  and  $B_{1g}$  strain respectively; these values agree within a standard deviation. Note that extracting statistically significant quadratic coefficients requires data extending to relatively large strains. For two experiments (two extra data points in the blue traces), this strain regime could not be reached before the mechanical failure of the sample, so only the linear coefficients are shown.

need to determine the critical value of the tuning parameter  $g_C$  (with respect to composition or strain), because the analysis investigates the variation of  $T_S$  with respect to the tuning parameter in the limit of small strains (this is especially useful in the present context because of the presence of the superconducting dome, but more generally it eliminates all errors that one would ordinarily incur from considering decades of variation in the quantity  $\delta = g - g_C$  when both  $g$  and  $g_C$  suffer from large uncertainty).

The power law behavior in  $\alpha/T_0$  and  $\beta/T_0$  is visualized best as a log-log plot for which a straight line with a slope of  $1/\theta$  is expected for both coefficients. This is precisely what is observed, as is shown in fig.4.4B. As the zero-strain critical temperature ( $T_0$ ) decreases (tuned by composition,  $x$ ), there is an apparent tendency for the strain coefficients towards a linear behavior in the log-log plot, indicated by the dashed lines. The cross-over regime appears at a similar value of  $T_0$  for both  $\alpha/T_0$  and  $\beta/T_0$ . Moreover, the slopes of the best-fits which represent the inverse critical exponents appear to be similar in both cases, with the value  $1/\theta = 1.75 \pm 0.2$  for  $\alpha/T_0$ , and  $1/\theta = 1.87 \pm 0.7$  for  $\beta/T_0$ , agreeing within experimental error. Averaging the two exponents obtained from the temperature dependence of the linear and quadratic coefficients, we obtain  $\theta = 0.56 \pm 0.07$ .

### 4.3.1 The effect of variation in elastic moduli to the observed power-law behavior

Since our experiment is done with samples with various cobalt concentration, it is important to understand the effect of the variation in the elastic moduli to our observed power-law behavior. This symmetry-preserving strain  $\epsilon_{A_{1g}}$  can be expressed as a linear combination of the in-plane  $\epsilon_{A_{1g,1}}$  and the out-of-plane  $\epsilon_{A_{1g,2}}$  symmetry preserving strain and the relative magnitude of the two strain modes depends on the applied uniaxial stress, and the elastic moduli of the samples. If the elastic moduli change, the ratio of  $\epsilon_{A_{1g,1}}$  and  $\epsilon_{A_{1g,2}}$  (and also  $\epsilon_{B_{1g}}$ ) will change, which could in turn alter our result. Here we will show that in the range of our experiment, the effect of changes in the elastic moduli is very small, such that the power law stays intact.

According to [108], the elastic tensors for  $x = 3.7\%$  and  $x = 6.0\%$  samples are

$$C_{3.7\%} = \begin{pmatrix} 93 & 11 & 11 \\ 11 & 93 & 11 \\ 11 & 11 & 88 \end{pmatrix} GPa, \quad (4.5)$$

and

$$C_{6.0\%} = \begin{pmatrix} 112 & 27 & 27 \\ 27 & 112 & 27 \\ 27 & 27 & 84 \end{pmatrix} GPa \quad (4.6)$$

respectively. Note here that since  $C_{13}$  cannot be measured accurately because of the crystal shape,

$C_{13}$  is assumed to be equal to  $C_{12}$ , the same way in [108].

The relation between  $\epsilon_{A_{1g,1}}$  and  $\epsilon_{A_{1g,2}}$ , and  $\epsilon_{xx}$  is found to be  $\epsilon_{A_{1g,1}} = \frac{1}{2}(1 - \nu)\epsilon_{xx}$  and  $\epsilon_{A_{1g,2}} = -\nu'\epsilon_{xx}$ , where  $\nu$  and  $\nu'$  are in-plane and out-of-plane Poisson's ratio. From the elastic tensors, one obtain  $\nu_{3.7\%} = 0.11$  and  $\nu'_{3.7\%} = 0.27$  for  $x = 3.7\%$  cobalt concentration, and  $\nu_{6.0\%} = 0.18$  and  $\nu'_{6.0\%} = 0.26$  for  $x = 6.0\%$  cobalt concentration. This change in the Poisson ratios causes the prefactors  $-\nu'$  and  $\frac{1}{2}(1 - \nu)$  to change by  $-4\%$  and  $-9\%$  from  $3.7\%$  to  $6.0\%$  cobalt concentration. For  $\epsilon_{B_{1g}} = \frac{1}{2}(1 + \nu)\epsilon_{xx}$ , the change of the prefactor is  $+6\%$ .

The changes of the Poisson ratios enters in the coefficients  $\alpha$  and  $\beta$  in Eq.(2) in the main text. However, the coefficients  $\alpha$  and  $\beta$  change by more than 100% from  $x = 4.8\%$  to  $x = 5.7\%$ . Therefore, the effect of change in elastic moduli is negligible to wide extent.

Furthermore, these changes are unlikely to contribute to the power law dependence in temperature. Consider a power law in case of two tuning parameters

$$T_S = (T_0^{1/\theta} - a_1\epsilon_{A_{1g,1}} - a_2\epsilon_{A_{1g,2}})^\theta = (T_0^{1/\theta} - C\epsilon_{xx})^\theta \quad (4.7)$$

where  $a_1$  and  $a_2$  are constants and  $C = \frac{1}{2}(1 - \nu)a_1 - \nu'a_2$ . The change in  $C$  is at most  $-9\%$  as shown above. Taylor expansion to leading order yields Eq.(4) in the main text:

$$\frac{T_S}{T_0} = 1 - \frac{C\theta}{T_0^{1/\theta}}\epsilon_{xx} + O(\epsilon_{xx}^2), \quad (4.8)$$

Since  $C$  has absorbed the change in the Poisson ratios, one would expect it to change as a function of chemical substitution. Given that there is no critical behavior in the elastic moduli, as it has not been observed in previous work [108], we assume that  $C$  changes slowly and linearly in doping:  $C = C_0 + k(x_c - x)$  where  $x_c$  is the critical doping. Substitution into Eq.(4.8) gives

$$\frac{T_S}{T_0} = 1 - \frac{(C_0 + k(x_c - x))\theta}{T_0^{1/\theta}}\epsilon_{xx} + O(\epsilon_{xx}^2) = 1 - \left( \frac{C_0\theta}{T_0^{1/\theta}} + D \right) \epsilon_{xx} + O(\epsilon_{xx}^2) \quad (4.9)$$

where the last equality comes from the fact that  $(x_c - x) \sim T^{1/\theta}$ . This shows that the slowly varying elastic moduli do not affect the temperature dependence of the linear coefficient  $\alpha/T_0$ . The same result can analogously also be found for  $B_{1g}$  strain.

## 4.4 Scaling collapse of $T_S$ as a function of combined tuning parameters

The power-law behavior observed in the previous section can equivalently be illustrated by a scaling collapse with respect to the combined non-thermal tuning parameters. As a function of the 3 tuning parameters in the experiment,  $x$ ,  $\epsilon_{A_{1g}}$  and  $\epsilon_{B_{1g}}$ , the critical temperature  $T_S$  varies in the quantum

critical regime as follows:

$$T_S(x, \epsilon_{A_{1g}}, \epsilon_{B_{1g}}) = \delta^\theta, \quad (4.10)$$

where  $\delta$  is the magnitude of the "relevant" perturbation which is thus a linear combination of the various tuning parameters. In the context of our experiment,  $\delta$  can be expressed as

$$\delta = A_1 \epsilon_{A_{1g},1} + A_2 \epsilon_{A_{1g},2} + A_3 \epsilon_{B_{1g}}^2 + A_4 (x - x_C). \quad (4.11)$$

where  $A_j$ , for  $j = 1 - 4$  are constants. If the (free standing) material lies within quantum critical regime, then its free standing critical temperatures can also be expressed as a power law of doping  $T_0(x) \equiv T_S(x, 0, 0) \sim (x - x_C)^\theta$ . Substitute this into Eq. 4.10, and use the fact that  $\epsilon_{A_{1g},1}$ ,  $\epsilon_{A_{1g},2}$ , and  $\epsilon_{B_{1g}}$  are linearly proportional to  $\epsilon_{xx}$ , one arrives at

$$T_S(x, \epsilon_{xx}) = [T_0(x)^{1/\theta} + A'_1 \epsilon_{xx} + A'_2 \epsilon_{xx}^2], \quad (4.12)$$

where  $A'_1$  and  $A'_2$  are constants. With appropriate fit values of  $A'_1$ ,  $A'_2$ , and  $\theta$ , the data points should collapse into a single line inside the quantum critical regime. In order to find appropriate fit parameters, Eq. 4.12 is rearranged into

$$T_S(x, \epsilon_{xx})^{1/\theta} - T_0(x)^{1/\theta} = A'_1 \epsilon_{xx} + A'_2 \epsilon_{xx}^2, \quad (4.13)$$

and fit the data into this second-degree polynomial with various  $\theta$  values. The best fit  $\theta$  can be obtained from an R-square analysis of this fit (Fig.4.5). Data collected from samples with Co-concentration between 4.8% and 6.2% are used in this fit, as they are in quantum critical regime as shown in Section 4.3. Samples with lower Co-concentration are outside of the quantum critical regime, and will not collapse into the same curve. The  $\theta$  scan is shown in Fig.4.5 where the best fit value is  $\theta = 0.52 \pm 0.02$  (the uncertainty is obtained using Trust-Region optimization methods). This value agrees with the the analysis in the previous section within the experimental uncertainty.

Figure 4.6 illustrate the relationship in Eq. 4.10 with appropriate fit parameters described above. A linear relationship of  $\delta$  and  $T_S^{1/\theta}$  can be seen in strain-tuned samples with  $T_S$  ranging from  $\sim 25$ K up to  $\sim 70$ K (sample with Co-concentration higher than 4.8%), establishing a nematic quantum critical regime where the energy scale of the system is dominated by quantum critical fluctuations. Samples with lower Co-concentration does not exhibit this scale collapse, indicating that non-critical degrees of freedom (microscopic) start to dominate the energy scale of the system.

## 4.5 Discussion

This value of  $\theta$  implies that the  $x$  derivative of  $T_S$  diverges as  $x$  approaches  $x_c$ , which is consistent with the shape of the phase diagram (fig.4.7B). Presumably this value of  $\theta$  relates to universal

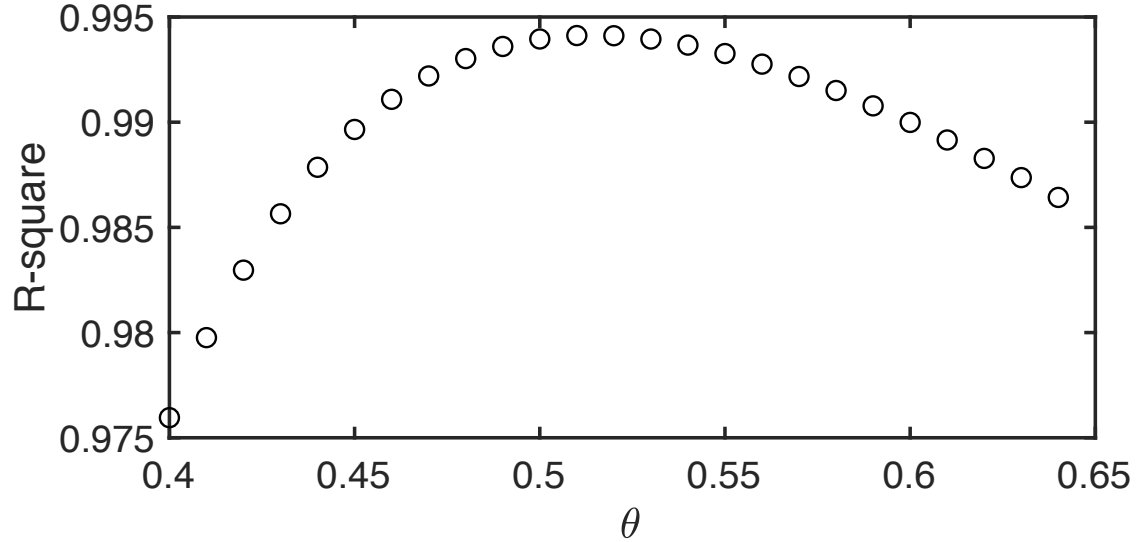


Figure 4.5: **Theta scan.** The plot shows the R-square value of the least square fit of Eq.(4.13) for various  $\theta$  values ranging from 0.4 – 0.65.  $\theta = 0.52 \pm 0.02$  give the best fit with R-square of 0.994.

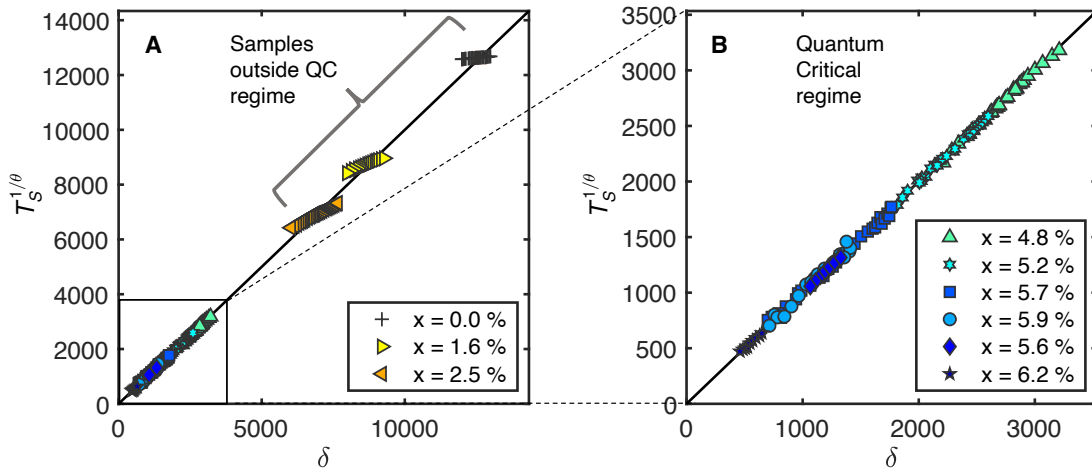


Figure 4.6: **Scaling collapse of non-thermal tuning parameters.** (A) The scaling collapse described in Eq. 4.12, in which  $T_S^{1/\theta}$  is plotted versus  $\delta$ . The best fit value  $\theta = 0.52 \pm 0.02$  is extracted using the method explained in Section 4.4. Symbols represent samples with differing dopings. The data is expected to collapse onto a single line in the quantum critical regime which is observed for samples within a range of Co concentrations between  $x = 4.8\%$  and  $6.2\%$ . This regime is magnified in the plot in panel (B), which shows a collapse over almost a decade of  $\delta$ .

exponents of a universality class appropriate for metallic Ising nematic systems with disorder, and as such provides a test for future theoretical treatments.

It is worth noting that the measured value of  $\theta$  is equal within experimental error to the theoretically predicted value ( $\theta = 0.5$ ) for a zero-temperature structural transition in a (Fermi liquid) metal [109]. However, although considerations of universality suggest that this observation may be pertinent asymptotically close to the putative QCP, in most or all of the parameter range covered by our experiments, the nematic fluctuations are primarily a property of the metallic degrees of freedom. In particular, a variety of experiments, including elastoresistivity [17, 47], elastic stiffness measurements [32], and Raman scattering [33, 34, 35] have shown that the driving force for the nematic transition comes primarily from the low-energy metallic degrees of freedom and that the response of the lattice is mostly parasitic.

Ideally, power law behavior is established over decades of a tuning parameter. In the present case, however, the presence of superconductivity at  $T_{c,max} \sim 25K$  limits the accessible parameter range (chemical doping or  $T_0$ ) for our investigation. Nevertheless, the observation of such closely similar behavior for the two fully-independent tuning parameters  $\epsilon_{A_{1g}}$  and  $\epsilon_{B_{1g}}$ , and the scaling collapse shown in fig.4.6, provide compelling evidence that the apparent power law behavior is driven by critical fluctuations.

The power law variation of  $\alpha/T_0 \sim -1/T^{1/\theta}$  and  $\beta/T_0 \sim -1/T^{1/\theta}$  implies that the normalized quantities,  $T^{1/\theta} \times \alpha/T_0$  and  $T^{1/\theta} \times \beta/T_0$ , should be constant so long as the material is in the quantum critical regime. This behavior is verified in fig.4.7A, which shows the variation of the normalized quantities as a function of composition,  $x$ . This figure makes clear two very important points. Firstly, the composition  $x$  does not need to be accurately determined to deduce that the material is in the quantum critical regime; it is sufficient solely that the normalized quantities have constant values, and the absolute value of the  $x$ -coordinates in fig.4.7A does not matter in reaching this conclusion. Secondly, the regime of power law exists over a substantially wide regime of composition and temperature (gray brackets in fig.4.7A and fig.4.7B), extending over the majority of the superconducting dome for these underdoped compositions. The immediate implications for superconductivity are unknown. However, these experimental results empirically establish that the superconductor is not only born out of a metal that hosts strong nematic fluctuations (as has been previously inferred from a wide variety of measurements [47, 17, 33, 34, 35]), but more specifically is born from a metal that exhibits *quantum critical* nematic fluctuations. Put another way, for a wide range of compositions in the  $x - T$  plane, the material ‘knows’ how far it is from the nematic QCP tuned by chemical composition, and this approximately correlates with the range of compositions over which the material superconducts.

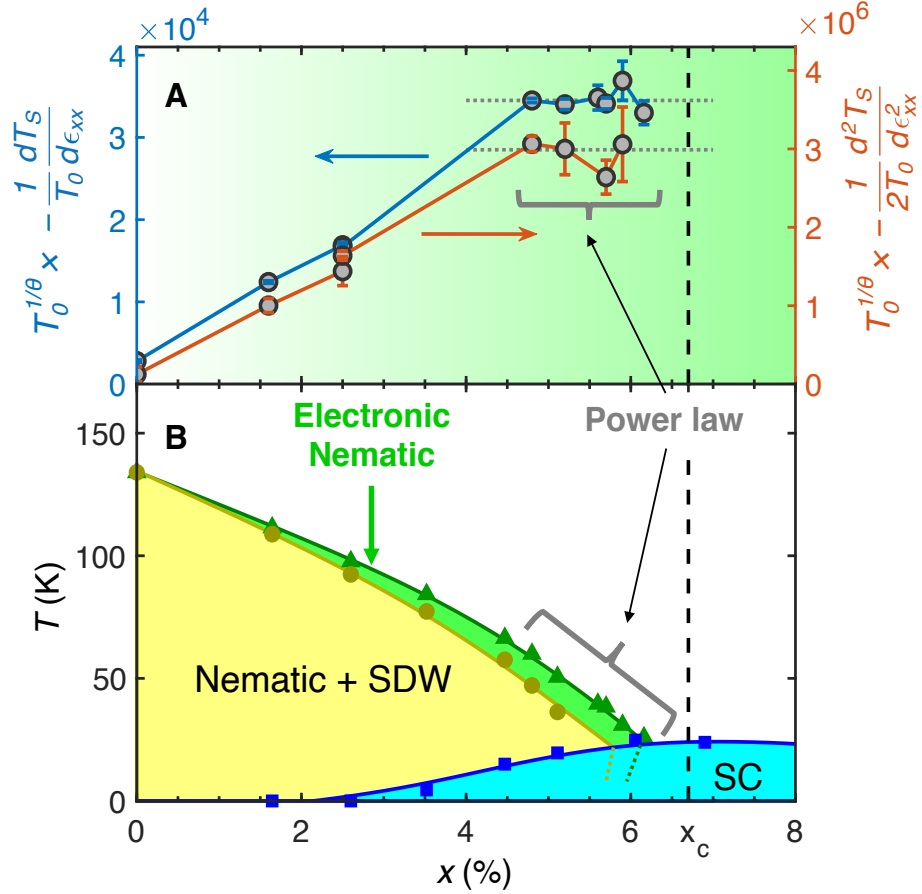


Figure 4.7: **Quantum criticality in  $\text{Ba}(\text{Fe}_{1-x}\text{Co}_x)_2\text{As}_2$  phase diagram.** (A) The normalized linear  $\alpha/T_0$  (left axis) and quadratic coefficients  $\beta/T_0$  (right axis), scaled with the expected zero-strain critical temperature dependent  $T_0^{-1/\theta}$ . These quantities are expected to be constant in the quantum critical regime, which spans the higher dopings, as suggested by the dotted line. The green shading represent the ratio of these scaled coefficients with their saturated value. (B) Phase diagram of  $\text{Ba}(\text{Fe}_{1-x}\text{Co}_x)_2\text{As}_2$  [7]. Power law behavior is observed for materials with a cobalt concentration between  $x = 4.8\% \pm 0.2\%$  all the way to  $x = 6.2\% \pm 0.2\%$ , above which  $T_S$  is unobservable due to the presence of superconductivity. This power-law behavior signifies the presence of strong nematic fluctuation of quantum origin due to the presence of the nematic QCP at  $x_c$ . Note that the dotted lines in (B) denotes the phase transition lines which presumably backbend inside the superconducting state [16].

## Chapter 5

# Probing nematic susceptibility while continuously tuning the system with strain

In this chapter, I describe an experimental approach that permits, at least in principle, measurement of the  $B_{2g}$  nematic susceptibility while simultaneously tuning the nematic critical temperature with  $A_{1g}$  and  $B_{1g}$  DC offset strain. The patterning of the microstructure, an essential component of this chapter, was carried out with the assistant of M.D. Bachmann.

### 5.1 Introduction

In the previous two chapters, it has been shown that  $A_{1g}$  and  $B_{1g}$  strains can be used to tune the critical temperature of the nematic phase transition  $T_S$ . A quantity of fundamental interest is the nematic susceptibility,  $\chi_{B_{2g}}$ . Ideally, one would like to devise means to tune  $T_S$  while simultaneously measuring  $\chi_{B_{2g}}$ . This chapter briefly motivates why such a measurement would be so desirable and describes a method that does exactly this. We do this using a combination of an applied magnetic field and a time-varying strain. Our results indicate that the coefficient coupling this effective field to the nematic order parameter is too small to be measured in this material. However, the technique has distinct promise for other material systems. Therefore, we describe both the method and specific results here, hoping that this will be useful for future investigations of alternative materials.

How disorder plays a role in nematic fluctuations, especially in the context of quantum criticality, is an ongoing debate. It has been shown (see supplementary materials of [47]) that even weak disorder can grow stringer upon approaching criticality. It can even induce non-perturbative effects such as quantum Griffith phases, which could alter thermodynamic properties of the material [110, 111].

Measurement of nematic susceptibility in cobalt-substituted  $\text{BaFe}_2\text{As}_2$  via elastoresistivity shows a peculiar behavior [47]. The elastoresistivity coefficient  $m_{B_{2g}, B_{2g}}$  deviates from Curie-Weiss behavior at low temperature. This effect is most severe close to the optimally doped composition, and diminishes away from it in both underdoped and overdoped directions. In fact, at 2.5% cobalt concentration or lower,  $m_{B_{2g}, B_{2g}}$  fits Curie-Weiss function perfectly down to the critical temperature  $T_S$ . This behavior is also seen in potassium- and nickel-substituted  $\text{BaFe}_2\text{As}_2$ , which are hole- and electron-doped systems, respectively. Remarkably, this effect is totally absent in the phosphorus-substituted  $\text{BaFe}_2\text{As}_2$ , which is an isovalently-substituted system and the least disordered system of them all. This suggests that the effect may be originated from an interplay between disorder and quantum criticality. Significantly, a glassy incommensurate magnetic phase was observed via neutron scattering experiment around to the putative quantum critical point in the nickel-substituted  $\text{BaFe}_2\text{As}_2$  system, interrupting the nematic and magnetic phase transitions from reaching zero temperature. As a result, the quantum critical point is ‘avoided’ [3, 4, 6].

To gain insights into the effect of disorder on the nematic susceptibility, one seeks a new tuning parameter that does not alter the disorder or doping level in the material. Naturally, one such tuning parameter is the hydrostatic pressure; however, to induce the nematic order parameter, a symmetry-breaking strain is required, which cannot be achieved inside a hydrostatic pressure cell. A more viable candidate is the uniaxial stress, introduced in Chapter 3. With this setup, symmetry-breaking strain can be induced. Furthermore, both  $A_{1g}$  and  $B_{1g}$  strains become more effective tuning parameters close to the nematic quantum critical point due to the power-law behavior [72], making this prospect even more compelling.

Since  $B_{2g}$  conjugate field smears the phase transition (see Section 1.3.2), the problem statement is, therefore, how to tune  $T_S$  with large  $A_{1g}$  and  $B_{1g}$  strains, while keeping  $B_{2g}$  conjugate field small only to measure the susceptibility. One can quickly see that simply misaligning the sample with the strain axis does not work, as a large  $B_{2g}$  will also be induced when a large offset uniaxial stress is applied. The technique introduced in the next section uses a novel  $B_{2g}$  conjugate field, which is a combination of the time derivative of  $B_{1g}$  strain and magnetic field to induce the nematic order parameter for measuring the susceptibility. Since only  $B_{1g}$  strain is required, stress is applied along [100] crystallographic direction of the material. This allows for tuning with large  $A_{1g}$  and  $B_{1g}$  strains while applying infinitesimal  $B_{2g}$  conjugate field for measuring nematic susceptibility.

## 5.2 The Trilinear coupling

To construct a new conjugate field, consider the product table in Table 1.2. A  $B_{2g}$  quantity can be produced by combining a  $B_{1g}$  quantity and an  $A_{2g}$  quantity. According to the character table (1.1), the  $A_{2g}$  quantity can be represented by a rotation around the z-axis,  $R_z$ , or equivalently an axial vector that point along the z-axis. This description fits the magnetic field,  $H_z$  precisely. However,

since  $H_z$  is antisymmetric under the time-reversal operator, a time operator is required to make the overall term symmetric under the time-reversal operator. This can be achieved by taking a derivative with respect to time. The following trilinear coupling was proposed by R.M. Fernandes:

$$\Delta F_{\text{trilinear}} = \eta H_z \dot{\epsilon}_{B_{1g}} \psi_{B_{2g}}, \quad (5.1)$$

where  $\dot{\epsilon}_{B_{1g}}$  is a time derivative of the  $B_{1g}$  strain,  $H_z$  is magnetic field along [001] crystallographic direction, and  $\psi_{B_{2g}}$  is the nematic order parameter. This makes the combined conjugate field  $\dot{\epsilon}_{B_{1g}} H_z$  a time-reversal symmetric  $B_{2g}$  quantity, and hence couple directly to  $\psi_{B_{2g}}$ .

In the disordered state, one can calculate the nematic order parameter induced by this combined conjugate field  $H_z \dot{\epsilon}_{B_{1g}}$  by minimizing the Landau free energy with respect to the order parameter. The total free energy in the presence of magnetic field and  $B_{1g}$  strain is

$$\Delta F = \frac{1}{2} \chi^{-1} \psi_{B_{2g}}^2 + \lambda_{B_{1g}B_{1g}, B_{2g}B_{2g}} \epsilon_{B_{1g}}^2 \psi_{B_{2g}}^2 + \eta H_z \dot{\epsilon}_{B_{1g}} \psi_{B_{2g}}, \quad (5.2)$$

where the second term is the biquadratic coupling between  $\epsilon_{B_{1g}}$  and  $\psi_{B_{2g}}$  as introduced in Section 1.3.2; and as shown the section, this coupling results in a shift in  $T_S$  by renormalizing  $\chi^{-1}$ . This term can, therefore, be absorbed into the  $\chi$ . Minimizing the free energy with respect to the order parameter obtains:

$$\psi_{B_{2g}} = \eta \chi H_z \dot{\epsilon}_{B_{1g}}. \quad (5.3)$$

Here the combined conjugate field  $H_z \dot{\epsilon}_{B_{1g}}$  can induce the nematic order parameter just like the  $B_{2g}$  strain.

The induced nematic order parameter can be probed by measuring the resistivity anisotropy in the  $B_{2g}$  channel, which can be expressed as

$$\left( \frac{\Delta \rho}{\rho} \right)_{B_{2g}} = g_{T,x} \psi_{B_{2g}} = g_{T,x} \eta \chi H_z \dot{\epsilon}_{B_{1g}}, \quad (5.4)$$

where  $g_{T,x}$  is a constant that relates the resistivity anisotropy to the nematic order parameter, the exact one defined in Section 1.3.3.

Taking the derivative of the resistivity anisotropy with respect to  $H_z$  and  $\dot{\epsilon}_{B_{1g}}$ , one obtains a quantity which is a proxy for the nematic susceptibility:

$$\frac{\partial^2}{\partial \dot{\epsilon}_{B_{1g}} \partial H_z} \left( \frac{\Delta \rho}{\rho} \right)_{B_{2g}} \Big|_{H_z = \dot{\epsilon} = 0} = g_{T,x} \eta \chi \propto \chi. \quad (5.5)$$

The quantity that is similar to  $m_{B_{2g}, B_{2g}}$ ; however, this is not an elastoresistivity coefficient, as the resistivity anisotropy is not induced by the  $B_{2g}$  strain. Rather, it is induced by a combination of time-derivative of strain and magnetic field. This quantity is dubbed the *Hall viscosity coefficient*.

This nomenclature comes from the combination of the Hall coefficient<sup>1</sup> and the viscosity. The Hall coefficient is defined as the derivative of the transverse resistivity with respect to the applied magnetic field. The viscosity is defined as the derivative of stress tensor with respect to the *shear velocity*<sup>2</sup>. Therefore, it is appropriate to call the quantity, which is defined as the derivative of the Hall coefficient with respect to the  $B_{1g}$  shear velocity, the Hall viscosity coefficient.

The method used to measure the Hall viscosity coefficient is inspired by the transverse elastoresistivity method explained in Section 2.4. This is outlined in the next section.

### 5.3 Measurement of the Hall viscosity coefficient

The simplest way to induce the  $\dot{\epsilon}_{B_{1g}}$  term is by applying oscillating stress along [100] direction. The combination of the oscillating strain and the magnetic field  $H_z$  will induce the resistivity anisotropy in the  $B_{2g}$  channel according to Eq.5.4. This  $B_{2g}$  resistivity anisotropy will be oscillating with time and out of phase with strain, as the time derivative introduces an extra phase of  $90^\circ$ . This can be measured via transverse resistivity configuration similar to that introduced in Section 2.4, and since the resistivity anisotropy is oscillating, it can be measured using the amplitude demodulation method [57], with some subtle difference from what is introduced in Section 2.4.

#### Measuring resistivity anisotropy via transverse resistivity configuration

The  $B_{2g}$  resistivity anisotropy can be expressed in the cartesian coordinate as

$$\left(\frac{\Delta\rho}{\rho}\right)_{B_{2g}} = \left(\frac{\Delta\rho}{\rho}\right)_{xy} = \frac{\Delta\rho_{xy}(\dot{\epsilon}, H)}{\sqrt{\rho_{xx}(\dot{\epsilon}, H=0)}\sqrt{\rho_{yy}(\dot{\epsilon}, H=0)}} = \frac{\Delta\rho_{xy}}{\rho_{xx}}, \quad (5.6)$$

as defined in Eq. 1.6 and 1.8, and  $\rho_{xx} = \rho_{yy}$  in the tetragonal state. The Hall viscosity coefficient is therefore

$$\frac{\partial^2}{\partial\dot{\epsilon}_{B_{1g}}\partial H_z} \left(\frac{\Delta\rho}{\rho}\right)_{B_{2g}} \Big|_{H_z=\dot{\epsilon}=0} = \frac{1}{\rho_{xx}} \frac{\partial^2 \rho_{xy}}{\partial\dot{\epsilon}_{B_{1g}}\partial H_z} \Big|_{H_z=\dot{\epsilon}=0}, \quad (5.7)$$

note that we can drop the  $\Delta$  inside the derivative since  $\frac{\partial^2}{\partial\dot{\epsilon}_{B_{1g}}\partial H_z} \rho_{xy}(\dot{\epsilon}, H=0) = 0$ . Hence, the Hall viscosity coefficient can be obtained by measuring the transverse (Hall) resistivity,  $\rho_{xy}$  and the longitudinal resistivity  $\rho_{xx}$ .

From Eq. 5.4, the change in Hall resistivity due to the trilinear coupling is

$$\Delta\rho_{xy} = \rho_{xx}g_{T,x}\eta\chi H_z\dot{\epsilon}_{B_{1g}}. \quad (5.8)$$

<sup>1</sup>It will become apparent in the next section why we use a Hall geometry to measure this signal.

<sup>2</sup>Shear velocity is a quantity that is equivalent to the time derivative of shear strain.

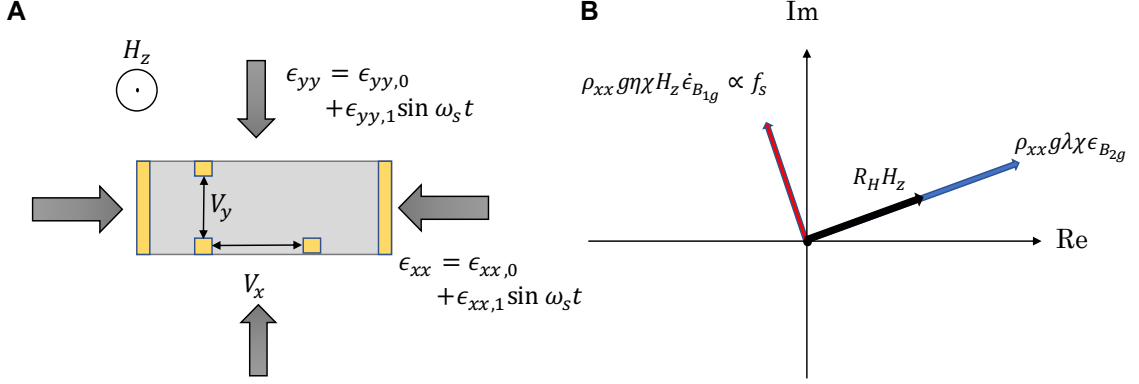


Figure 5.1: (A) The geometric of the sample. Biaxial strain  $\epsilon_\alpha = \epsilon_{\alpha,0} + \epsilon_{\alpha,1} \sin(\omega_s t)$ , ( $\alpha = xx, yy$ ) is induced by gluing the sample onto the PZT stack. The  $\epsilon_{\alpha,0}$  is used to tune the critical temperature  $T_S$ , while the oscillating part  $\epsilon_{\alpha,1} \sin(\omega_s t)$  is used to induce the nematic order parameter with magnetic field  $H_z$ . (B) the phase diagram comparing the three terms in Eq.5.10. The Hall resistivity, and the anisotropy induced by the  $B_{2g}$  strain is in phase with the strain. The anisotropy induced by the trilinear coupling is in quadrature with strain and is linearly dependent on frequency.

Substituting this term into Eq.5.7 yields

$$\frac{1}{\rho_{xx}} \left. \frac{\partial^2 \rho_{xy}}{\partial \dot{\epsilon}_{B_{1g}} \partial H_z} \right|_{H_z = \dot{\epsilon} = 0} = g_{T,x} \eta \chi \propto \chi. \quad (5.9)$$

This indicates that the Hall viscosity coefficient can be a proxy for the nematic susceptibility. In practice, this is not the only term that contributes to the resistivity in the Hall channel. The magnetic field will naturally introduce the Hall effect, and some misorientation of the sample to the strain axis will produce finite  $B_{2g}$  strain, which will also contribute to the Hall resistivity.

### Disentangling the Hall signal

Even though these effects appear in the same channel, they can be disentangled. Consider the total resistivity in the Hall channel:

$$\rho_{xy} = R_H H_z + \rho_{xx} g \lambda_{B_{2g}, B_{2g}} \chi \epsilon_{B_{2g}} + \rho_{xx} g \eta \chi H_z \dot{\epsilon}_{B_{1g}}, \quad (5.10)$$

The first term is the Hall effect, where  $R_H$  is the Hall coefficient of the sample. The second term arises from the bilinear coupling between the nematic order parameter  $\psi_{B_{2g}}$  and the  $B_{2g}$  strain (which arises due to imperfect sample alignment), and  $\lambda_{B_{2g}, B_{2g}}$  is the nemato-elastic coupling between  $\psi_{B_{2g}}$  and  $\epsilon_{B_{2g}}$ . The third term is the trilinear coupling introduced in this chapter.

Sinusoidal voltage  $V = V_0 \sin(\omega_s t)$  is applied into the PZT stacks at frequency  $f_s = \omega_s / 2\pi$ ,

	$R_H H_z$	$\rho_{xx} g \lambda_{B_{2g}, B_{2g}} \chi \epsilon_{B_{2g}}$	$\rho_{xx} g \eta \chi H_z \epsilon_{B_{1g}}$
Field dependence	Yes	No	Yes
Frequency dependence	No	No	Yes
Phase relative to strain	$0^\circ$	$0^\circ$	$90^\circ$

Table 5.1: There are three terms that contribute to the Hall resistivity in equation 5.11: the Hall effect, the resistivity anisotropy induced by  $B_{2g}$  strain, and the resistivity anisotropy induced by the trilinear coupling. These trilinear coupling can be distinguished completely from the other terms by looking at the the field dependence and the frequency dependence of the signal, and the phase of the signal relative to that of the induced strain.

inducing the oscillating strain. The time-dependent resistivity in Eq. 5.10 can be expressed as

$$\rho_{xy}(t) = R_H H_z + \rho_{xx} g \lambda \chi \epsilon_{B_{2g},1} \sin(\omega_s t) + \rho_{xx} g \eta \chi H_z \epsilon_{B_{1g},1} \omega_s \cos(\omega_s t), \quad (5.11)$$

where  $\epsilon_{xx,1}$  and  $\epsilon_{yy,1}$  are the amplitude of the oscillating  $xx$  and  $yy$  strains, respectively. The notation  $\epsilon_1$ 's are used as the  $\epsilon_0$ 's are already used for DC offset strains.

The beauty of this method is that the trilinear coupling term can be distinguished completely from the rest by observing temperature, magnetic field, and strain frequency dependence of the Hall signal. This is summarized in Table 5.1. The trilinear coupling is the only term that has a (i) linear magnetic field dependence, (ii) linear strain frequency dependence, (iii) Curie-Weiss temperature dependence, and (iv) is  $90^\circ$  out of phase with respect to strain. In this way, the trilinear coupling term can be distinguished from others.

### The amplitude demodulation method

In order to measure the trilinear part of the Hall signal, we utilize the amplitude demodulation technique [57] introduced in Section 2.4:

Consider only the trilinear coupling term from Eq. 5.11:

$$\rho_{xy,t}(t) = \rho_{xx} g \eta \chi H_z \epsilon_{B_{1g},1} \omega_s \cos(\omega_s t) = \rho_{xy,t} \cos(\omega_s t). \quad (5.12)$$

An AC current  $I_x(t) = I_0 \sin(\omega t)$  is sourced through the sample at a carrier frequency  $f_c$  ( $\neq f_s$ ), resulting an oscillating voltage with the following form:

$$V_y(t) = I_x(t) R_{xy,t}(t) = I_0 R_{xy,t} \sin(\omega_c t) \cos(\omega_s t), \quad (5.13)$$

where  $R_{xy,t} = \rho_{xy,t}/t$  is the trilinear contribution of the Hall resistance, and  $t$  is the thickness of the sample. A trigonometry identity is used to obtain

$$V_y(t) = I_0 R_{xy,t} \sin(\omega_c t) \cos(\omega_s t) = \frac{1}{2} I_0 R_{xy,t} [\sin(\omega_c + \omega_s)t + \sin(\omega_c - \omega_s)t]. \quad (5.14)$$

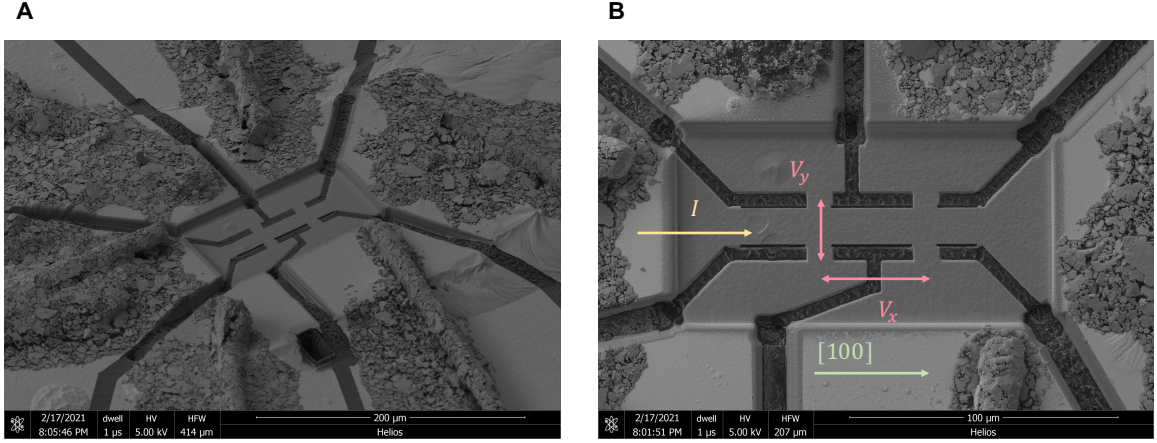


Figure 5.2: (A) Typical microstructure with 6-point-contact geometry. (B) Top view of the microstructure. Labels indicate the current path, and the longitudinal voltage  $V_x$  and the transverse voltage  $V_y$ . These scanning electron microscope pictures were taken inside of the FIB machine by M.D. Bachmann

The signal can be measured using lock-in amplifier to lock in to either of the sideband frequency at  $|\omega_c \pm \omega_s|$ . The measured sideband is

$$S_{xy,t} = \frac{1}{2} I_0 \rho_{xx} g \eta \chi H_z \epsilon_{B_{1g},0} \omega_s. \quad (5.15)$$

By comparing this equation to Eq.5.9, the sideband and the Hall viscosity are related through the following relation:

$$\frac{\partial^2}{\partial \epsilon_{B_{1g}} \partial H_z} \left( \frac{\Delta \rho}{\rho} \right) \Big|_{B_{2g}} \Big|_{H_z = \dot{\epsilon} = 0} \propto \frac{1}{\rho_{xx}} \frac{\partial^2}{\partial f_s \partial H_z} S_{xy} \propto \chi. \quad (5.16)$$

Note here that  $S$  is the X-component of the sideband.

To obtain  $\partial^2 S_{xy} / \partial f_s \partial H_z$ , first, the Hall signal is measured as a function of the magnetic field; this should give a linear dependence of the signal. The slope of the linear fit gives  $\partial S_{xy} / \partial H_z$ . This is repeated with many strain frequencies. This allows us to take the second (partial) derivative of the signal with respect to the magnetic field and strain frequency, i.e.  $\partial^2 S_{xy} / \partial H_z \partial f_s$ . Since the nematic susceptibility has a Curie-Weiss form, one should see this temperature dependence when repeating the measurement at many temperatures close to  $T_S$ .

## 5.4 Experimental setup

Following the discussion from the previous section, the desired geometry is a rectangle with  $[100]$  and  $[010]$  parallel to the side of the rectangle illustrated in Fig.5.1. Current is sourced along the length

of the sample, and transverse and longitudinal voltage can be measured simultaneously. Stress is applied along the [100] direction of the sample. This enables oscillating  $B_{1g}$  strain for measuring the nematic susceptibility, and  $A_{1g}$  and  $B_{1g}$  strain for tuning  $T_S$ .

A preliminary experiment in a bulk sample indicates that the signal is very small. Therefore, it becomes extremely important to have a sample with large resistance and very well controlled electrical contact placement. This necessitated preparations of crystals using Focused Ion Beam (FIB).

Single crystals of  $BaFe_2As_2$  were grown using the method described elsewhere [7, 62]. Sample of thickness less than  $20\mu\text{m}$  was glued onto a piezoelectric stack (*Piezomechanik GmbH* model PSt150/5×5/7 cryo 1) with *Angstrom Bond* AB9110LV epoxy. The [100] crystallographic direction is aligned parallel to the length of the PZT. The sample is milled with FIB using *Helios NanoLab 600i DualBeam* at Stanford Nanoshare facility. The sample preparation process is explained in more detail in Section 2.1.

A typical microstructure is shown in Fig.5.2. The active area (marked by the rectangle) has a typical thickness of  $1\mu\text{m}$ . Compared to the typical thickness of as-cleaved samples of  $\sim 30\mu\text{m}$ , the Hall resistance increases by 30-fold after the milling process. The contact misalignment can be determined by measuring  $V_y/V_x$  with the typical value of less than 1%. A common concern with the microstructure is it can be damaged when a large current is applied due to heating. An appropriate current range suitable for the measurement can be determined by measuring the voltage as a function of current (V-I curve). For  $BaFe_2As_2$  microstructure with a typical dimension of  $100\mu\text{m} \times 20\mu\text{m} \times 1\mu\text{m}$ , the V-I curve exhibits a linear behavior up to more than 10mA. This ensures that there is no significant heating, and the measurement is in the Ohmic region at all time.

Current is sourced by converting the voltage output from *Stanford Research* SR860 to current using *Stanford Research* CS580 Voltage-Controlled Current Source. The voltages across the PZT stack is controlled using *Stanford Research* SR860 Lock-In amplifier and amplified by a factor of 25 through a *Tegam 2350* precision power amplifier. The sideband is measured using the dual mode of the SR860. The measurement was performed in *Quantum Design* Physical Properties Measurement System (PPMS), with the magnetic field up to 14T in both  $+z$  and  $-z$  direction. This allows for up to 28T of magnetic field sweep.

## 5.5 Result and discussion

The measurement is performed in the stoichiometric parent  $BaFe_2As_2$  with  $T_S \approx 132.5\text{K}$ . Figure 5.3 summarizes the results. The X component of the sideband signal from Hall voltage is first antisymmetrized with respect to the field  $S_{xy,t}^{\text{antisym}} = \frac{1}{2}[S_{xy,t}(H_z) - S_{xy,t}(-H_z)]$ . This is done to eliminate any elasto-resistance that may be picked up from contact misalignment<sup>3</sup>.

<sup>3</sup>According to Onsager's reciprocal relation, the magnetoresistivity of a material is an even function of the applied magnetic field [112]. Antisymmetrizing the Hall signal eliminates the contamination from contact misalignment.

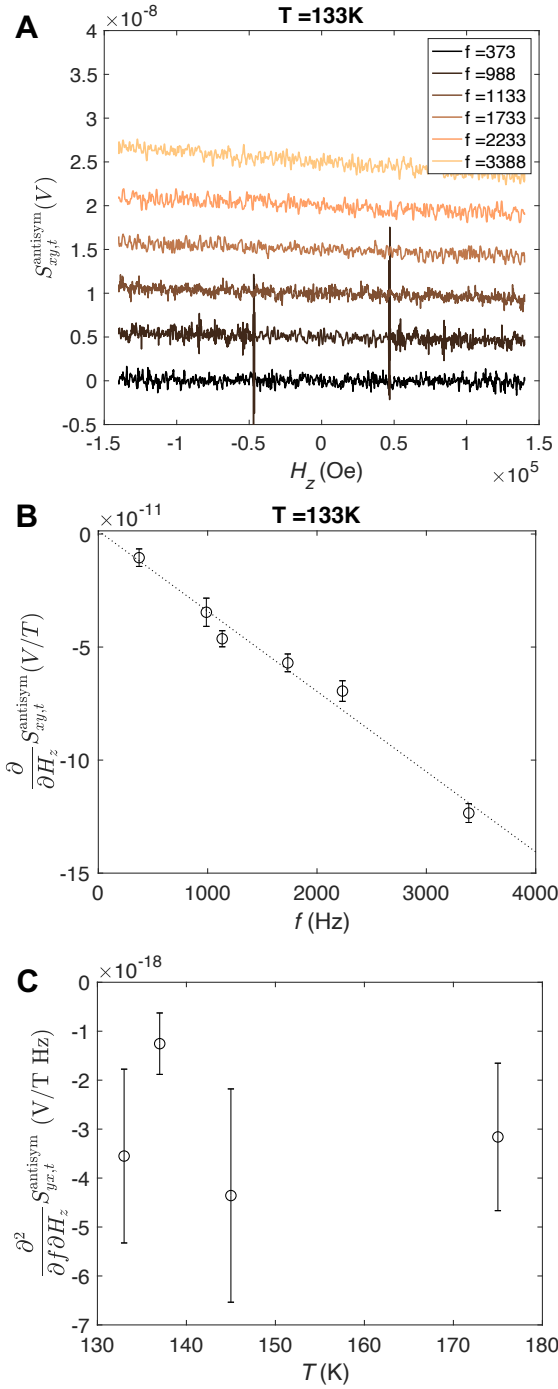


Figure 5.3: (A) The antisymmetrized sideband from the Hall channel. It is linear as a function of the applied magnetic field, and the slope increases as a function of strain frequency. This plot is smoothen using the smoothing spline method in MatLab. (B) The slope  $\frac{\partial}{\partial H_z} S_{xy,t}^{antisym}$  is plotted as a function of strain frequency, revealing a linear dependence. The slope of this plot,  $\frac{\partial^2}{\partial f_s \partial H_z} S_{xy,t}^{antisym}$ , is directly proportional to the Hall viscosity coefficient. (C)  $\frac{\partial^2}{\partial f \partial H_z} S_{xy,t}^{antisym}$  is plotted as a function of temperature. The expected Curie-Weiss temperature dependence was not observed, implying the observed Hall viscosity coefficient may come from other origins.

Figure 5.3A shows the antisymmetrized sideband as a function of the magnetic field at various strain frequencies at 133K, just above the critical temperature  $T_S$  for this sample. It is apparent that  $S_{xy,t}^{\text{antisym}}$  is linearly dependent on  $H_z$ , and the slope is larger for higher strain frequency  $f_s$ . The field derivative  $\left. \frac{\partial}{\partial H_z} S_{xy,t}^{\text{antisym}} \right|_{H_z=0}$  is extracted from each trace by fitting a linear function to the data. This is then plotted as a function of frequency in Fig.5.3B, and it shows a linear frequency dependence. To obtain  $\left. \frac{\partial^2}{\partial f_s \partial H_z} S_{xy,t}^{\text{antisym}} \right|_{H_z, f=0}$ , a linear function is fitted to the field derivative of temperature. The slope is proportional to the Hall viscosity coefficient. The temperature dependence of the Hall viscosity coefficient is obtained by repeating this process at many temperatures. The result is shown in Fig.5.3C. It can be seen that all the data points lie within each other's standard deviation, which is not the anticipated temperature dependence, as the nematic susceptibility is expected to have a Curie-Weiss functional form [17, 47].

Theoretically, the Hall viscosity diverges at  $T_S$ , and the Hall viscosity coefficient should always be observed close to  $T_S$ . However, it is a matter of how close the temperature has to be to  $T_S$  to observe this signal; and it is the trilinear coupling coefficient  $\eta$  that dictates this temperature range. It can, therefore, be inferred from our result that the trilinear coupling coefficient  $\eta$  in this system is extremely small, such that the temperature has to be infinitesimally close  $T_S$  to observe the divergence. Although the the observed signal does not follow the expected temperature dependence in this material, I hope it has future uses in other phases or materials where this type of coupling is large.

Lastly, it shall be noted that, although the signal we observed does not have an expected temperature dependence, it is non-zero. The observation implies that the observed Hall viscosity coefficient may come from other microscopic origins, as it is allowed by symmetry for the conjugate field  $\dot{\epsilon}_{B_{1g}} H_z$  to couple to any other  $B_{2g}$  objects, such as the  $B_{2g}$  phonon mode.

## 5.A Strain response of the PZT

The frequency response of a PZT stack is obtained by measuring induced strain amplitude. This can be done by gluing the strain gauge onto the back of the PZT (see Section 2.2.1 with the amplitude demodulation method). Using the result from Section 2.4, the strain amplitude is calculated from the relation  $\epsilon_{SG} = S_{SG}/C_{SG}$ , where  $S_{SG}$  and  $C_{SG}$  are the sideband and the central band of the strain gauge, respectively. The upper panel of Fig.5.4 shows the strain amplitude induced by a 20V peak-to-peak input to the PZT. This exhibits almost a flat response as a function of frequency, but has a significant temperature dependence, as the strain amplitude is reduced by nearly a quarter 200K to 25K. However, in our temperature range between 135K and 175K, the change in strain amplitude is slight.

The bottom panel of Fig.5.4 shows the phase of the sideband  $S_{SG}$ . The expected phase is  $90^\circ$  (see Section 2.4); however the deviation from that value is observed. At low frequency, this is expected due to the capacitive effect of the PZT. At high frequency, the phase started to deviate, especially at high temperatures. The physical origin of this deviation is unclear as it may cause by many factors such as a high-frequency noise or inductance in the wiring of the cryostat. Nevertheless, this observation establishes the limits of the frequency range to perform this experiment.

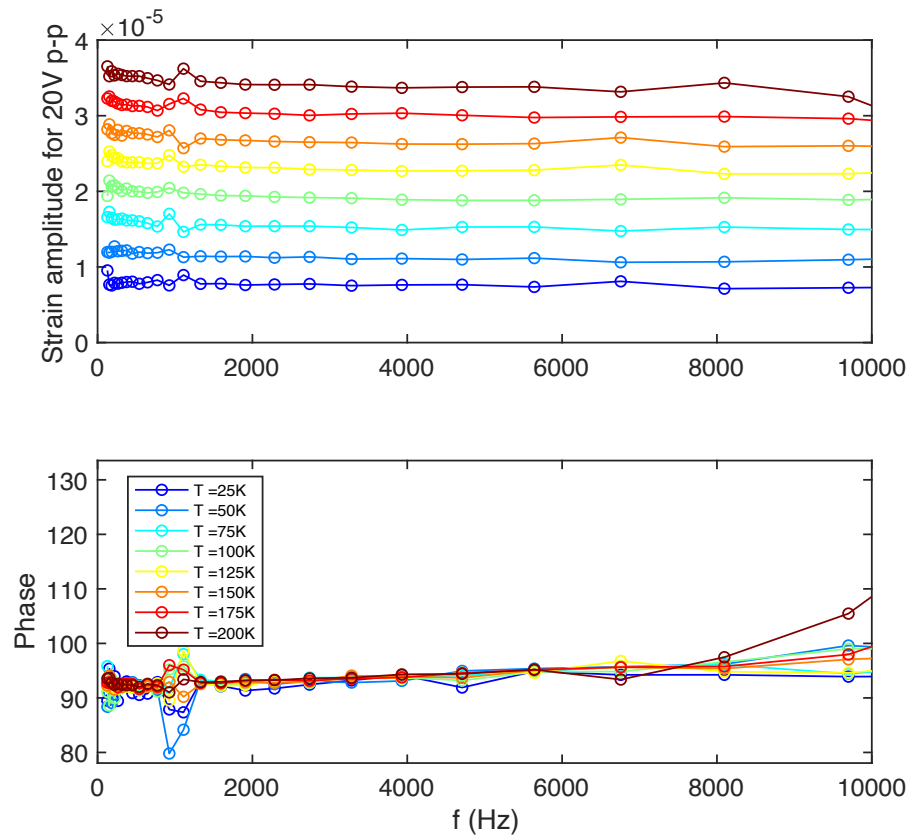


Figure 5.4: Frequency response of the PZT obtained by attaching a strain gauge to the back of the PZT and measured with amplitude demodulation method described in Section 2.4

## 5.B Comments on the strain dependence of the Hall coefficient

As the oscillating stress is applied to the sample, the Hall coefficient will oscillate accordingly. We can approximate the size of this Hall effect using a one-band free electron approximation:

$$R_H(t) = \frac{1}{n_e(t)e} = \frac{\Omega(t)}{Ne}, \quad (5.17)$$

where  $\Omega$  is the volume of the sample, and  $n_e$  and  $N$  are the number density and the number of the electrons, respectively. The fractional change of the measured Hall voltage due to oscillating strain is therefore equal to the fractional change of the sample's volume:

$$\frac{\Delta V_{xy}}{V_{xy}} = \frac{\Delta R_H}{R_H} = \frac{\Delta \Omega}{\Omega}. \quad (5.18)$$

The fractional volume change can be expressed in terms of strain:

$$\frac{\Delta \Omega}{\Omega} = \frac{\Delta x}{x} + \frac{\Delta y}{y} + \frac{\Delta z}{z} = \epsilon_{xx} + \epsilon_{yy} + \epsilon_{zz}. \quad (5.19)$$

This can be expressed in terms of  $\epsilon_{xx}$  and the out of plane Poisson's ratios of the sample,  $\nu' = 0.164$  (see Table 3.1), and the Poisson's ratio of the PZT,  $\nu_P = 1/2.3 = 0.43$  :

$$\frac{\Delta \Omega}{\Omega} = (1 - \nu_P)(1 - \nu')\epsilon_{xx} \sim 0.4\epsilon_{xx}. \quad (5.20)$$

Figure 5.4 shows that the strain amplitude in the  $xx$  component is at 150K is approximately  $3 \times 10^{-5}$ . This translate into the fractional change in volume of approximately  $1.2 \times 10^{-5}$ . Therefore,

$$\Delta V_{xy} \sim 1.2 \times 10^{-5} V_{xy} \quad (5.21)$$

for this strain amplitude. The maximum value of  $V_{xy}$ , measured at 14T and 150K, is approximately  $5 \times 10^{-6}$  for a parent BaFe<sub>2</sub>As<sub>2</sub> sample with a typical microstructure (Fig.5.2). This means that the maximum signal caused by this effect is approximately  $\Delta V_{xy} \sim 6 \times 10^{-11} V$ , which is more than one order of magnitude smaller than the sensitivity of the instrument (*Stanford Research SR860*). Indeed, this effect was not observed in any of our measurement.

## Chapter 6

# Final summary and future works

### 6.1 Summary of this thesis work

My thesis is motivated by the phenomenon of nematic quantum criticality in iron-based superconductors. Understanding the role of electronic nematicity could lead to a more complete understanding of unconventional superconductivity. Because the physical properties in vicinity of a quantum critical point is governed by power laws, it is crucial to have a continuous tuning parameter that can move the system infinitesimally close to the critical point. This motivates me to look for new tuning parameters, and this is presented in Chapter 3. Strain, specifically strain induced by an externally applied stress, is a potential candidate for such tuning parameter, as it can be done in-situ and is essentially a continuous tuning parameter. This experiment investigates the variation of the critical temperature  $T_S$  of the nematic phase transition as strain is induced from two different environments: inside a hydrostatic pressure cell and on a uniaxial stress cell. The two distinct stress environments allow for a full decomposition of in-plane  $A_{1g,1}$  and the out-of-plane  $A_{1g,2}$  symmetry-preserving strains, and the orthogonal antisymmetric  $B_{1g}$  strain. The result shows that  $B_{1g}$  strain is a powerful continuous tuning parameter. Furthermore, it is observed that the  $A_{1g,1}$  and  $A_{1g,2}$  strains work against each other in the hydrostatic environment but work together in the uniaxial stress environment. This makes uniaxial stress a very powerful tool to tune the nematic phase transition.

Chapter 4 utilizes uniaxial stress to investigate the nematic quantum criticality. The response of  $T_S$  to uniaxial stress is systematically studied in various compositions of  $\text{Ba}(\text{Fe}_{1-x}\text{Co}_x)_2\text{As}_2$  close to the putative quantum critical point. It is observed that uniaxial stress becomes more effective close to the putative quantum critical point. By symmetry decompose the uniaxial stress into  $A_{1g}$  and  $B_{1g}$  strains, it is found that this phenomenon is caused by the power-law behavior of  $T_S$  as a function of non-thermal tuning parameters. This provides the first direct evidence for the nematic quantum critical point in the form of power-law behavior. The power-law regime exists over a remarkably wide range of composition and temperature, extending over the majority of the superconducting

dome for these underdoped compositions. This empirically establish that the superconductor is not only born out of a metal that hosts strong nematic fluctuations but specifically is born from a metal that exhibits quantum critical nematic fluctuations.

The realization that uniaxial stress is an excellent continuous tuning parameter close to the quantum critical point motivates us to measure the nematic susceptibility while tuning the system with uniaxial stress. In the final experiment (Chapter 5), I present a new technique to measure the nematic susceptibility with a novel conjugate field  $\dot{\epsilon}_{B_{1g}} H_z$ , which is a combination of a time-varying  $B_{1g}$  strain and a magnetic field. This combined conjugate field belongs to the  $B_{2g}$  irreducible representation, and thus can couple to the  $B_{2g}$  nematic in a bilinear fashion. In theory, this allows for the measurement of nematic susceptibility while tuning the system with  $A_{1g}$  and  $B_{1g}$  strains. We measured a non-zero Hall viscosity coefficient, a quantity that is a proxy for nematic susceptibility. However, it does not have the anticipated temperature dependence. This implies that the coupling constant between the combined conjugate field and the nematic order is small, and the measured Hall viscosity coefficient is dominated by coupling to other non-critical degrees of freedom. Even though this result suggests that this technique is not applicable for this material, it is nevertheless an important technique that may be applied to other material systems.

## 6.2 Future outlooks

Although this thesis has pushed the boundary of establishing the nematic quantum critical phenomena, much work is to be done to understand the complete picture of this unconventional superconductor. A question that immediately follows is what happens to the quantum critical nematic fluctuations under the superconducting dome. Specifically, whether the nematic phase transition persists, and if so, does the power-law behavior also persists, and what is the critical exponent of that power law. A difficult part of that experiment is the lack of probe to detect the phase transition under the superconducting dome, as all the transport measurements are rendered ineffective, and the signal from heat capacity measurement is also heavily blurred by the disorder effects. There are, however, a recent development that could allow this measurement. AC elastocaloric effect, developed by M.S. Ikeda in our group [61], has the potential. It is a thermodynamic probe that is not obstructed by the presence of superconductivity and has proven to have an excellent signal to noise ratio - allowing the measurement of specific heat anomalies even in highly disordered materials.

One may also take an alternative route and extend the normal state down to lower temperatures by suppressing the superconductivity using, for instance, a magnetic field. Some work has already been done, led by J.C. Palmstrom and J.A.W. Straquadine of our group [113, 104], using a high magnetic field up to 65T to partially suppress the superconductivity and measuring the nematic susceptibility in that region.

Another exciting avenue that can be explored with this perspective is in other materials in

the family of iron-based superconductors that do not exhibit the usual phase diagram, such as  $\text{Ba}(\text{Fe}_{1-x}\text{Cu}_x)_2\text{As}_2$  and  $\text{FeSe}_{1-x}\text{S}_x$ . The phase diagram of  $\text{Ba}(\text{Fe}_{1-x}\text{Cu}_x)_2\text{As}_2$  is mostly similar to  $\text{Ba}(\text{Fe}_{1-x}\text{Co}_x)_2\text{As}_2$ , where the nematic and magnetic states are suppressed and superconductivity emerges [114]. The big difference is the superconducting dome is much smaller. It peaks at  $\sim 1\text{K}$  at the optimally doped composition - raising the question of whether there are quantum critical fluctuations in the system and what role disorder plays in a quantum critical system.  $\text{FeSe}_{1-x}\text{S}_x$  presents a unique phase diagram [115], where the electronic nematic phase is present by itself without the accompaniment of a magnetic phase. The parent  $\text{FeSe}$  compound superconducts at  $\sim 9\text{K}$ , and remains essentially constant when the nematic phase is suppressed. This indicates a different type of interplay between electronic nematicity and superconductivity. Studying these materials may help elucidate another big question: how much does the electronic nematicity influence the superconductivity.

# Bibliography

- [1] Michael R. Norman. The challenge of unconventional superconductivity. *Science*, 332(6026):196–200, 2011.
- [2] T. Shibauchi, A. Carrington, and Y. Matsuda. A quantum critical point lying beneath the superconducting dome in iron pnictides. *Ann. Rev. of Cond. Matter Phys.*, 5(1):113–135, 2014.
- [3] Xingye Lu, H. Gretarsson, Rui Zhang, Xuerong Liu, Huiqian Luo, Wei Tian, Mark Laver, Z. Yamani, Young-June Kim, A. H. Nevidomskyy, Qimiao Si, and Pengcheng Dai. Avoided quantum criticality and magnetoelastic coupling in  $\text{BaFe}_{2-x}\text{Ni}_x\text{As}_2$ . *Phys. Rev. Lett.*, 110:257001, Jun 2013.
- [4] Xingye Lu, David W. Tam, Chenglin Zhang, Huiqian Luo, Meng Wang, Rui Zhang, Leland W. Harriger, T. Keller, B. Keimer, L.-P. Regnault, Thomas A. Maier, and Pengcheng Dai. Short-range cluster spin glass near optimal superconductivity in  $\text{BaFe}_{2-x}\text{Ni}_x\text{As}_2$ . *Phys. Rev. B*, 90:024509, Jul 2014.
- [5] Yoichi Kamihara, Takumi Watanabe, Masahiro Hirano, and Hideo Hosono. Iron-based layered superconductor  $\text{LaO}_{1-x}\text{F}_x\text{FeAs}$  ( $x = 0.05 - 0.12$ ) with  $T_c = 26$  K. *Journal of the American Chemical Society*, 130(11):3296–3297, 2008. PMID: 18293989.
- [6] Qimiao Si, Rong Yu, and Elihu Abrahams. High-temperature superconductivity in iron pnictides and chalcogenides. *Nature Reviews Materials*, 1(4):16017, Mar 2016.
- [7] Jiun-Haw Chu, James G. Analytis, Chris Kucharczyk, and Ian R. Fisher. Determination of the phase diagram of the electron-doped superconductor  $\text{Ba}(\text{Fe}_{1-x}\text{Co}_x)_2\text{As}_2$ . *Phys. Rev. B*, 79:014506, Jan 2009.
- [8] Takehiro Yamazaki, Nao Takeshita, Ryosuke Kobayashi, Hideto Fukazawa, Yoh Kohori, Kunihiro Kihou, Chul-Ho Lee, Hijiri Kito, Akira Iyo, and Hiroshi Eisaki. Appearance of pressure-induced superconductivity in  $\text{BaFe}_2\text{As}_2$  under hydrostatic conditions and its extremely high sensitivity to uniaxial stress. *Phys. Rev. B*, 81:224511, Jun 2010.

- [9] Marianne Rotter, Marcus Tegel, and Dirk Johrendt. Superconductivity at 38K in the iron arsenide  $(\text{Ba}_{1-x}\text{K}_x)\text{Fe}_2\text{As}_2$ . *Phys. Rev. Lett.*, 101:107006, Sep 2008.
- [10] K Haule and G Kotliar. Coherence–incoherence crossover in the normal state of iron oxypnictides and importance of hund's rule coupling. *New Journal of Physics*, 11(2):025021, feb 2009.
- [11] Antoine Georges, Luca de' Medici, and Jernej Mravlje. Strong correlations from hunds coupling. *Annual Review of Condensed Matter Physics*, 4(1):137–178, 2013.
- [12] M. Yi, D. H. Lu, J. G. Analytis, J.-H. Chu, S.-K. Mo, R.-H. He, R. G. Moore, X. J. Zhou, G. F. Chen, J. L. Luo, N. L. Wang, Z. Hussain, D. J. Singh, I. R. Fisher, and Z.-X. Shen. Electronic structure of the  $\text{BaFe}_2\text{As}_2$  family of iron-pnictide superconductors. *Phys. Rev. B*, 80:024515, Jul 2009.
- [13] P J Hirschfeld, M M Korshunov, and I I Mazin. Gap symmetry and structure of fe-based superconductors. *Reports on Progress in Physics*, 74(12):124508, oct 2011.
- [14] S Graser, T A Maier, P J Hirschfeld, and D J Scalapino. Near-degeneracy of several pairing channels in multiorbital models for the fe pnictides. *New Journal of Physics*, 11(2):025016, feb 2009.
- [15] James G. Analytis, H-H. Kuo, Ross D. McDonald, Mark Wartenbe, P. M. C. Rourke, N. E. Hussey, and I. R. Fisher. Transport near a quantum critical point in  $\text{BaFe}_2(\text{As}_{1-x}\text{P}_x)_2$ . *Nature Physics*, 10(3):194–197, 2014.
- [16] S. Nandi, M. G. Kim, A. Kreyssig, R. M. Fernandes, D. K. Pratt, A. Thaler, N. Ni, S. L. Bud'ko, P. C. Canfield, J. Schmalian, R. J. McQueeney, and A. I. Goldman. Anomalous suppression of the orthorhombic lattice distortion in superconducting  $\text{Ba}(\text{Fe}_{1-x}\text{Co}_x)_2\text{As}_2$  Single Crystals. *Phys. Rev. Lett.*, 104:057006, Feb 2010.
- [17] Jiun-Haw Chu, Hsueh-Hui Kuo, James G. Analytis, and Ian R. Fisher. Divergent nematic susceptibility in an iron arsenide superconductor. *Science*, 337(6095):710–712, 2012.
- [18] Anna E. Bhmer and Christoph Meingast. Electronic nematic susceptibility of iron-based superconductors. *Comptes Rendus Physique*, 17(1):90 – 112, 2016. Iron-based superconductors / Supraconducteurs base de fer.
- [19] Morten H. Christensen, Jian Kang, Brian M. Andersen, Ilya Eremin, and Rafael M. Fernandes. Spin reorientation driven by the interplay between spin-orbit coupling and hund's rule coupling in iron pnictides. *Phys. Rev. B*, 92:214509, Dec 2015.
- [20] Rafael M Fernandes and Andrey V Chubukov. Low-energy microscopic models for iron-based superconductors: a review. *Reports on Progress in Physics*, 80(1):014503, nov 2016.

- [21] Elena Bascones, Beln Valenzuela, and Maria Jos Caldern. Magnetic interactions in iron superconductors: A review. *Comptes Rendus Physique*, 17(1):36–59, 2016. Iron-based superconductors / Supraconducteurs base de fer.
- [22] M D Lumsden and A D Christianson. Magnetism in fe-based superconductors. *Journal of Physics: Condensed Matter*, 22(20):203203, apr 2010.
- [23] Pengcheng Dai, Jiangping Hu, and Elbio Dagotto. Magnetism and its microscopic origin in iron-based high-temperature superconductors. *Nature Physics*, 8(10):709–718, Oct 2012.
- [24] REN Zhi-An, LU Wei, YANG Jie, YI Wei, SHEN Xiao-Li, LI Zheng-Cai, CHE Guang-Can, DONG Xiao-Li, SUN Li-Ling, ZHOU Fang, and ZHAO Zhong-Xian. Superconductivity at 55K in iron-based f-doped layered quaternary compound  $\text{SmO}_{1-x}\text{F}_x\text{FeAs}$ . *Chinese Physics Letters*, 25(6):2215–2216, 2008.
- [25] Jian-Feng Ge, Zhi-Long Liu, Canhua Liu, Chun-Lei Gao, Dong Qian, Qi-Kun Xue, Ying Liu, and Jin-Feng Jia. Superconductivity above 100K in single-layer fese films on doped  $\text{SrTiO}_3$ . *Nature Materials*, 14(3):285–289, Mar 2015.
- [26] L. Boeri, O. V. Dolgov, and A. A. Golubov. Is lafeaso $_{1-x}$ f $_x$  an electron-phonon superconductor? *Phys. Rev. Lett.*, 101:026403, Jul 2008.
- [27] Andrey Chubukov. Pairing mechanism in fe-based superconductors. *Annual Review of Condensed Matter Physics*, 3(1):57–92, 2012.
- [28] Dmytro S. Inosov. Spin fluctuations in iron pnictides and chalcogenides: From antiferromagnetism to superconductivity. *Comptes Rendus Physique*, 17(1):60–89, 2016. Iron-based superconductors / Supraconducteurs base de fer.
- [29] M. A. Tanatar, J.-Ph. Reid, H. Shakeripour, X. G. Luo, N. Doiron-Leyraud, N. Ni, S. L. Bud’ko, P. C. Canfield, R. Prozorov, and Louis Taillefer. Doping dependence of heat transport in the iron-arsenide superconductor  $\text{Ba}(\text{Fe}_{1-x}\text{Co}_x)_2\text{As}_2$ : From isotropic to a strongly  $k$ -dependent gap structure. *Phys. Rev. Lett.*, 104:067002, Feb 2010.
- [30] I.I. Mazin and J. Schmalian. Pairing symmetry and pairing state in ferropnictides: Theoretical overview. *Physica C: Superconductivity*, 469(9):614–627, 2009. Superconductivity in Iron-Pnictides.
- [31] Jiun-Haw Chu, James G. Analytis, Kristiaan De Greve, Peter L. McMahon, Zahirul Islam, Yoshihisa Yamamoto, and Ian R. Fisher. In-plane resistivity anisotropy in an underdoped iron arsenide superconductor. *Science*, 329(5993):824–826, 2010.

- [32] A. E. Böhmer, P. Burger, F. Hardy, T. Wolf, P. Schweiss, R. Fromknecht, M. Reinecker, W. Schranz, and C. Meingast. Nematic susceptibility of hole-doped and electron-doped  $\text{BaFe}_2\text{As}_2$  iron-based superconductors from shear modulus measurements. *Phys. Rev. Lett.*, 112:047001, Jan 2014.
- [33] Pierre Massat, Donato Farina, Indranil Paul, Sandra Karlsson, Pierre Strobel, Pierre Toulemonde, Marie-Aude Méasson, Maximilien Cazayous, Alain Sacuto, Shigeru Kasahara, Takasada Shibauchi, Yuji Matsuda, and Yann Gallais. Charge-induced nematicity in FeSe. *Proceedings of the National Academy of Sciences*, 113(33):9177–9181, 2016.
- [34] Y. Gallais, R. M. Fernandes, I. Paul, L. Chauvière, Y.-X. Yang, M.-A. Méasson, M. Cazayous, A. Sacuto, D. Colson, and A. Forget. Observation of incipient charge nematicity in  $\text{Ba}(\text{Fe}_{1-x}\text{Co}_x)_2\text{As}_2$ . *Phys. Rev. Lett.*, 111:267001, Dec 2013.
- [35] V. K. Thorsmølle, M. Khodas, Z. P. Yin, Chenglin Zhang, S. V. Carr, Pengcheng Dai, and G. Blumberg. Critical quadrupole fluctuations and collective modes in iron pnictide superconductors. *Phys. Rev. B*, 93:054515, Feb 2016.
- [36] Eduardo Fradkin, Steven A. Kivelson, Michael J. Lawler, James P. Eisenstein, and Andrew P. Mackenzie. Nematic fermi fluids in condensed matter physics. *Annual Review of Condensed Matter Physics*, 1(1):153–178, 2010.
- [37] Youichi Yamakawa, Seiichiro Onari, and Hiroshi Kontani. Nematicity and magnetism in fese and other families of fe-based superconductors. *Phys. Rev. X*, 6:021032, Jun 2016.
- [38] Rafael M. Fernandes, Peter P. Orth, and Jrg Schmalian. Intertwined vestigial order in quantum materials: Nematicity and beyond. *Annual Review of Condensed Matter Physics*, 10(1):133–154, 2019.
- [39] S.-H. Baek, D. V. Efremov, J. M. Ok, J. S. Kim, Jeroen van den Brink, and B. Büchner. Orbital-driven nematicity in fese. *Nature Materials*, 14(2):210–214, Feb 2015.
- [40] P. Zhang, T. Qian, P. Richard, X. P. Wang, H. Miao, B. Q. Lv, B. B. Fu, T. Wolf, C. Meingast, X. X. Wu, Z. Q. Wang, J. P. Hu, and H. Ding. Observation of two distinct  $d_{xz}/d_{yz}$  band splittings in fese. *Phys. Rev. B*, 91:214503, Jun 2015.
- [41] H. Pfau, S. D. Chen, M. Yi, M. Hashimoto, C. R. Rotundu, J. C. Palmstrom, T. Chen, P.-C. Dai, J. Straquadine, A. Hristov, R. J. Birgeneau, I. R. Fisher, D. Lu, and Z.-X. Shen. Momentum dependence of the nematic order parameter in iron-based superconductors. *Phys. Rev. Lett.*, 123:066402, Aug 2019.
- [42] Max A. Metlitski, David F. Mross, Subir Sachdev, and T. Senthil. Cooper pairing in non-fermi liquids. *Phys. Rev. B*, 91:115111, Mar 2015.

- [43] T. A. Maier and D. J. Scalapino. Pairing interaction near a nematic quantum critical point of a three-band  $\text{CuO}_2$  model. *Phys. Rev. B*, 90:174510, Nov 2014.
- [44] Samuel Lederer, Yoni Schattner, Erez Berg, and Steven A. Kivelson. Superconductivity and non-Fermi liquid behavior near a nematic quantum critical point. *Proceedings of the National Academy of Sciences*, 114(19):4905–4910, 2017.
- [45] S. Lederer, Y. Schattner, E. Berg, and S. A. Kivelson. Enhancement of superconductivity near a nematic quantum critical point. *Phys. Rev. Lett.*, 114:097001, Mar 2015.
- [46] Cyril Proust and Louis Taillefer. The remarkable underlying ground states of cuprate superconductors. *Annual Review of Condensed Matter Physics*, 10(1):409–429, 2019.
- [47] Hsueh-Hui Kuo, Jiun-Haw Chu, Johanna C. Palmstrom, Steven A. Kivelson, and Ian R. Fisher. Ubiquitous signatures of nematic quantum criticality in optimally doped Fe-based superconductors. *Science*, 352(6288):958–962, 2016.
- [48] P. Walmsley, C. Putzke, L. Malone, I. Guillamón, D. Vignolles, C. Proust, S. Badoux, A. I. Coldea, M. D. Watson, S. Kasahara, Y. Mizukami, T. Shibauchi, Y. Matsuda, and A. Carrington. Quasiparticle mass enhancement close to the quantum critical point in  $\text{BaFe}_2(\text{As}_{1-x}\text{P}_x)_2$ . *Phys. Rev. Lett.*, 110:257002, Jun 2013.
- [49] Subir Sachdev. *Quantum Phase Transitions*. Cambridge University Press, 2 edition, 2011.
- [50] T. Kissikov, R. Sarkar, M. Lawson, B. T. Bush, E. I. Timmons, M. A. Tanatar, R. Prozorov, S. L. Bud'ko, P. C. Canfield, R. M. Fernandes, W. F. Goh, W. E. Pickett, and N. J. Curro. Local nematic susceptibility in stressed  $\text{BaFe}_2\text{As}_2$  from NMR electric field gradient measurements. *Phys. Rev. B*, 96:241108, Dec 2017.
- [51] Arthur S. Nowick. *Crystal Properties via Group Theory*. Cambridge University Press, 1995.
- [52] <https://www.chemtube3d.com/xf4-symmetry-d4h/>.
- [53] Akash V. Maharaj, Elliott W. Rosenberg, Alexander T. Hristov, Erez Berg, Rafael M. Fernandes, Ian R. Fisher, and Steven A. Kivelson. Transverse fields to tune an Ising-nematic quantum phase transition. *Proceedings of the National Academy of Sciences*, 114(51):13430–13434, 2017.
- [54] M.C. Shapiro. *Elastoresistivity as a Probe of Electronically Driven Rotational Symmetry Breaking and Its Application to the Hidden Order State in  $\text{URu}_2\text{Si}_2$* . PhD thesis, 2016.
- [55] M. C. Shapiro, Patrik Hlobil, A. T. Hristov, Akash V. Maharaj, and I. R. Fisher. Symmetry constraints on the elastoresistivity tensor. *Phys. Rev. B*, 92:235147, Dec 2015.

- [56] Matthias S. Ikeda, Thanapat Worasaran, Elliott W. Rosenberg, Johanna C. Palmstrom, Steven A. Kivelson, and Ian R. Fisher. Elastocaloric signature of nematic fluctuations, arXiv:2101.00080.
- [57] Alexander T. Hristov, Johanna C. Palmstrom, Joshua A. W. Straquadine, Tyler A. Merz, Harold Y. Hwang, and Ian R. Fisher. Measurement of elastoresistivity at finite frequency by amplitude demodulation. *Review of Scientific Instruments*, 89(10):103901, 2018.
- [58] J. C. Palmstrom, A. T. Hristov, S. A. Kivelson, J.-H. Chu, and I. R. Fisher. Critical divergence of the symmetric ( $A_{1g}$ ) nonlinear elastoresistance near the nematic transition in an iron-based superconductor. *Phys. Rev. B*, 96:205133, Nov 2017.
- [59] M. C. Shapiro, A. T. Hristov, J. C. Palmstrom, Jiun-Haw Chu, and I. R. Fisher. Measurement of the  $B_{1g}$  and  $B_{2g}$  components of the elastoresistivity tensor for tetragonal materials via transverse resistivity configurations. *Review of Scientific Instruments*, 87(6):063902, 2016.
- [60] Michael E. Fisher and J. S. Langer. Resistive anomalies at magnetic critical points. *Phys. Rev. Lett.*, 20:665–668, Mar 1968.
- [61] M. S. Ikeda, J. A. W. Straquadine, A. T. Hristov, T. Worasaran, J. C. Palmstrom, M. Sorensen, P. Walmsley, and I. R. Fisher. AC elastocaloric effect as a probe for thermodynamic signatures of continuous phase transitions. *Review of Scientific Instruments*, 90(8):083902, 2019.
- [62] Johanna C. Palmstrom. *Elastoresistance of Iron-Based Superconductors*. PhD thesis, 2020.
- [63] Maja Bachmann. *Manipulating Anisotropic Transport and Superconductivity by Focused Ion Beam Microstructuring*. PhD thesis, 01 2020.
- [64] Clifford W. Hicks, Mark E. Barber, Stephen D. Edkins, Daniel O. Brodsky, and Andrew P. Mackenzie. Piezoelectric-based apparatus for strain tuning. *Review of Scientific Instruments*, 85(6):065003, 2014.
- [65] M. S. Ikeda, T. Worasaran, J. C. Palmstrom, J. A. W. Straquadine, P. Walmsley, and I. R. Fisher. Symmetric and antisymmetric strain as continuous tuning parameters for electronic nematic order. *Phys. Rev. B*, 98:245133, Dec 2018.
- [66] M. S. Torikachvili, S. K. Kim, E. Colombier, S. L. Budko, and P. C. Canfield. Solidification and loss of hydrostaticity in liquid media used for pressure measurements. *Review of Scientific Instruments*, 86(12):123904, 2015.
- [67] T.F. Smith, C.W. Chu, and M.B. Maple. Superconducting manometers for high pressure measurement at low temperature. *Cryogenics*, 9(1):53 – 56, 1969.

- [68] J. D. Thompson. Lowtemperature pressure variations in a selfclamping pressure cell. *Review of Scientific Instruments*, 55(2):231–234, 1984.
- [69] U. Karahasanovic and J. Schmalian. Elastic coupling and spin-driven nematicity in iron-based superconductors. *Phys. Rev. B*, 93:064520, Feb 2016.
- [70] I. Paul and M. Garst. Lattice effects on nematic quantum criticality in metals. *Phys. Rev. Lett.*, 118:227601, Jun 2017.
- [71] Alexander T. Hristov, Matthias S. Ikeda, Johanna C. Palmstrom, Philip Walmsley, and Ian R. Fisher. Elastoresistive and elastocaloric anomalies at magnetic and electronic-nematic critical points. *Phys. Rev. B*, 99:100101, Mar 2019.
- [72] Thanapat Worasaran, Matthias S. Ikeda, Johanna C. Palmstrom, Joshua A. W. Straquadine, Steven A. Kivelson, and Ian R. Fisher. Nematic quantum criticality in an Fe-based superconductor revealed by strain-tuning. *Science*, 372(6545):973–977, 2021.
- [73] Hsueh-Hui Kuo, Maxwell C. Shapiro, Scott C. Riggs, and Ian R. Fisher. Measurement of the elastoresistivity coefficients of the underdoped iron arsenide  $\text{Ba}(\text{Fe}_{0.975}\text{Co}_{0.025})_2\text{As}_2$ . *Phys. Rev. B*, 88:085113, Aug 2013.
- [74] Rafael M Fernandes and Jrg Schmalian. Manifestations of nematic degrees of freedom in the magnetic, elastic, and superconducting properties of the iron pnictides. *Superconductor Science and Technology*, 25(8):084005, jul 2012.
- [75] R. M. Fernandes, A. V. Chubukov, and J. Schmalian. What drives nematic order in iron-based superconductors? *Nature Physics*, 10:97, January 2014.
- [76] T.-M. Chuang, M. P. Allan, Jinho Lee, Yang Xie, Ni Ni, S. L. Bud’ko, G. S. Boebinger, P. C. Canfield, and J. C. Davis. Nematic electronic structure in the “parent” state of the iron-based superconductor  $\text{Ca}(\text{Fe}_{1-x}\text{Co}_x)_2\text{As}_2$ . *Science*, 327(5962):181–184, 2010.
- [77] Suguru Hosoi, Kohei Matsuura, Kousuke Ishida, Hao Wang, Yuta Mizukami, Tatsuya Watashige, Shigeru Kasahara, Yuji Matsuda, and Takasada Shibauchi. Nematic quantum critical point without magnetism in  $\text{FeSe}_{1-x}\text{S}_x$  superconductors. *Proceedings of the National Academy of Sciences*, 113(29):8139–8143, 2016.
- [78] A. J. Achkar, M. Zwiebler, Christopher McMahan, F. He, R. Sutarto, Isaiah Djianto, Zhihao Hao, Michel J. P. Gingras, M. Hücker, G. D. Gu, A. Revcolevschi, H. Zhang, Y.-J. Kim, J. Geck, and D. G. Hawthorn. Nematicity in stripe-ordered cuprates probed via resonant x-ray scattering. *Science*, 351(6273):576–578, 2016.
- [79] J. Wu, A. T. Bollinger, X. He, and I. Božović. Spontaneous breaking of rotational symmetry in copper oxide superconductors. *Nature*, 547:432, July 2017.

- [80] Yoichi Ando, Kouji Segawa, Seiki Komiya, and A. N. Lavrov. Electrical resistivity anisotropy from self-organized one dimensionality in high-temperature superconductors. *Phys. Rev. Lett.*, 88:137005, Mar 2002.
- [81] V. Hinkov, D. Haug, B. Fauqué, P. Bourges, Y. Sidis, A. Ivanov, C. Bernhard, C. T. Lin, and B. Keimer. Electronic liquid crystal state in the high-temperature superconductor  $\text{YBa}_2\text{Cu}_3\text{O}_{6.45}$ . *Science*, 319(5863):597–600, 2008.
- [82] R. Daou, J. Chang, David LeBoeuf, Olivier Cyr-Choinire, Francis Lalibert, Nicolas Doiron-Leyraud, B. J. Ramshaw, Ruixing Liang, D. A. Bonn, W. N. Hardy, and Louis Taillefer. Broken rotational symmetry in the pseudogap phase of a high- $T_c$  superconductor. *Nature*, 463:519, January 2010.
- [83] O. Cyr-Choinière, G. Grissonnanche, S. Badoux, J. Day, D. A. Bonn, W. N. Hardy, R. Liang, N. Doiron-Leyraud, and Louis Taillefer. Two types of nematicity in the phase diagram of the cuprate superconductor  $\text{YBa}_2\text{Cu}_3\text{O}_y$ . *Phys. Rev. B*, 92:224502, Dec 2015.
- [84] Kazuhiro Fujita, Mohammad H. Hamidian, Stephen D. Edkins, Chung Koo Kim, Yuhki Kohsaka, Masaki Azuma, Mikio Takano, Hidenori Takagi, Hiroshi Eisaki, Shin-ichi Uchida, Andrea Allais, Michael J. Lawler, Eun-Ah Kim, Subir Sachdev, and J. C. Séamus Davis. Direct phase-sensitive identification of a d-form factor density wave in underdoped cuprates. *Proceedings of the National Academy of Sciences*, 111(30):E3026–E3032, 2014.
- [85] S. A. Kivelson, E. Fradkin, and V. J. Emery. Electronic liquid-crystal phases of a doped Mott insulator. *Nature*, 393:550, June 1998.
- [86] Yong Baek Kim and Hae-Young Kee. Pairing instability in a nematic fermi liquid. *Journal of Physics: Condensed Matter*, 16(18):3139, 2004.
- [87] Laimei Nie, Akash V. Maharaj, Eduardo Fradkin, and Steven A. Kivelson. Vestigial nematicity from spin and/or charge order in the cuprates. *Phys. Rev. B*, 96:085142, Aug 2017.
- [88] Chetan Dhital, Z. Yamani, Wei Tian, J. Zeretsky, A. S. Sefat, Ziqiang Wang, R. J. Birge-neau, and Stephen D. Wilson. Effect of uniaxial strain on the structural and magnetic phase transitions in  $\text{BaFe}_2\text{As}_2$ . *Phys. Rev. Lett.*, 108:087001, Feb 2012.
- [89] Xingye Lu, Kuo-Feng Tseng, T. Keller, Wenliang Zhang, Ding Hu, Yu Song, Haoran Man, J. T. Park, Huiqian Luo, Shiliang Li, Andriy H. Nevidomskyy, and Pengcheng Dai. Impact of uniaxial pressure on structural and magnetic phase transitions in electron-doped iron pnictides. *Phys. Rev. B*, 93:134519, Apr 2016.
- [90] T. Kissikov, R. Sarkar, M. Lawson, B. T. Bush, E. I. Timmons, M. A. Tanatar, R. Prozorov, S. L. Budko, P. C. Canfield, R. M. Fernandes, and N. J. Curro. Uniaxial strain control of

- spin-polarization in multicomponent nematic order of  $\text{BaFe}_2\text{As}_2$ . *Nature Communications*, 9(1):1058, March 2018.
- [91] M. S. da Luz, J. J. Neumeier, R. K. Bollinger, A. S. Sefat, M. A. McGuire, R. Jin, B. C. Sales, and D. Mandrus. High-resolution measurements of the thermal expansion of superconducting co-doped  $\text{BaFe}_2\text{As}_2$ . *Phys. Rev. B*, 79:214505, 2009.
- [92] M. Yoshizawa and S. Simayi. Anomalous elastic behavior and its correlation with superconductivity in iron-based superconductor  $\text{Ba}(\text{Fe}_{1-x}\text{Co}_x)_2\text{As}_2$ . *Modern Physics Letters B*, 26(19):1230011, 2012.
- [93] Christoph Meingast, Frédéric Hardy, Rolf Heid, Peter Adelman, Anna Böhmer, Philipp Burger, Doris Ernst, Rainer Fromknecht, Peter Schweiss, and Thomas Wolf. Thermal expansion and Grüneisen parameters of  $\text{Ba}(\text{Fe}_{1-x}\text{Co}_x)_2\text{As}_2$ : A thermodynamic quest for quantum criticality. *Phys. Rev. Lett.*, 108:177004, Apr 2012.
- [94] A. E. Böhmer, A. Sapkota, A. Kreyssig, S. L. Bud'ko, G. Drachuck, S. M. Saunders, A. I. Goldman, and P. C. Canfield. Effect of biaxial strain on the phase transitions of  $\text{Ca}(\text{Fe}_{1-x}\text{Co}_x)_2\text{As}_2$ . *Phys. Rev. Lett.*, 118:107002, Mar 2017.
- [95] W. H. Warren Jr. and W. G. Bader. Superconductivity measurements in solders commonly used for low temperature research. *Review of Scientific Instruments*, 40(1):180–182, 1969.
- [96] R. J. Corruccini and J. J. Gniewek. *Thermal Expansion of Technical Solids at Low Temperatures - A Compilation from the Literature*. United States Department of Commerce, Washington 25, D.C., 1961.
- [97] J. D. Thompson. Low temperature pressure variations in a self clamping pressure cell. *Review of Scientific Instruments*, 55(2):231–234, 1984.
- [98] G. B. de Souza, F. C. Serbena, A. R. Jurelo, S. A. da Silva, L. B. L. G. Pinheiro, F. T. Dias, A. Mikowski, S. L. Bud'ko, A. Thaler, and P. C. Canfield. On the determination of hardness and elastic modulus in  $\text{BaFe}_2\text{As}_2$  lamellar-like material. *Journal of Materials Research*, 31(10):1413, 2016.
- [99] Laimei Nie, Gilles Tarjus, and Steven Allan Kivelson. Quenched disorder and vestigial nematicity in the pseudogap regime of the cuprates. *Proceedings of the National Academy of Sciences*, 111(22):7980–7985, 2014.
- [100] Sourin Mukhopadhyay, Rahul Sharma, Chung Koo Kim, Stephen D. Edkins, Mohammad H. Hamidian, Hiroshi Eisaki, Shin-ichi Uchida, Eun-Ah Kim, Michael J. Lawler, Andrew P. Mackenzie, J. C. Séamus Davis, and Kazuhiro Fujita. Evidence for a vestigial nematic state in

- the cuprate pseudogap phase. *Proceedings of the National Academy of Sciences*, 116(27):13249–13254, 2019.
- [101] K. Hashimoto, K. Cho, T. Shibauchi, S. Kasahara, Y. Mizukami, R. Katsumata, Y. Tsuruhara, T. Terashima, H. Ikeda, M. A. Tanatar, H. Kitano, N. Salovich, R. W. Giannetta, P. Walmsley, A. Carrington, R. Prozorov, and Y. Matsuda. A sharp peak of the zero-temperature penetration depth at optimal composition in  $\text{BaFe}_2(\text{As}_{1-x}\text{P}_x)_2$ . *Science*, 336(6088):1554–1557, 2012.
- [102] H. Shishido, A. F. Bangura, A. I. Coldea, S. Tonegawa, K. Hashimoto, S. Kasahara, P. M. C. Rourke, H. Ikeda, T. Terashima, R. Settai, Y. Ōnuki, D. Vignolles, C. Proust, B. Vignolle, A. McCollam, Y. Matsuda, T. Shibauchi, and A. Carrington. Evolution of the fermi surface of  $\text{BaFe}_2(\text{As}_{1-x}\text{P}_x)_2$  on entering the superconducting dome. *Phys. Rev. Lett.*, 104:057008, Feb 2010.
- [103] C. G. Wang, Z. Li, J. Yang, L. Y. Xing, G. Y. Dai, X. C. Wang, C. Q. Jin, R. Zhou, and Guo-qing Zheng. Electron mass enhancement near a nematic quantum critical point in  $\text{NaFe}_{1-x}\text{Co}_x\text{As}$ . *Phys. Rev. Lett.*, 121:167004, Oct 2018.
- [104] J. C. Palmstrom, P. Walmsley, J. A. W. Straquadine, M. E. Sorensen, D. H. Burns, and I. R. Fisher, Comparison of temperature and doping dependence of nematic susceptibility near a putative nematic quantum critical point, arXiv:1912.07574.
- [105] In a tetragonal system, positive and negative  $B_{1g}$  has the same effect to the material, therefore,  $T_s$  can only be an even function of  $B_{1g}$  strain - quadratic to leading order.
- [106] In cases where a scaling hypothesis holds, the critical temperature is set by an energy scale that is inversely proportional to the critical correlation time  $\tau_C \sim (g_C - g)^{-\nu z}$  where  $\nu$  is critical exponent for the correlation length, and  $z$  is dynamical scaling exponent. In such case,  $\theta = \nu z$  [49], but we persist in writing the exponent simply as  $\theta$  to preserve generality.
- [107] Positive and negative  $B_{1g}$  strain suppress the critical temperature equally, hence the square on  $\epsilon_{B_{1g}}$ .
- [108] Chiaki Fujii, Shalamujiang Simayi, Kouhei Sakano, Chizuru Sasaki, Mitsuteru Nakamura, Yoshiki Nakanishi, Kunihiro Kihou, Masamichi Nakajima, Chul-Ho Lee, Akira Iyo, Hiroshi Eisaki, Shin-ichi Uchida, and Masahito Yoshizawa. Anisotropic Grneisen parameter and diverse order parameter fluctuations in iron-based superconductor  $\text{Ba}(\text{Fe}_{1-x}\text{Co}_x)_2\text{As}_2$ . *Journal of the Physical Society of Japan*, 87(7):074710, 2018.
- [109] Mario Zacharias, Indranil Paul, and Markus Garst. Quantum critical elasticity. *Phys. Rev. Lett.*, 115:025703, Jul 2015.

- [110] Daniel S. Fisher. Random transverse field ising spin chains. *Phys. Rev. Lett.*, 69:534–537, Jul 1992.
- [111] Olexei Motrunich, Siun-Chuon Mau, David A. Huse, and Daniel S. Fisher. Infinite-randomness quantum ising critical fixed points. *Phys. Rev. B*, 61:1160–1172, Jan 2000.
- [112] Herbert B. Callen. The application of onsager’s reciprocal relations to thermoelectric, thermomagnetic, and galvanomagnetic effects. *Phys. Rev.*, 73:1349–1358, Jun 1948.
- [113] J. A. W. Straquadine, J. C. Palmstrom, P. Walmsley, A. T. Hristov, F. Weickert, F. F. Balakirev, M. Jaime, R. McDonald, and I. R. Fisher. Growth of nematic susceptibility in the field-induced normal state of an iron-based superconductor revealed by elastoresistivity measurements in a 65 t pulsed magnet. *Phys. Rev. B*, 100:125147, Sep 2019.
- [114] N. Ni, A. Thaler, J. Q. Yan, A. Kracher, E. Colombier, S. L. Bud’ko, P. C. Canfield, and S. T. Hannahs. Temperature versus doping phase diagrams for  $\text{Ba}(\text{Fe}_{1-x}\text{TM}_x)_2\text{as}_2$  (TM = Ni, Cu, Cu/Co) single crystals. *Phys. Rev. B*, 82:024519, Jul 2010.
- [115] M. D. Watson, T. K. Kim, A. A. Haghighirad, S. F. Blake, N. R. Davies, M. Hoesch, T. Wolf, and A. I. Coldea. Suppression of orbital ordering by chemical pressure in  $\text{fese}_{1-x}\text{sx}$ . *Phys. Rev. B*, 92:121108, Sep 2015.